Spin-dependent transport and X-ray imaging of microwave-frequency magnetic vortex oscillations in nanoscale spin valves

by Vlad-Stefan Pribiag

This thesis/dissertation document has been electronically approved by the following individuals:

Buhrman,Robert A (Chairperson)

Brouwer,Piet (Minor Member)

Ralph,Daniel C (Minor Member)

SPIN-DEPENDENT TRANSPORT AND X-RAY IMAGING OF MICROWAVE-FREQUENCY MAGNETIC VORTEX OSCILLATIONS IN NANOSCALE SPIN VALVES

A Dissertation

Presented to the Faculty of the Graduate School

of Cornell University

in Partial Fulfillment of the Requirements for the Degree of

Doctor of Philosophy

by

Vlad-Stefan Pribiag

August 2010

SPIN-DEPENDENT TRANSPORT AND X-RAY IMAGING OF
MICROWAVE-FREQUENCY MAGNETIC VORTEX OSCILLATIONS IN
NANOSCALE SPIN VALVES

Vlad-Stefan Pribiag, Ph.D.

Cornell University 2010

This dissertation is a summary of my investigations of the effects of spin-polarized currents on the dynamics of nanomagnets in which the magnetization has a vortex configuration. The "active" region of the devices consists of two ferromagnetic layers (typically made of $Ni_{81}Fe_{19}$) separated by a nonmagnetic "spacer" made of Cu. The devices are lithographically patterned into nanoscale pillar structures. To obtain a stable magnetic vortex one of the two ferromagnetic layers is considerably thicker (typically 60 nm) than the exchange length of $Ni_{81}Fe_{19}$ ($\sim$ 5 nm), making the vortex configuration more energetically favorable than the single-domain.

Transfer of angular momentum from a spin-polarized current to a ferromagnet provides an efficient means to control the dynamics of nanomagnets, and consequently has been one of the most active areas of research in the field of magnetism over the past decade, driven in part by the potential for applications such as non-volatile magnetic memories and tunable, dc-driven gigahertz-frequency oscillators.

Prior to my work, spin-torque driven oscillations of the magnetization had been investigated primarily in devices containing spatially uniform nanomagnets. In contrast, my experiments demonstrate that a dc spin-polarized current can be used to drive steady-state oscillations of a magnetic vortex in a spin-

valve nanopillar. Detection of these oscillations is accomplished by measuring the time-varying voltage generated via the giant magneto-resistance effect. I investigated the decoherence mechanisms in these oscillators through a combination of frequency-domain and single-shot time-domain measurements. I found that, surprisingly, vortex oscillations can exhibit considerably narrower linewidths than uniform oscillations, which means that they can be a more coherent source of microwaves than vortex-free spin-torque oscillators. Yet the vortex oscillation modes also exhibit a substructure characterized by slow, discrete fluctuations that provides important insight into the possible sources of decoherence.

In addition to electronic transport measurements I have also used circularly-polarized x-rays to obtain the first time-resolved, real-space images of a spin-torque oscillator. These images show that the vortex has an unexpectedly complex magnetization profile resulting from the characteristically small size of these devices, and suggest that this complexity plays an important role for the excitation of steady-state vortex oscillations.

BIOGRAPHICAL SKETCH

Vlad Stefan Pribiag was born on February 17, 1980 in Bucharest, Romania, the son of Nicoleta and Gheorghe Pribiag. Three years later the stork brought a little brother, Horia, who has been his closest companion ever since.

If a mother's memories of her children's early years are anything to go by, it would appear that Vlad's interest in the nature of things predates his own oldest memories, his mother mentioning that at the age of three he was already inquiring about such things as the physics of the boiling of water, as well as performing his own experiments on the terminal velocities of various vegetables by launching them from the windows of his third floor laboratory. Dating from somewhat later, impressions of free-standing memories start to emerge: an experiment on the thermally-induced deformation of a plastic cup in an oven (with surprising results!), an early fountain pen, and later, already in kindergarten, a team project to build what would undoubtedly have led to the first time machine, had he and his collaborators not been so quickly asked to enter the regimented life of elementary school, with its rhythm so inescapably punctuated by the ringing of the electric buzzer commonly referred to as the "bell." Fortunately, the "bell" did not give him the headaches he had feared, and thanks to his mother's sustained (and often heroic) support and his teacher's stick and stick method, he ended up developing an appreciation for the more formal paths to knowledge, and was even a regular winner of academic prizes.

In December 1989, when school was off, Vlad remembers being on the balcony, watching tanks make their way towards the center of Bucharest, followed for days by the sounds of machine gun fire in the distance. There was also beautiful white snow, and school was off indefinitely, which would have been enough to put any 10 year old in a happy trance, even in the absence of that

permeating feeling that his life was about to change dramatically. Weeks later his father took him to see the center of the city, with the burnt skeleton of the National Library lying next to the bullet-ridden National Art museum and the former headquarters of the heretofore all-powerful communist party with its notorious balcony where the change had started.

A few months later, he left Romania for the first time and moved with his family to Switzerland. There, he learned that not being able to speak the local language can lead to certain difficulties related to social interaction, especially when one is 10 years old and a foot taller than everyone else. There, he also learned to speak French. From his teacher he learned that school can be fun and that altruism is not just a myth.

Two years later, Vlad returned to his native land, looking for, but unable to find his homeland. After catching up with two years of Romanian-style education in one trimester, eventually demonstrating that he was not only able to solve systems of linear equations etc as required, but also to perform jumps across distances whose length matched or exceeded the requirements imposed by the Ministry of Education, he was finally allowed to enroll in the 7th grade. Over the next 2 years he managed to recover most of his remaining curricular deficiencies and after 8th grade was admitted to the mathematics-physics section of the prestigious Spiru Haret high-school in Bucharest. After only one trimester in the high-school he emigrated with his family to Canada (a move which incidentally saved him from nearly failing his formal logic class at the high school).

Canada adopted him and his family wholeheartedly, for which he is very grateful. Vlad attended the Earl Haig Secondary School in Toronto, where he enjoyed the company of a number of very original people, who were his intel-

lectual companions as well as his tennis and biking partners. After high school Vlad enrolled in the Computer Science and Physics Specialist program at the University of Toronto. He was initially torn between these two competing and largely non-overlapping concentrations, a struggle made no easier by the fact that his ultimate goal was and had been for quite some time to end up an astronomer, while at the same time he was discovering a growing interest for psychology. Ultimately, joining a condensed matter research group helped him realize that physics was the future! After working on spin injection into high T_c superconductors for about three years, Vlad was quite eager to start graduate studies in condensed matter experiment.

Despite the predominant lore on the boredom of life in Ithaca, Vlad was fortunate to meet someone who advised him quite to the contrary, leading to one of the best decisions he has made in his life. His experience at Cornell[1], which like many good things is drawing to an end, has been one of the happiest and most enriching in his life, both professionally and personally. This is thanks in no small part to the many wonderful people he has had the chance to meet here! In a few months, he will be embarking on a new journey, with his wife, Ioana. They are moving across the big pond, where Vlad will be starting a post-doc position in Leo Kouwenhoven's group at TU Delft, studying spin-related quantum transport phenomena in semiconductor nanowires. He hopes that in addition to doing lots of exciting physics, he is also going to be able to learn a new language.

---

[1]If a father's memories of his children's early years are anything to go by, Vlad's father, who was often engrossed in reading scarce copies of National Geographic, remembers reading about Cornell for the first time, in connection with the Arecibo observatory, on a park bench, near his son's stroller, at a time when the mere thought of traveling outside his country was only a dream.

A l'avenir,

together.

ACKNOWLEDGEMENTS

The work done for this dissertation could not have been completed without tremendous help from a large number of people. They provided me with the knowledge, inspiration, motivation and moral support to carry it through. I am greatly indebted to them for all this.

My advisor, Bob Buhrman is the first person whom I would like to thank. I have been tremendously fortunate and privileged to be able to work in his group. From him I have learned, first of all how to be a scientist; how to be enthusiastic about a problem, but also how to retain a skeptic's distance, how to try to peel off the layer of hype that so often enshrouds the scientific and practical relevance of research today. He has taught me that nothing in science exists in a vacuum and that one must always be aware of the context of a problem in order to avoid being blinded by its current glamor. He has also helped me become comfortable with a deceptively simple question: why is what you are doing important?

Bob has also been an extraordinary role model on how to run a research group efficiently, making sure that everyone has access to the necessary resources to do their work, that information flows within the group, that group members collaborate respectfully with each other, rather than competing, that meetings are never so short as to be irrelevant or so long as to become a burden. I can only hope that one day I will be able to apply, be it even a fraction of what I have learned from Bob in this respect. I would also like to thank him for the freedom he gave me to pursue all the research problems that interested me and for never pressuring me to work in a direction I did not feel attracted to. This and his constant support have meant a lot to me, and have helped me mature both as a scientist and as a person throughout these years. If I could go back

to my first year at Cornell in my kindergarten time machine and chose again, I can't imagine having worked in a better environment. Thank you, Bob!

I am also deeply grateful to Dan Ralph for his enormously helpful scientific advice and his insightful comments to my manuscripts. His sharp, challenging questions have made my work stronger and have been of tremendous importance in helping me grow as a scientist. I also learned a lot of condensed matter physics from him while working as a grader for his graduate-level course.

From Piet Brouwer's class I learned a large part of the advanced condensed matter I now know. I am also thankful to him for very helpful and always uplifting conversations about my work. Many thanks also to Chris Henley for his very insightful comments, and for graciously agreeing to be part of my special committee on such short notice.

I have been extremely fortunate to be able to work with Ilya Krivorotov when he was still a postdoc at Cornell. I am deeply indebted to him for his patient and illuminating advice at the time when I was still trying to come up with a project. From his encyclopedic knowledge of physics to his methodical approach to doing research and his great sense of humor, he has been, and continues to be, a constant source of inspiration for me.

I would also like to express my gratitude to John Wei at the University of Toronto, who gave me the opportunity to work in his group starting at the end of my freshman year, with nothing more than a course in general physics under my belt, and in whose lab I experienced my first revelations about condensed matter physics.

Nathan Emley and Greg Fuchs in the Buhrman group were my mentors in my early years. I owe many of my research skills to them, from nano-fabrication to measurements and analysis. Jack Sankey has been great every time I had

any questions about microwave measurements. I would also like to thank John Read for pointing me in the direction of Bob's group in my first year, when we were both taking Neil Ashcroft's class, as well as the great Ozhan Ozatay and Pat Braganca for many discussions about science and more over the years. Giovanni Finocchio's micromagnetic simulations have enabled me to understand many of the complex features of the vortex oscillations. He is also a great friend and a great dancer (to whom I must apologize for one night at Pixel when the D.J. was the only one enjoying the music). Zhipan Li and I shared many long days (and nights[2]) fabricating suspended nanopillars at the CNF and traveling to California for our x-ray imaging experiments. I would also like to thank Yves Acremann (then at SSRL) and Xiaowei Yu at Stanford for many discussions during our collaboration.

A certain Praveen Gowtham has been an awesome friend with whom I enjoy talking as much about physics, as about current affairs or ancient Greece. A true Upper East sider (or is it West? I can never remember), he has also been kind enough to share with me childhood stories of an infamous rat-bashing neighborhood superhero, as well as his impressive knowledge of YouTube star artists, sometimes (but not always) against my immediate will. I would also like to thank Oukjae Lee, with whom I have had many fruitful discussions about linewidth broadening and more, and whose bulgogi seems to be very delicious. Big thanks go to Junbo Park for helping out during many long hours in the CNF cleanroom and in the basement of Clark. With my graduation he is about to find new freedom and to start his own project.

I am also very grateful for many discussions and experiences (at various times of the day) to Attila Bergou, Jean-François Brière, Yongtao Cui, Nate

---

[2]The nights at the CNF would have been much duller without the unfading presence of Rob Ilic, whom I would also like to thank, among many things, for the tips about KOH etching he gave me during one of his 2 AM breakfasts.

Gabor, Saikat Ghosh, Simon Gravel, Ted Gudmundsen, Pinshane Huang, Jörn Kupferschmidt, Yun Li, Johannes Lischner, Luqiao Liu, Alex Melnik, Takahiro Moriyama, Tchefor Ndukum, Josh Parks, Sumiran Pujari, Sophie Rittner, Eric Ryan, Sufei Shi, Eugenia Tam, Kiran Thadani, Hsin-wei Tseng, Chen Wang, Ben Williams, Lin Xue, Arend van der Zande and many, many others.

Special thanks go to all the great guys in the machine shop, and in particular Bob Snedeker ("Sned") (who has taught me most of what I know about the art of machining, and who has ensured over the years that I can "count to ten and see to do it"), Rodney Bowman, Stan Carpenter and Nate Ellis. I would also like to thank Jon Shu for being a fantastic lab manager for the Cornell Center for Nanoscale Systems.

Cornell is a big place and Ithaca is a whole city. Over the years, Ioana and I have also been very lucky to share the company of many great friends outside of the physics department. We are both very grateful for all the wonderful moments, and hope they will extend well into the future.

I saved my family for last, because I was hoping that, given more time, I could find more adequate words to express the role they played in helping me reach the point where I am now, writing this dissertation. Well, that time is now up and I am no better off. Words just won't serve! But what I can say with certainty is that without their support the work that went into this dissertation would have felt incomplete; that a great part of what it is about is due to them, to what they taught me is worth doing, and to the dreams they seeded and nurtured in me. They are the ones who, through example and advice, have inspired me and have given me the confidence that I could achieve what I had set out to do. They are my mother, my father and my brother, who have always been there for me. They are also my grandparents, who are no longer here.

They are also my wife's parents, grandparents and her sister, who have not only raised this wonderful creature, but who have also welcomed me among them with such a rare warmth.

Finally, I would like to thank Ioana, who, with her constant encouragements, has helped me stay sane throughout the more stressful times, and who, with her impressively contagious energy, curiosity and determination, has helped me grow in ways I could not have imagined.

Thank you!

TABLE OF CONTENTS

LIST OF TABLES

LIST OF FIGURES

CHAPTER 1

MAGNETOELECTRONICS AND SPINTRONICS

1.1 Introduction

Electrons have an electrical charge and a quantum mechanical spin. Many of the innovations in data processing and information storage in the 20th century have relied on controlling the mobility of electrons (or holes) by means of electric fields. However, the magnetic properties of materials have played an important role for a long time, starting from the magnetic core memories that were precursors to modern electronic Random Access Memory (RAM), to the magnetic hard disk technology which dominates long-term data storage today. Magnetic devices are more accurately called magnetoelectronic because in general electrical transport measurements need to be performed in order to manipulate the state of or read from the device. In the case of early magnetolectronics, such as core memories or early hard disks, the relevant degree of freedom was the macroscopic magnetization, which was accessed classically, by means of elecromagnetic induction. The more recent field of spintronics proposes to exploit, to various degrees, the quantum mechanical properties of the electron spin, which are intrinsically microscopic. The goal is generally either to modulate the electron mobility through the spin degree of freedom (in metallic or semiconducting devices) or to achieve coupling between the electron spin and photons (semiconducting devices) [1]. Among the properties that make make spin such an attractive degree of freedom, two appear to stand out: i) the existence of an energy splitting between spin up and spin-down electrons in ferromagnets, which allows efficient coupling to the charge degree of freedom (as discussed in more

detail below), and ii) the fact that electron spin is a natural quantum mechanical two-level system, which make it promising for quantum computation [2, 3]. Of course, any information processing device will need to fulfill two basic function: accept an input and produce a readable output. The sections below will outline the relevant physics, with emphasis primarily on metallic spintronic devices, which are the main subject of this dissertation. The following section will deal with the physics of information readout in such devices, specifically with magnetoresistance, which has led to the first technological breakthroughs in spintronics. The section that follows it will deal with the physics of the information input and data manipulation, specifically spin-transfer torques.

1.2   Magnetoresistance

Magnetoresistive (or galvanomagnetic) effects consist of a change in the electrical resistance of a material or device in response to an applied magnetic field or a reorientation of the magnetization (the later need not occur as result of an applied magnetic field, as we will see in the section on spin-transfer torques). Below is a list of several types of magnetoresistive processes [4, 5, 6, 7]:

1. The so-called Ordinary Magnetoresistance (OMR), which can arise in ferromagnetic or non-ferromagnetic materials, leads to an increase in resistance with applied magnetic field and is due to the Lorentz force acting on the electron trajectories (the latter also being responsible for the ordinary Hall resistance). This is usually a small effect ($< \sim$ 1% at fields on the order of 1 Tesla).

2. In ferromagnetic materials, in addition to OMR, there exists an additional effect, called Anisotropic Magnetoresistance (AMR), which depends on the rel-

ative orientation of the magnetization and the electric current. The size of the effect depends not only on the magnitude, but also on the direction of the applied field. Only a field that reorients the magnetization will result in an effect. In polycrystalline samples the minimum resistance is obtained when the magnetization is saturated perpendicular to the current direction and the maximum when the two are parallel (with a $cos^2(\theta)$ dependence on the angle θ between magnetization current). In single-crystal samples the AMR angular dependence is more complex because no averaging over randomly-oriented crystallites takes place (see e.g. Ref. [8]). AMR occurs because of the spin-orbit interaction (can be understood qualitatively as a change in the spin-dependent scattering cross-section of electrons due to the spatial reorientation of the orbitals, as a result of the applied field). AMR has been of great technological importance, replacing inductive read heads in hard drives in 1991, because of its comparatively high sensitivity (~2% change in resistance for 10 Oe of applied field for magnetically soft alloys, such as $Ni_{81}Fe_{19}$).

3. Giant Magnetoresistance (GMR), discovered in 1988 ([9, 10]), occurs as a result of the relative orientation of magnetic moments within a layered or granular metallic magnetic structure. This effect has been of great technological importance because it can result in considerably larger changes in resistance than any of the previous mechanisms (in excess of 80% relative to the minimum value). As a result, GMR read heads replaced AMR read heads in hard disks starting around 1997. However, the relevance of the GMR effect extends well beyond hard disk technology. Its discovery and understanding is often considered as a major milestone in the development of the greater field of spintronics, which was in part recognized by the 2007 Nobel Prize for physics. Since GMR is the primary detection mechanism for the devices I studied, I will dedicate the

next section to a more detailed description of this phenomenon.

4. Magnetoresistance due to the reorientation of the local magnetization is not unique to all-metallic systems. Systems where adjacent magnetic layers are separated by an insulator that is sufficiently thin to allow quantum-mechanical tunneling of electrons can exhibit the so-called Tunneling Magnetoresistance (TMR). This phenomenon was discovered in 1975 [11], before GMR, but it did not receive much attention until higher quality barriers were developed in 1995 [12, 13]. TMR is currently of great importance for the development of spin-based electronics, due in part to the fact it offers resistance changes that can be in excess of 500% [14] relative to the minimum value.

5. Another large magnetoresistance effect is the so-called Colossal Magnetoresistance (CMR), which occurs for certain Mn-doping concentrations in perovskite compounds, such as those based on $LaMnO_3$. The magnetoresistance in these compounds can be several orders of magnitudes, and occurs as the materials undergo a phase transition upon cooling. The materials are paramagnetic insulators above a certain temperature and become ferromagnetic metals at low temperature [15]. A large change in resistance is observed when the materials are cooled in a magnetic field vs. zero field. So far, this effect has been relatively unpromising for spintronics applications because of the requirement of low temperatures and large (several Tesla) applied magnetic fields.

1.2.1 Giant Magnetoresistance

As mentioned briefly above, the GMR effect occurs in magnetic multilayers or granular materials and requires a local reorientation of the magnetization.

Therefore, it is not intrinsic to a given material, but is instead a characteristic of an appropriately engineered structure. Thus, the 1988 discovery of GMR [9, 10] was largely facilitated by the discovery, two years earlier, of interlayer exchange coupling [16, 17, 18], which favors the parallel or antiparallel orientation of thin magnetic layers separated by a normal (non-ferromagnetic) metallic layer. The strength and sign of this coupling was later found to oscillate as a function of thickness of the normal layer [19]. Interlayer exchange coupling thus resulted in a system where adjacent magnetic layers could be naturally oriented antiferromagnetically (antiparallel to each other) in the absence of an applied magnetic field, but could have a ferromagnetic (parallel) orientation at sufficiently large fields, thus enabling a change in resistance to be observed. The resistance has a minimum value when the layers are parallel and a maximum value when they are antiparallel (see Fig. 1.1), with an approximately cosine angular dependence given by equation 1.1 [21]:

$$R(\theta) = R_P + (R_{AP} - R_P)(1 - cos(\theta)) \qquad (1.1)$$

where R is the resistance, θ is the angle between the adjacent layers, R_P is the resistance of the parallel configuration and R_{AP} that of the antiparallel configuration. Some studies have found evidence that the conductance, rather than the resistance has a cosine angular dependence, but the difference between the two models is second order in the GMR ratio, so it is in general negligibly small [22]. GMR can be observed in two types of multilayered structures (the case of granular structures is not directly relevant for this dissertation or for most current applications of GMR): devices where the current flows in-plane (CIP) and devices where the current flows perpendicular to the plane (CPP) (see Fig. 1.2). Although the initial discovery of GMR was made on CIP devices, and most of the initial theoretical models were aimed at this geometry, CPP devices can ex-
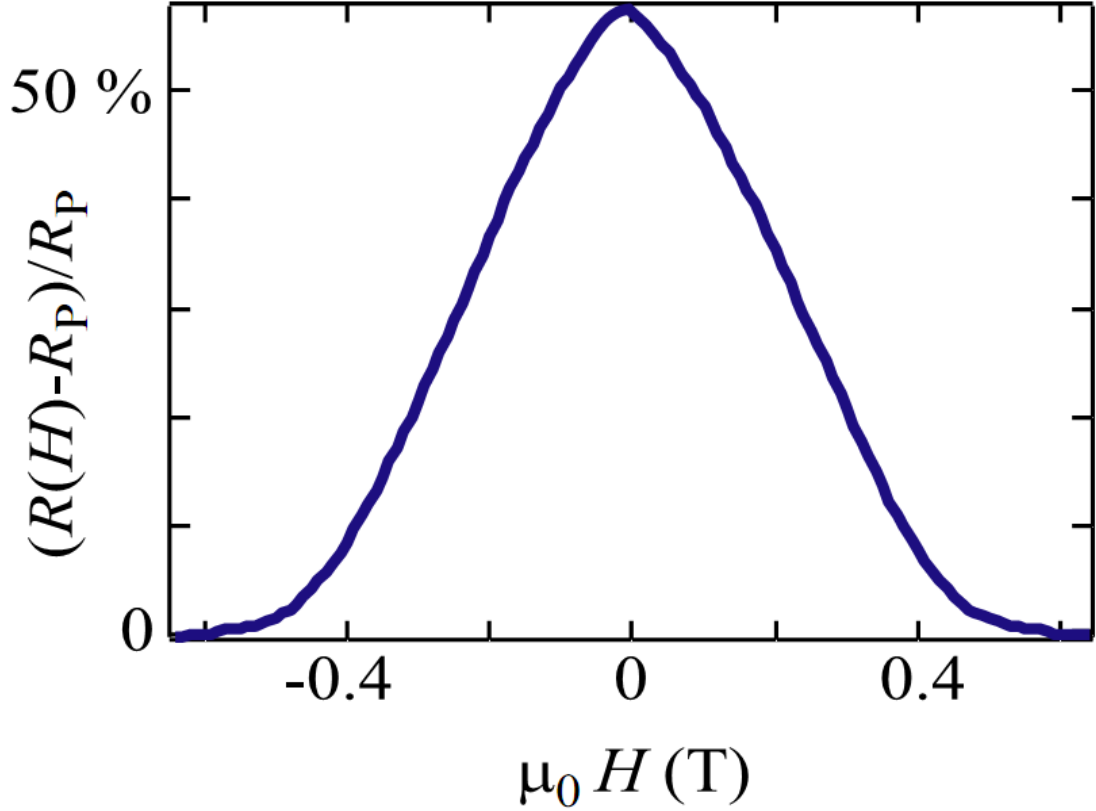
Figure 1.1: Giant Magnetoresistance (GMR) vs. applied field H for a [Co(1.2 nm)\Cu(0.96 nm)]$_{10}$ multilayer structure measured for current flowing in plane, at a temperature of 4.2 Kelvin. (From [20])

hibit larger GMR values, and can also show a significant magnetoresistance up to greater layer thicknesses [23] (but require considerably more advanced fabrication techniques, since only when the lateral dimensions are at the nanoscale are the resistance and GMR large). For reasons that will be explained in the section on spin-transfer torques, the CPP geometry has additional advantages over CIP, and is therefore the geometry of all devices studied for this dissertation. Below, I will describe briefly some of the models used to understand GMR, with particular attention to the CPP case.
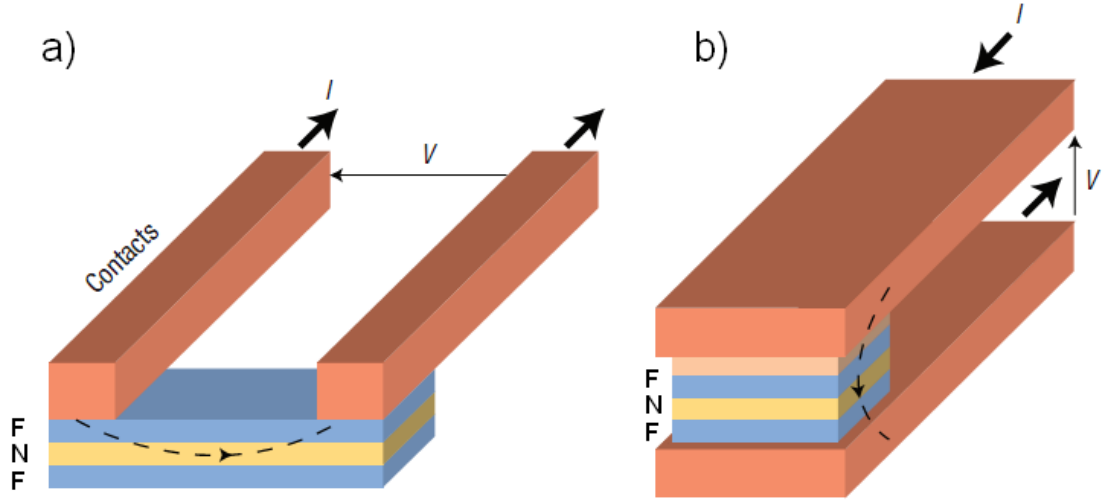
Figure 1.2: Comparison of two GMR geometries: a) CIP geometry, b) CPP geometry. *I* is the applied current and *V* the resulting voltage. The ferromagnetic layers are labeled F and the normal layers N. For the CIP case, a trilayer is shown, but typical structures are designed with multiple F\N iterations in order to obtain larger GMR values. For the CPP case, large GMR values can be obtained with a simple trilayer, as shown in b). (Adapted from [7])

Two current model

A qualitative understanding of GMR can be obtained by starting from the Mott model [24]. The main two assumptions[1] of the model are i) that spin-up and spin-down electrons (as defined by a quantization axis) act as independent conduction channels, and ii) that conduction occurs mostly through valence *sp* bands, while the *d* bands influence the conductivity indirectly, by providing states for the *sp* electrons to scatter into. Since the *d* band is exchange split in 3*d* transition metal ferromagnets, the spin-up and spin-down subbands have

---

[1]In general a finite CIP GMR effect is only observed if the mean free path for momentum scattering is greater than the layer thicknesses. Very thin layers compared to the mean free paths are required for a large effect. The mean free path is not relevant for observing CPP GMR.
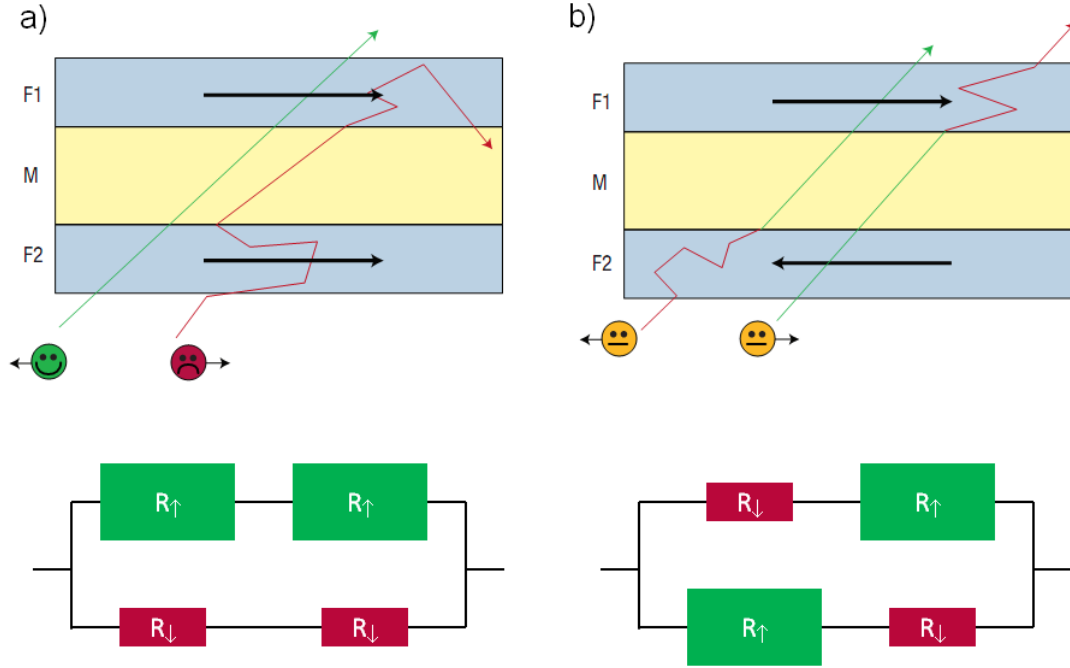
Figure 1.3: Simplistic illustration of the GMR effect in a CPP spin valve structure. Spin-up electrons (spin antiparallel to the local magnetic moment) experience a low rate of scattering, whereas spin-down electrons are scattered strongly. The two spin channels act as parallel conduction paths. a) When the two ferromagnetic layers are parallel the overall resistance is at its minimum value. b) When the ferromagntic layers are antiparallel the resistance is at its maximum value. (Adapted from [7])

different densities of states at the Fermi level, resulting in spin-dependent bulk scattering rates. From this it follows that *sp-d* scattering of majority (spin-up) electrons is weak because the low density of *d* states to scatter into, resulting in a low resistance for the majority channel. The opposite holds for the minority channel. If the two layers have parallel magnetizations then majority electrons in the first layer remain majority electrons in the second layer and the majority channel effectively short-circuits the device giving rise to a minimum resistance.

If, on the other hand, the two layers are antiparallel, then each spin channel is majority in one of the layers and minority in the other, resulting in a maximum resistance, as illustrated schematically in Fig. 1.3.

Band structure effects

Considering a realistic band structure has two main effects on the qualitative picture of GMR introduced above: i) refining somewhat the argument for spin-dependent bulk scattering, and ii) introducing an additional, interfacial contribution to the GMR. In $3d$ metals the $4s$ and $4p$ electrons hybridize to form a sp band that is characterized by high velocity and low density of states, making these free-like electrons primarily responsible for the electric conductivity. The $3d$ electrons are characterized by a low velocity and high density of states, as well as a narrow energy range. If the sp and d bands overlap, they also hybridize, giving rise to $sp-d$ bands. These are characterized by a reduced energy range (band-bending), lower velocities and higher densities of states than the sp bands. As a result of this the exchange splitting of the d bands has major implications for the transport in transition metal ferromagnets. The majority electrons have a primarily sp character at the Fermi level, resulting therefore in a high conductivity, similar to a normal metal like Cu. For the minority electrons, however, the Fermi level falls across the $sp-d$ band, resulting therefore in substantially reduced conductivity of the minority channel. This is illustrated by the band diagrams in Fig. 1.4. As can be seen in Fig. 1.4, the band structure of Cu is much better aligned at the Fermi level with that of the majority Co electrons than that of the minority electrons. Since any energy step results in reflection, the difference in band matching introduces an interfacial

9
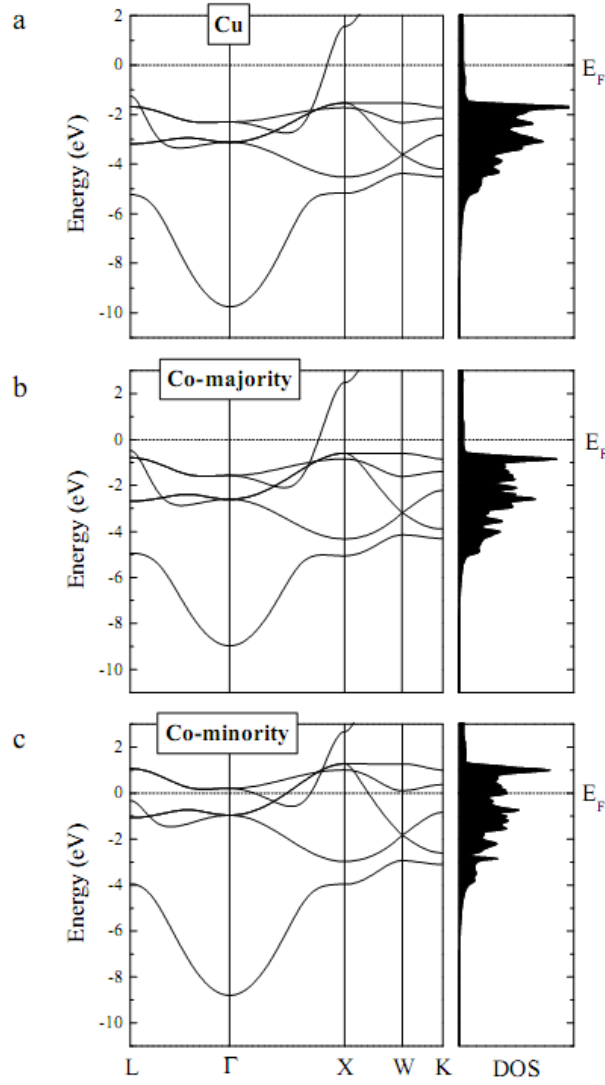
Figure 1.4: Electronic band structure and density of states for Cu and *fcc* Co.
a) For Cu, the majority and minority spin subbands are identical. The *d* bands
are filled and the Fermi level lies across the *sp* bands resulting in high conduc-
tivity. b) The exchange-split majority spin subband in Co is similar to Cu, and
has a high conductivity. c) The exchange-split minority spin subband in Co is
characterized has an $sp - d$ character at the Fermi level, resulting in a consid-
erably lower conductivity than the majority subband, as explained in the text.
(From [5])

spin-filtering effect at the Cu\Co interface: majority-spin electrons have relatively good matching and experience little reflection, while minority-spin electrons experience stronger reflection due to poorer band matching at the interface. Not all ferromagnet-normal metal combinations exhibit the same degree of band matching asymmetry. The two most typical combinations are Fe/Cr (in which GMR was discovered) and Co/Cu. Because of its very low magnetocrystalline and magnetoellastic anisotropies permalloy (Py: $Ni_{80}Fe_{20}$) is an excellent soft ferromagnetic material, often desirable over pure Fe or Cr. Fortunately, Py has an fcc structure that is similar to that of Cu, and very good band matching for the majority spin subband, resulting in high GMR values. [5]

Valet-Fert model and spin accumulation

Attempts at more rigorous descriptions of GMR have been put forward that model the electronic transport either semiclassically (based on the Boltzmann equation) or quantum mechanically. The treatment of the electronic structure is also very important and there is a whole spectrum of theories, ranging from free electron-models, to single-band tight binding, to more realistic multiband models [5]. In the case of CPP GMR, the most often employed model is one that was proposed by Valet and Fert in 1993 [25]. The model assumes free electrons and treats the transport using the Boltzmann equation. An important feature is that in addition to electronic momentum relaxation, it also includes a finite relaxation time for the spin, which effectively sets a length scale (referred to as the spin diffusion length) for the validity of the Mott two-current picture. The concept associated with the spin diffusion length is the so-called spin accumu-

lation[2], which refers to the creation of a chemical potential difference between spin-up and spin-down electrons near the ferromagnet/normal material interface. This chemical potential difference decays exponentially over the spin diffusion length, as given by equation 1.2

$$\Delta\mu(x) = \Delta\mu(0) * Exp(-x/l_{sf}) \tag{1.2}$$

where $\Delta\mu$ is the spin-induced chemical potential splitting, x (≥ 0) is the distance from the interface and l_{sf} is the spin-diffusion length. The name spin accumulation can be somewhat confusing at first, as it might suggest that the spin polarization always increases. In fact, spin accumulation results in a non-equilibrium spin population as a function of space. This does mean inducing a local spin polarization in the normal material, where the bulk equilibrium is spin-unpolarized, but for the ferromagnet it means a local spin depolarization near the interface, as illustrated in Fig. 1.5. One of the implications of the Valet-Fert model is that the relevant scale for CPP GMR is the spin-diffusion length and not the (usually much shorter) mean free path, as is the case for CIP GMR. This means that for CPP GMR the series resistor model applies regardless of whether the mean free path is shorter than or longer than the layer thickness, and also that an effect can be observed in both cases. The magnitude of the effect depends only on the layer thicknesses [28, 29]. This feature of CPP GMR allows structures to be made using slightly thicker layers than is possible for CIP devices, which can be useful in some cases, as for example the devices studied for this dissertation, where the normal metal (Cu) layers can be as thick as 40 nm, allowing control over the strength of the interlayer magnetostatic interaction. Another important implication of spin-accumulation and spin diffusion concerns

---

[2]The earliest experimental demonstration of spin accumulation, based on spin injection from a ferromagnet into a normal metal, was performed by Johnson and Silsbee at Cornell in 1985 [26], who also developed some of the early microscopic models of spin injection at a ferromagnet/normal metal interface (e.g. [27])
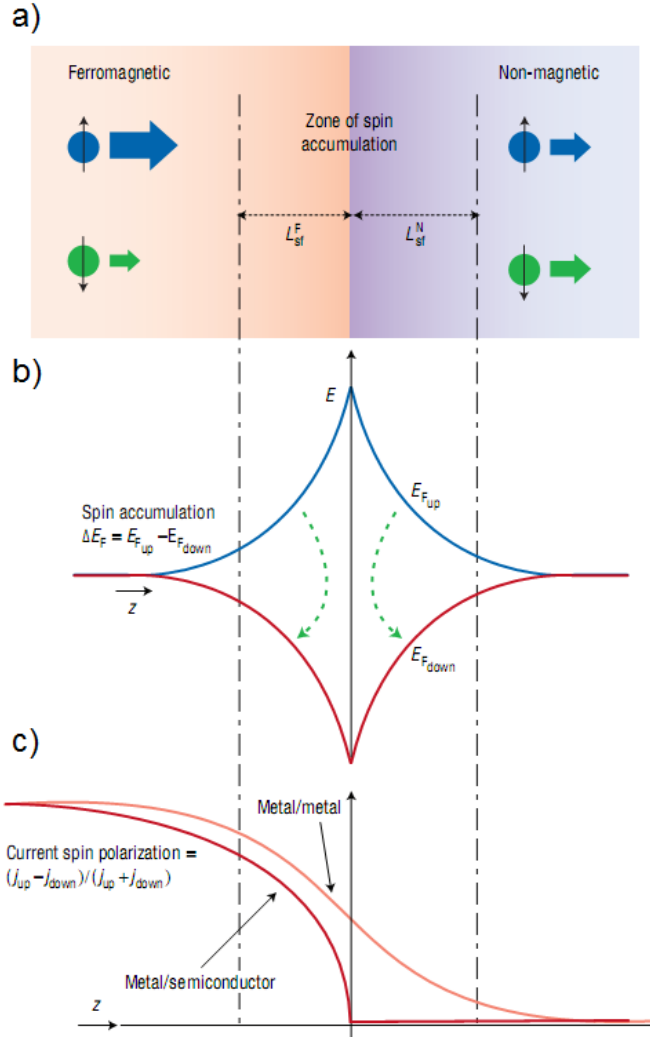
Figure 1.5: Spin accumulation and spin injection near a ferromagnet-normal material interface. a) Schematic of the sample geometry showing spin polarized electrons entering the normal material from the ferromagnet. b) Splitting of the chemical potential near the interface leads to spin accumulation. The dashed green arrows indicate spin flip between the two out-of-equilibrium spin populations. c) Schematic of the spatial profile of spin polarization showing the difference between the case of two metals (efficient spin injection) and the case of a metal-semiconductor junction (inefficient spin injection, as explained in the text). (From [7].)

the feasibility of hybrid spintronic devices that employ metallic ferromagnets to inject spin polarization into normal semiconductors. In this case the large conductivity mismatch and generally much shorter spin diffusion length in the metal than in the semiconductor leads to a quasi total depolarization of the spin current within the ferromagnet, making spin injection into semiconductors via ohmic contacts extremely inefficient [30]. (Introducing a spin-dependent interface resistance by means of a tunnel barrier or Schottky barrier is a solution to this issue [31, 32, 33, 34].)

1.2.2 Tunnel Magnetoresistance

Although none of the devices studied for this dissertation employ tunneling effects, I will nevertheless briefly describe the main aspects of spin-dependent quantum tunneling, with particular emphasis on Tunnel Magnetoresistance (TMR) (see Fig. 1.6) in ferromagnet/insulator/ferromagnet magnetic tunnel junctions (MTJ's). Spin-dependent tunneling is a natural complement to all-metallic spin-dependent transport and has great implications for the magnetic memory industry and other, more remote spintronic applications.

Jullière model

The simplest model used to understand spin-dependent tunneling and TMR was introduced by Jullière in 1975 when he made the first experimental obervations of the phenomenon on Co/oxidized Ge/Fe MTJ [11]. The model relies on the Mott two-current picture and the assumption that tunneling is spin-conserving. If the electrodes have parallel magnetizations then majority spin
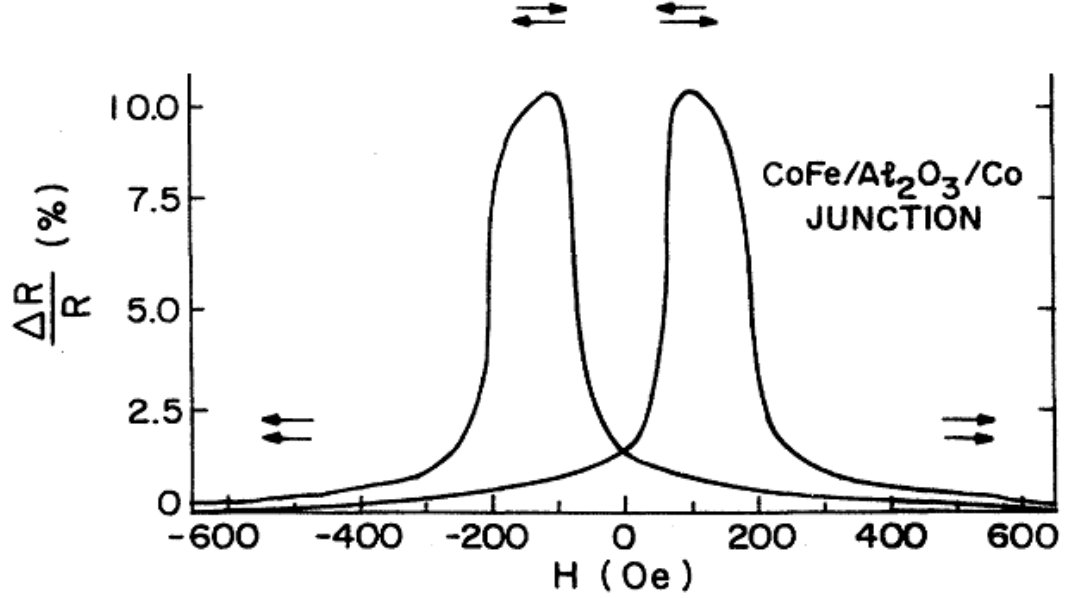
Figure 1.6: Magnetoresistance curve on a CoFe/Al$_2$O$_3$/Co MTJ, from one of the first two demonstrations of reproducible large TMR. (Modified from [12].)

electrons in the emitter are also majority spin in the collector and similarly for minority spin electrons. If, on the other hand, the electrode magnetizations are antiparallel, then each majority electrons become minority electrons after tunneling and vice versa. The fact that the density of states at the Fermi level is larger for minority spin electrons than for majority spin electrons has two implications: i) there are more minority electrons available to tunnel out from on the emitter side and ii) there are more minority states to tunnel into on the collector side, resulting in different conductivities for each of the two relative electrode orientations, as illustrated in Fig. 1.7 and described by equation 1.3.

$$TMR = \frac{P_1 P_2}{1 - P_1 P_2} \qquad (1.3)$$

where $P_i = \frac{D_{i\uparrow} - D_{i\downarrow}}{D_{i\uparrow} + D_{i\downarrow}}$, with $D_{i\uparrow}$ ($D_{i\downarrow}$) being the spin-up (spin-down) densities of states at the Fermi level for each of the two electrodes.

15

Insulator effects

The model of Jullière does not account for the role played by the tunnel barrier material itself in the tunneling process. Among the limitations of the model is the fact that it predicts a positive TMR (that is higher resistance in the antiparallel case), regardless of the details of the structure. Experimental observations have shown however, that the choice of insulator can change the sign of the TMR (e.g. [36]). Other than this dramatic qualitative effect, the insulator can also affect the magnitude of the TMR, resulting in values that exceed the predictions of the Jullière picture. This occurs when using a crystalline tunnel barrier material. The evanescent densities of states for each spin channel can be mod-
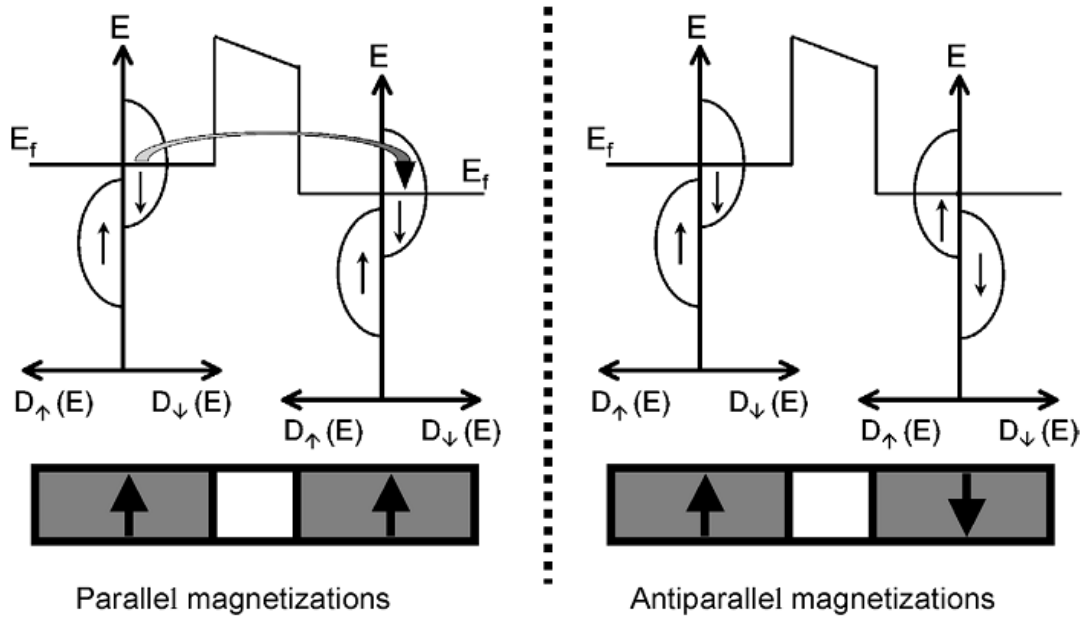
Figure 1.7: Schematic of the density of states for the two electrodes in a magnetic tunnel junction. In the Jullière model, the product of the densities of states in the two electrodes for each spin channel uniquely determines the magnetoresistance. (From [35].)
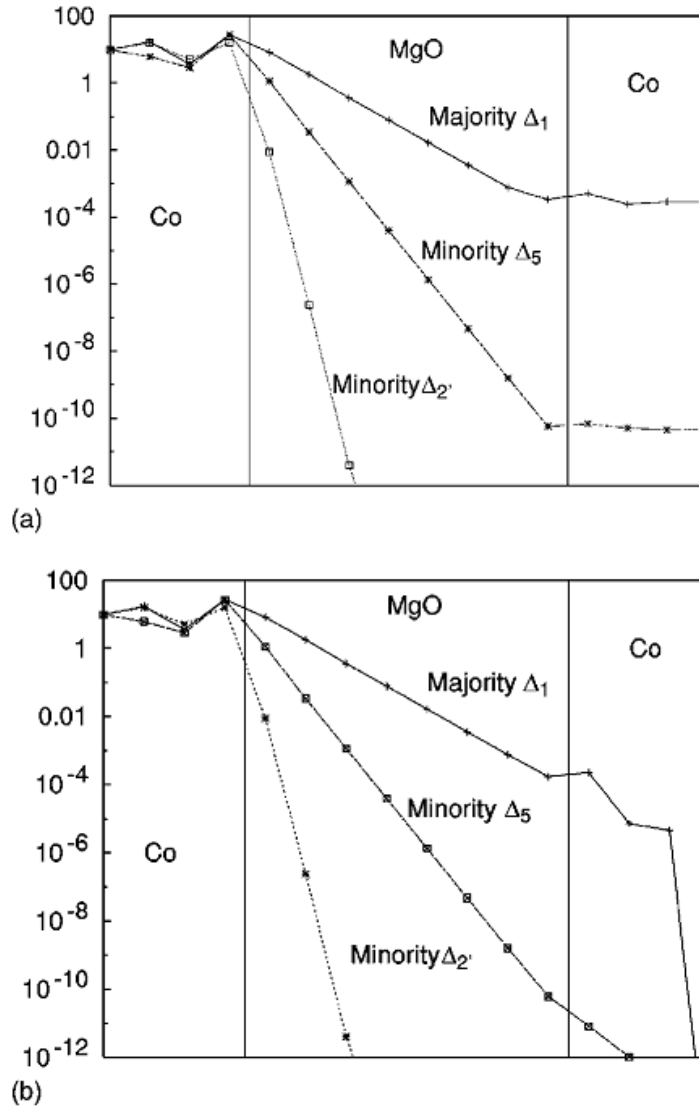
Figure 1.8: Tunneling density of states for Co/MgO/Co MTJ, illustrating the spin-filtering properties possible with a crystalline structure. a) Parallel alignment of the electrode magnetizations. b) Antiparallel alignment of the electrode magnetizations. (From [37].)

eled by using complex Bloch wavevectors ($k = q + i\kappa$). For example, the *bcc* Co(100)/MgO(100)/Co(100) system has a similar crystal structure for both the metal and the insulator, resulting in similar symmetries for the electronic bands across the entire structure [37]. As can be seen from Fig. 1.8 the Δ_1 channel experiences the slowest decay in the MgO barrier. The density of Δ_1 symmetry states in Co is high for majority spin electrons , but small for minority spin electrons. Consequently, the transmission rate is much larger in the parallel configuration than in the antiparallel case and the tunnel barrier effectively acts as a spin filter.

1.3 Spin-transfer torque

1.3.1 Context

As outlined in the previous section, the initial breakthroughs in the field of spintronics were related to the ability to read the state of a device, commonly the relative orientation of ferromagnetic layers in a spin valve or a magnetic tunnel junction, by means of GMR and TMR, respectively. However, writing of information is still in general accomplished by using magnetic fields. This has several disadvantages: i) magnetic fields are difficult to localize spatially (leading to writing errors in closely-packed arrays of devices), ii) switching with magnetic fields does not scale well (maintaining thermal stability of magnets as their size shrinks requires increasing the anisotropy, which in turns results in the need for larger switching fields, and consequently larger power consumption), iii) static magnetic fields cannot be used to produce oscillations (frequency sources, which are potentially useful for communications applications, can consequently

not be built).

An efficient alternative to manipulating small ferromagnets with field was proposed in two influential papers[3] in 1996 by Slonczewski [40] and Berger [41]. Their idea was that a spin-polarized current could be used to apply a torque to a ferromagnet. This would require much less current to produce a measurable re-orientation of the ferromagnet (at scales less than ~200nm) than a magnetic field generated by Ampère's law, and would also be highly localized. The dynamics excited by this spin-transfer torque (STT) could be classified in two broad types: i) switching of the magnetization of a spin-valve between two stable configurations (with great implications for the development of efficient, nonvolatile magnetic random access memory) and ii) steady-state oscillations of the magnetization under excitation by a direct current (with great implications for the development of on-chip, nanoscale, tunable oscillators in the GHz range) [42]. These are illustrated in Fig. 1.9. The first clear experimental observations of STT were made at Cornell (switching [43, 44], and steady-state dynamics [45]). The rest of this chapter will explore in more detail these two types of magnetization dynamics in all-metallic ferromagnet/normal/ferromagnet CPP trilayers and will conclude with a brief discussion of STT-driven domain wall motion and STT in the context of semiconducting materials.

---

[3]Early theoretical work on current-induced domain-wall drag had been done by Berger as early as 1974 [38]. Experimental work was also performed about 11 years later [39], but the phenomenon did not receive widespread attention until the formulations of STT by Slonczewski and Berger in 1996, perhaps in part because the fabrication capabilities for CPP structures did not mature until then.
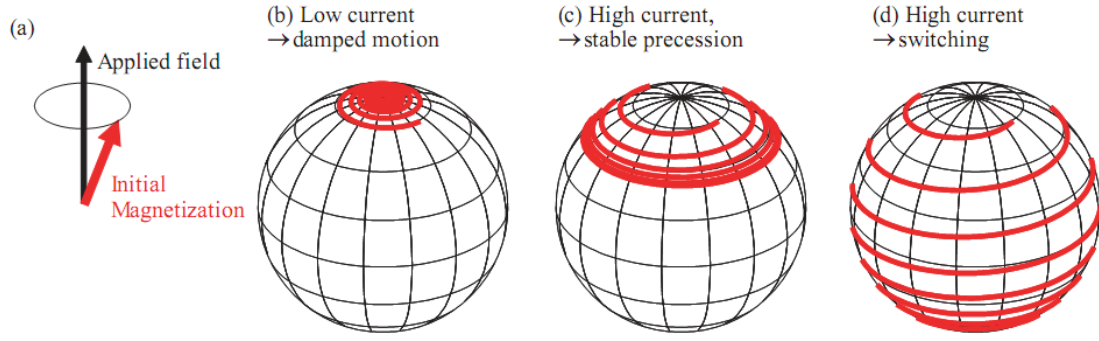
Figure 1.9: Illustration of the two types of dynamics that can be excited by STT for a magnetic moment with no anisotropy. a) Initial configuration of the magnetic moment in the presence of an applied field. b) For small (subthreshold) applied current amplitude the magnetization remains close to the stable equilibrium along the z-axis as a result of damping. For sufficiently large currents (above threshold), the STT leads to overall negative damping and the magnetization can undergo two types of dynamics, depending on the angular form of STT and damping: c) steady-state large-angle precession or d) reversal. (Modified from [20].)

1.3.2   Qualitative picture of STT in a metallic trilayer

An intuitive understanding of STT can be obtained by considering the flow of electrons in a current-biased spin valve, as illustrated by Fig. 1.10. The electrons entering the device are initially unpolarized since they are assumed to arrive from normal leads. They become spin-polarized by the first ferromagnet, so that the magnetic moment of the electrons transmitted through this layer is parallel to the magnetization of this layer. Some electrons are reflected, and these have the opposite magnetic moment. Upon incidence on the second ferromagnetic layer the transverse component of the spin is absorbed, giving rise to a torque,
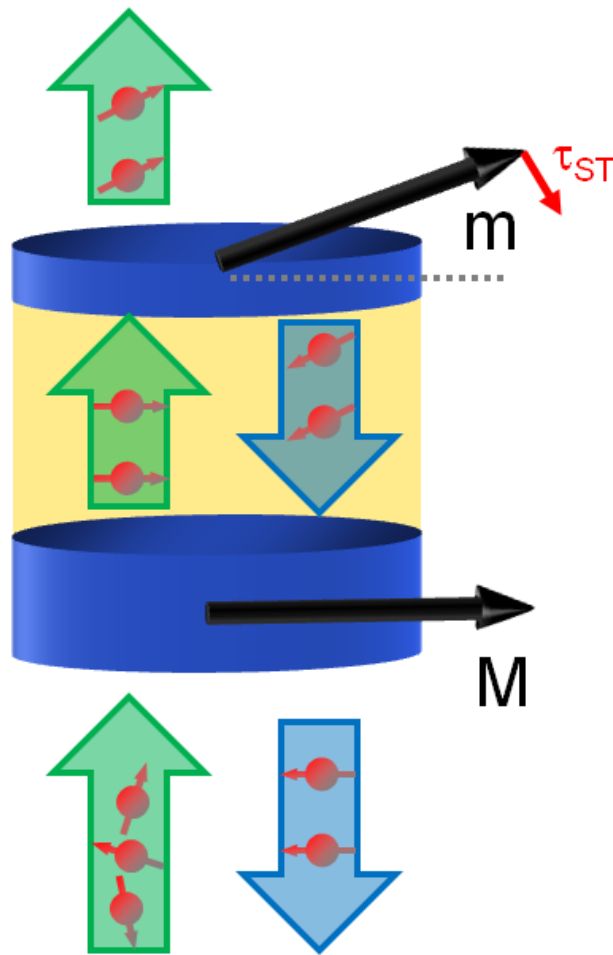
Figure 1.10: Cartoon illustrating spin-transfer torque in an all-metallic spin-valve. The device is current biased so that electrons flow upward. Initially unpolarized electrons become spin-polarized by the first ferromagnet (bottom blue layer) so that their magnetic moment is parallel to the magnetization of this layer. (Some electrons are reflected with the opposite magnetic moment.) Upon incidence on the second ferromagnetic layer (upper blue layer) the transverse component of the spin is absorbed, giving rise to a torque, referred to as spin-transfer torque. Here, too, some fraction of electrons are reflected. (These are spin-polarized such that their moment is opposite to the magnetic moment of the second ferromagnet.)

which is what is referred to as spin-transfer torque. Here, too, some fraction of electrons are reflected. These are spin-polarized such that their moment is opposite to the magnetic moment of the second ferromagnet. The reflected electrons will apply a torque on the first magnetic layer. Through common discourse it is easy to overlook the fact that this is not the end of the process. Of course, another transmission/reflection will happen at the first ferromagnet, then at the second ferromagnet, and so on. In general, accurate calculations of STT must take into account the iterative nature of the process (e.g. through a scattering matrix approach).

1.3.3   Microscopic physics of spin-transfer torque

A more detailed understanding of the physics of STT can be obtained by looking at the quantum mechanical processes from which it originates. A simple 1-dimensional model, as shown in Fig. 1.11, can be quite useful to illustrate the torque exerted by one electron incident on a ferromagnet [20]. We consider an incident spinor plane-wave wavefunction for a single electron with spin at angle θ to the z-axis:

$$|\psi_{incident}\rangle = Ce^{ikx}(cos(\theta/2)|\uparrow\rangle + sin(\theta/2)|\downarrow\rangle) \tag{1.4}$$

where C is a normalization factor. Because of the ferromagnet's exchange splitting the energy of the spin-up electrons in the ferromagnet is lower by Δ than that of spin-down electrons. We can set the potential step at the normal/ferromagnet interface to be 0 for spin-up electrons, so that only spin-down electrons are reflected (by a potential step of height Δ). This is a good approximation for many commonly-used normal/ferromagnet interfaces, such as Cr/Fe, Cu/Co or Cu/Ni. Then the transmitted and reflected wavefunctions can
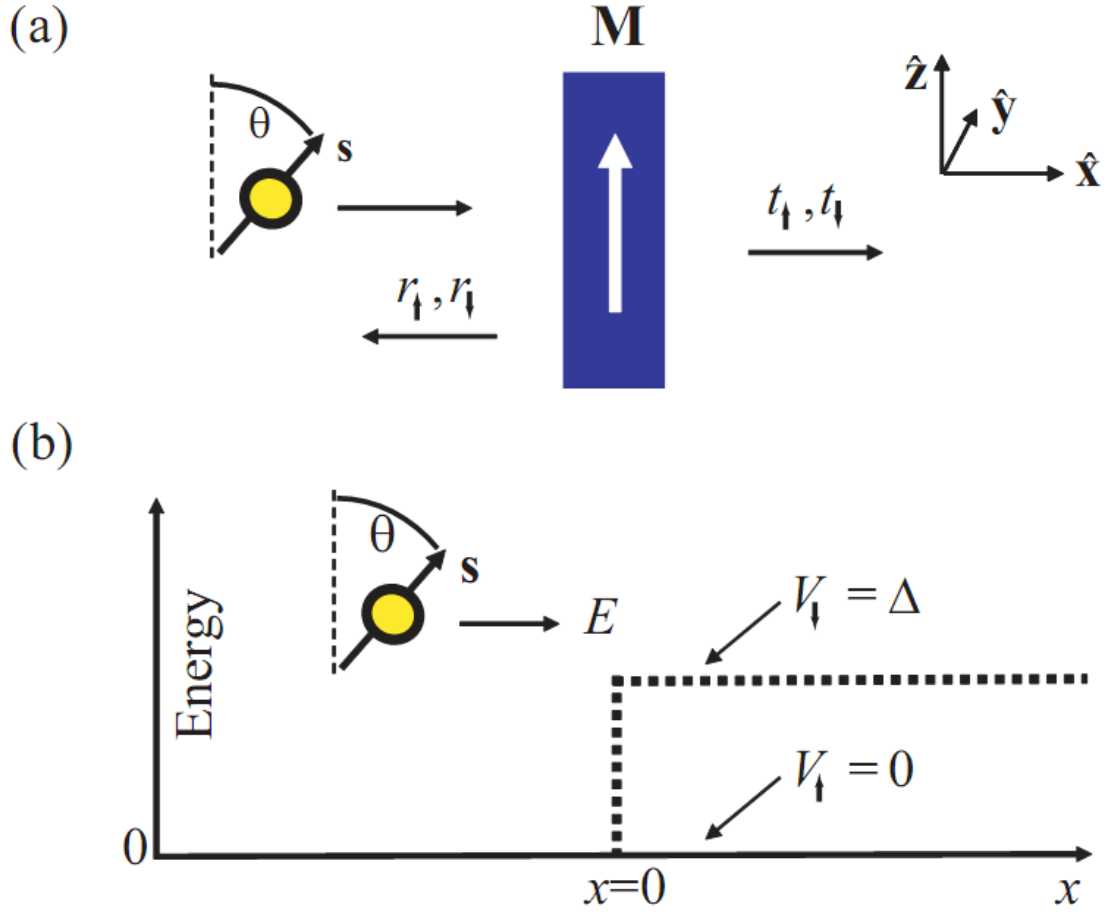
Figure 1.11: 1-D model for spin-torque showing a) scattering of electrons by a ferromagnetic layer, and b) a simplified mechanism for the scattering, based on the exchange-splitting Δ between the two spin subbands. $r_\uparrow$ ($r_\downarrow$) and $t_\uparrow$ ($t_\downarrow$) are the spin-up (spin-down) reflection and transmission amplitudes, respectively. (Modified from [20].)

be calculated to be

$$|\psi_{transmitted}\rangle = C(e^{ik_\uparrow x}cos(\theta/2)|\uparrow\rangle + e^{ik_\downarrow x}\frac{2k}{k+k_\downarrow}sin(\theta/2)|\downarrow\rangle) \qquad (1.5)$$

$$|\psi_{reflected}\rangle = Ce^{-ikx}\frac{k+k_\downarrow}{k+k_\downarrow}sin(\theta/2)|\downarrow\rangle \qquad (1.6)$$

23

where $k_\uparrow = k$ (since spin-up sees no potential step in this simplified model) and $k_\downarrow = \sqrt{2m(E-\Delta)}/\hbar$, with E being the energy of the incident electron ($E > \Delta$) and m the free electron mass. The spin-transfer torque per electron is given by equation 1.7, which expresses the conservation of angular momentum

$$\mathbf{N} = -\int \hat{\mathbf{n}} \cdot \mathbf{Q}\, d^2\mathbf{R} \tag{1.7}$$

where $\mathbf{Q}$ is the spin current density per unit area of the ferromagnet, $\hat{\mathbf{n}}$ is the unit vector normal to the ferromagnet surface and the integral is over the surfaces of the ferromagnet. Thus, in order to calculate the amount of spin angular momentum transferred from the conduction electrons to the ferromagnet (and hence the spin-transfer torque) it is first necessary to compute the spin current densities per unit area of ferromagnet $\mathbf{Q}$ (incident, transmitted and reflected parts). At the normal/ferromagnet interface these can be computed from equation 1.8 by using the corresponding wavefunction given by equations 1.4, 1.5 and 1.6:

$$\mathbf{Q} = \frac{\hbar^2}{2m}\mathrm{Im}(\psi^*\boldsymbol{\sigma}\otimes\boldsymbol{\nabla}\psi) \tag{1.8}$$

where $\boldsymbol{\sigma}$ is the vector of Pauli matrices. By performing this calculation it is found that the transverse (in the x-y plane) component of the spin current density is entirely transmitted through the normal/ferromagnet interface, while the reflected spin current has moment pointing along -z (antiparallel to the magnetization). Moreover, the transverse components of the spin current transmitted into the ferromagnet have sinusoidal terms with arguments of the form $(k_\uparrow - k_\downarrow)x$. This implies that the spin will precess in the ferromagnet with period $2\pi/(k_\uparrow - k_\downarrow)$ (since spin-up and spin-down have different energies due to the exchange splitting). This leads to rapid classical dephasing of the transverse spin component, typically over a length scale of a few atomic spacings in a $3d$ ferromagnet. Consequently, the entire transverse component of the spin current is absorbed by

24

the ferromagnet, and the spin current transmitted out of the ferromagnet is polarized with moment parallel to the magnetization. The total absorption of the transverse component leads to an expression for the torque per electron of the form

$$\mathbf{N} = AC\frac{\hbar^2}{2m}sin(\theta)\hat{\mathbf{x}} \tag{1.9}$$

where A is the area of the ferromagnet (in a cross-section perpendicular to $\hat{\mathbf{x}}$). Equation 1.9 is a good approximation for all-metallic systems. A number of differences exist between the physics of spin-torque in all-metallic systems and in magnetic tunnel junctions. In particular, in MTJ's there exists an additional contribution to the torque, along the $\hat{\mathbf{y}}$ direction, which in metallic systems is negligibly small. Since the devices studied for this dissertation are all-metallic, I will not discuss the specifics of MTJ's here. However, comprehensive reviews of STT in MTJ's can be found in references [20] and [46].

The torque given by equation 1.9 is only a starting point to understanding the effects of STT in a real device. Since electrons in a normal metal are spin-unpolarized, the incident spin current is zero and so the torque would in general entirely vanish[4] in a device consisting of a single normal/ferromagnet bilayer. Thus, all practical multilayer devices use the spin valve geometry, consisting of a ferromagnet/normal/ferromagnet trilayer. As mentioned earlier, in this case, it is necessary to consider the effect of multiple scattering events at the normal/ferromagnet interfaces. It is also important to consider whether transport through the normal spacer is ballistic or diffusive, and whether the structure is symmetric or not (some of the resulting expressions can be found in [50] and

---

[4]In normal/ferromagnet/normal junctions spin wave instabilities [47, 48] that may even induce switching [49] can occur if the two normal metals have different parameters, thus breaking the symmetry of the junction and the associated spin accumulations on either side of the ferromagnet. This type of structure has two main drawbacks: it requires larger currents to operate and generates only a small signal, by the AMR mechanism.

references therein). The basic form of the rate of change of the magnetization[5] (for an asymmetric trilayer with ballistic transport across the normal spacer) is

$$\left(\frac{\partial \mathbf{M_1}}{\partial t}\right)_{STT} = -g_1(\theta)\frac{\gamma_0 \hbar I}{eV_1}\hat{\mathbf{M}}_\mathbf{1} \times \left(\hat{\mathbf{M}}_\mathbf{1} \times \hat{\mathbf{M}}_\mathbf{2}\right) \qquad (1.10)$$

where V_i is the volume of ferromagnetic layer i, e is the elementary charge, I is the applied current, γ_0 is the gyromagnetic ratio, $\hat{\mathbf{M}}_\mathbf{i}$ are unit vectors for the magnetization of the two ferromagnetic layers, and $g_i(\theta)$ is an expression that depends on the details of the structure. It has the form [50]

$$g_i(\theta) = \frac{q_{+,i}}{A + B\cos(\theta)} + \frac{q_{-,i}}{A - B\cos(\theta)} \qquad (1.11)$$

with parameters A, B, $q_{+,i}$, $q_{-,i}$ that can be computed given the details of the structure, or can be obtained by fitting to experiment (although this is not easy for largely asymmetric structures).

1.3.4 A few words on the relative efficiencies of spin-torque and the Oersted field torque

An important and technologically advantageous feature of spin-torque is that the effect becomes stronger as device size shrinks. A relevant length scale that can be used to make this statement more quantitative is the radius R_b at which the spin-torque and the torque due to the Oersted field at the boundary of a cylindrical device are equal. Assuming a uniform current density along the axis of a magnetic element with radius R and a thickness L, and assuming

---

[5]Strictly speaking the magnetization is not proportional to the spin, as assumed here. The magnetization depends on both the spin and the orbital angular momenta, which are not generally collinear. However, because the orbital angular momentum is relatively small in $3d$ ferromagnets, it is a reasonable approximation to ignore it. This is not the case for ferromagnetic semiconductors.

the maximum possible values of both torques as a function of the magnetization orientation, the Oersted field torque at the boundary (the Oersted field increases linearly with radial position away from the center of the cylinder, so at the disk boundary it reaches its maximum value) equals the spin-torque when $R_b = \frac{\hbar P}{\mu_0 |e| L M_s}$, where P is the spin-polarization of the current and M_s is the saturation magnetization of the ferromagnetic layer being considered here (i.e. magnetic moment density per unit volume at saturation). For a 5 nm thick Permalloy layer, R_b is about 30 nm. Since the Oersted field torque decreases as $1/R$, while the spin-torque has a $1/R^2$ dependence, the latter dominates the former at the boundary (and hence even more so inside the disk) when the device radius is smaller than R_b. This discussion assumes that the magnetic layer that feels the spin torque is thin. If this layer is too thick the spin-torque, which is primarily an interfacial effect in spin valves, will not directly affect the magnetization far from the surface from where the spin-polarized current is incident. Instead, far away from this interface the magnetization would feel the effect of the spin-torque only indirectly (i.e. as torques transmitted from the interface via the exchange interaction and local internal fields), while the effect of the Oersted field would still be direct since the latter is a bulk effect. In fact the devices studied for this dissertation have such a thick magnetic layer, and as I will explain in the following chapters this leads to significant and beneficial effects due to the Oersted field.

1.3.5 Equation of motion of the magnetization

In the absence of STT the classical dynamics of the magnetization are typically described by using the phenomenological Landau-Lifshitz-Gilbert equation. In

the case where STT is also present, equation 1.10 is introduced as a third term (τ_{STT}), giving the final form

$$\left(\frac{\partial \hat{\mathbf{M}}_{\mathbf{1}}}{\partial t}\right) = -\gamma_0 \hat{\mathbf{M}}_{\mathbf{1}} \times \mathbf{H}_{\mathbf{eff}} + \alpha \hat{\mathbf{M}}_{\mathbf{1}} \times \left(\frac{\partial \hat{\mathbf{M}}_{\mathbf{1}}}{\partial t}\right) - g_1(\theta) \frac{\gamma_0 \hbar I}{e V_1 M_{S1}} \hat{\mathbf{M}}_{\mathbf{1}} \times \left(\hat{\mathbf{M}}_{\mathbf{1}} \times \hat{\mathbf{M}}_{\mathbf{2}}\right) \quad (1.12)$$

The first term describes the torque (τ_H) that leads to Larmor precession of the magnetization around the total effective field $\mathbf{H}_{\mathbf{eff}}$ and the second term (τ_d) describes classical damping of the magnetization oscillations, as introduced by Gilbert (with α being ~0.01 for a typical 3d ferromagnet). In order to highlight the dynamic effects, the equation is written in terms of $\hat{\mathbf{M}}_{\mathbf{i}}$, which is a unit vector in the direction of the magnetization vector $\mathbf{M}_{\mathbf{i}}$. Fig. 1.12 illustrates the torques acting on a magnetic moment and their approximate orientations. As can be seen, the spin torque can act either as a source of positive damping , or as a source of negative damping (opposing the Gilbert damping), depending on the current polarity. Equation 1.12 describes the dynamics of a single-domain magnet. In general, magnets, even at the nanoscale, are not truly single-domain, although they can be close under certain conditions. This will be discussed in more detail in the next chapter. In cases where the magnetization is not uniform, one typically still employs equation 1.12, but with the understanding that it is only valid locally. This leads to the so-called micromagnetic description of magnetization dynamics, in which a larger magnetic structure is discretized into elements that are small enough to be considered single-domain. This approach to modeling magnetization dynamics will be discussed in more detail in the chapters that deal with the new experimental results presented in this dissertation.
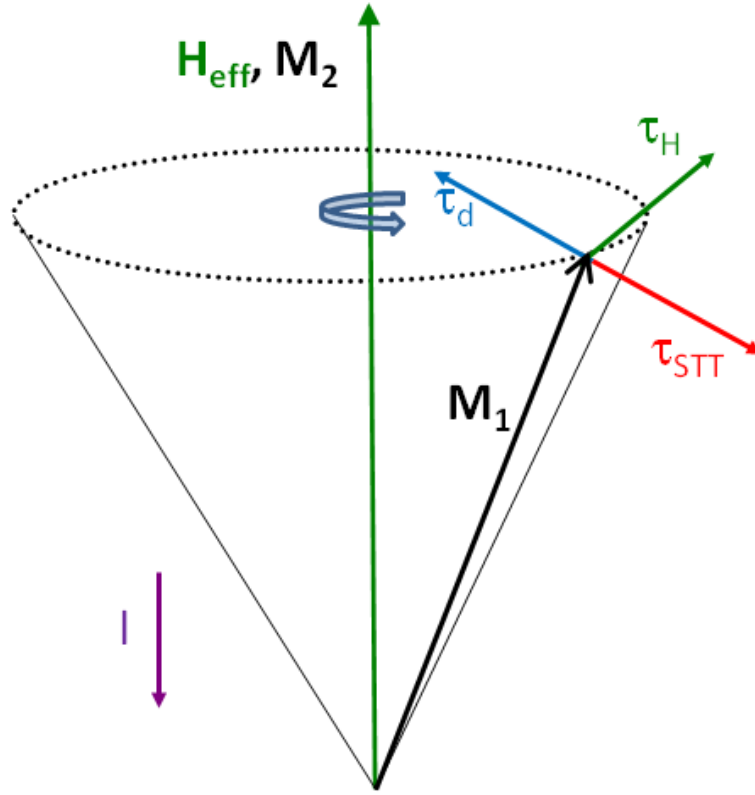
Figure 1.12: Directions of the torques on a magnetic moment.

Magnetic damping

Before moving on to a discussion of the two main classes of dynamics that can be expected from equation 1.12, I would like to give a brief description of the meaning and the physical origins of magnetic damping. The Gilbert form of the damping term[6] describes the fact that, in the absence of an external excitation, the magnetization tends to relax to the direction of the effective field over a time $1/(\alpha\omega)$, where ω is the angular Larmor precession frequency. The damping term is also responsible for the finite width of ferromagnetic resonance (FMR) peaks. From a formal point of view Gilbert damping is similar to a drag force

---

[6]The original form proposed by Landau and Lifshitz has a slightly different form (see, e.g. [20]).

proportional to the velocity (or, in this case the rate of change of the magnetization). This form was chosen essentially because it is the simplest, but without any significant insight into its microscopic origins. There is still no general consensus on how correct it is, especially for dynamics where the magnetization forms a large angle with respect to the effective field or in the case of strongly-nonuniform magnetic configurations. From a microscopic point of view, two main types of damping have been suggested. The first deals with so-called extrinsic contributions, in which, for example, two-magnon scattering from inhomogeneities is considered as a means for energy loss out of a particular mode of oscillation (thus damping out that mode) [51]. Another source of extrinsic damping is due to the so-called spin-pumping effect, which occurs as the precessing magnetization emits spin-waves that travel into the neighboring normal layers [52]. The second type deals with intrinsic damping. The dominant model ascribes the main source of damping to spin-orbital torque correlations and electron-hole pair generation [53] and appears to give good agreement with experiment for 3d ferromagnets and magnetic semiconductors [54, 55].

1.3.6   Switching between stable states

Hysteretic switching between stable states is generally studied in trilayer devices that have uniaxial anisotropy, typically due to their elongated shape, which leads to two possible configurations of the two ferromagnetic layers: parallel or antiparallel. Via GMR or TMR, one can easily distinguish between these two states, making such devices promising for applications as nonvolatile magnetic random access memory (MRAM) (see Fig. 1.13). This application has been the main driving force for the study of STT in magnetic trilayers,
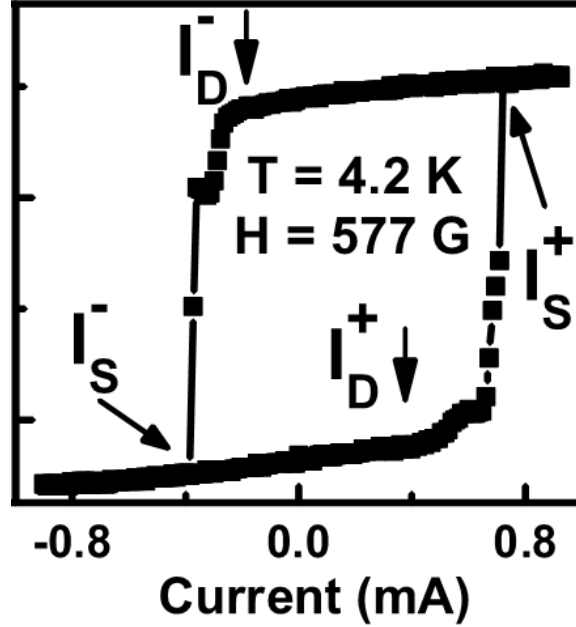
Figure 1.13: Example of transport data showing STT-induced switching between two stable states. (Modified from [56].)

both in academia and in the industry. The experiments performed for this thesis, however, deal with steady-state precession, so I will only give a very brief overview of the physics of switching. The geometry of choice for studying STT-driven magnetic switching is the spin-valve nanopillar (a ferromagnet/normal/ferromagnet CPP trilayer with lateral dimensions of ~100 nm), first demonstrated by Katine *et al.* in 2000 [44]. In a typical spin-valve nanopillar one of the magnetic layers is prevented from responding to the torques (referred to as the fixed or reference layer). This can be achieved by several different means: i) by making it thicker, ii) by using a magnetically harder material, or iii) by pinning it by means of exchange coupling to an antiferromagnetic layer. The second layer is designed to easily respond to the STT, while at the same time being sufficiently thermally stable to maintain its configuration after the current is removed. The switching process is thermally assisted for current pulses wider

than a few hundred picoseconds. Below this, the switching process is too rapid for thermal effects to play a significant role. Most of the recent work has been aimed either at reducing the critical currents required for switching (e.g. [57]) or at decreasing the switching times (e.g. [58]) (often one happens at the expense of the other, but optimization of both is expected to be possible).

1.3.7 Steady-state microwave-frequency self-oscillations

As mentioned above, the second type of dynamics that was predicted to be possible as a result of STT are steady-state oscillations of the magnetization under excitation by a direct (dc) current. Numerous experiments have indeed demonstrated this phenomenon in spin-valve devices [45, 59, 60, 61] than can have either the nanopillar or the point-contact geometry (see Fig. 1.14).
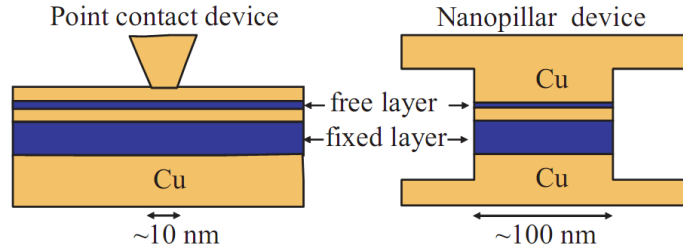
Figure 1.14: Comparison of the point-contact and nanopillar geometries used to study persistent oscillations driven by a dc spin-polarized current. (From [20].)

The initial experiments in nanopillar devices were performed at large applied fields. The devices were designed to have nearly single-domain magnetization. In this geometry, the persistent oscillations were observed for in-plane applied fields $H_{appl} > H_K$, where H_K is the in-plane shape anisotropy field i.e. the magnitude of the field required to saturate the magnetization along the in-plane

hard (short) axis of these elliptical devices. Under such conditions the current bias sign is chosen such as to favor switching the free layer antiparallel to the fixed layer, while the field is strong enough to oppose switching. Thus, one way to understand the persistent dynamics is that it results from the interplay of the two opposing factors, the field torque and the STT. The STT acts as an source of antidamping, canceling out the damping torque on average and thus allowing the magnetization to undergo undamped Larmor-like precession about the effective field (see Fig. 1.12). Because of the strong demagnetization fields associated with a flat magnet, the orbit is not circular, but rather has an elongated shape, as shown in Fig. 1.15.
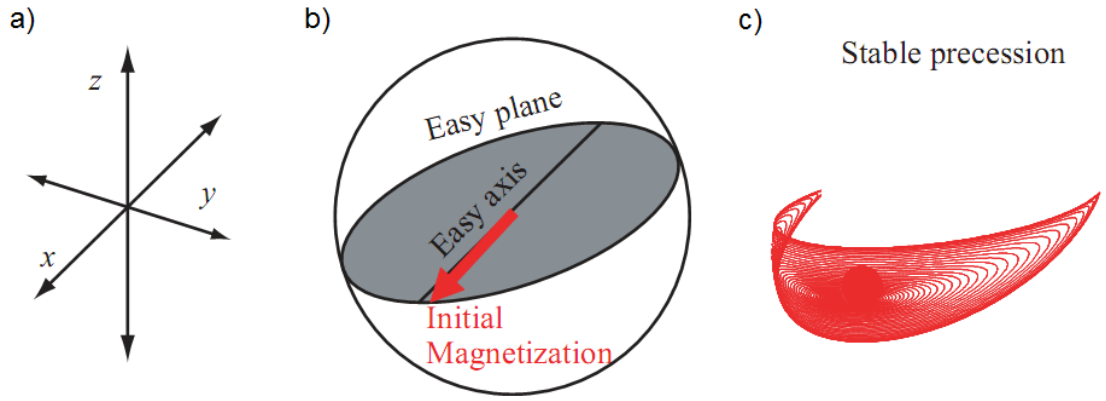
Figure 1.15: Illustration of the elongated orbits resulting from the demagnetization field effects. The easy axis is the x-axis and the hard axis is the out-of-plane (z) direction. (Modified from [20].)

The "natural" precession frequency of a single-domain magnet, taking into account anisotropy effects, is given by the so-called Kittel formula [62] (equation 1.13):

$$f = \frac{\gamma_0}{2\pi}\sqrt{(H_{appl} + H_K)(H_{appl} + H_K + 4\pi M_S - 2K_u/M_S)} \qquad (1.13)$$

where M_S is the saturation magnetization and K_u is the uniaxial anisotropy con-

stant associated with the out-of-plane direction. The "natural" Kittel frequency is affected (quite considerably) by the magnitude of the applied dc current (due to the nonlinearity of the STT), so that the dc-driven frequency is close to the Kittel frequency associated with H_{eff} only near the critical current for exciting the dynamics [63, 64].

Four main questions arise in connection with these dc-driven oscillations:

1. Is an applied field necessary to excite the oscillations or is it possible to design a device that does away with this requirement? Eliminating the need for an applied field could considerably reduce the fabrication complexity of a potential commercial device.

2. Is it possible to excite steady-state dynamics even when the magnetization deviates considerably from single-domain?

3. What are the mechanisms responsible for linewidth broadening, and how can the linewidth be minimized in order to obtained well-defined, sharp oscillation peaks?

4. Can the output power[7] (due to GMR or TMR) be made large enough to be of interest for applications?

I will discuss points 1. and 2. in the chapters dedicated to the experimental results. For now, I will just say the answer is positive to both questions. Point 3 is also integral to much of the work done for this thesis, and will be discussed in more detailed later, but I would first like to provide a brief theoretical

---

[7]Although, most often, the total power output is cited as a figure of merit, it is possible that the power density might be a better measure of the usefulness of an oscillator. For example, a very broad peak, with low power density can be much more difficult to distinguish against the noise background than a narrow peak with high power density relative to noise, although the former might have a greater total integrated power than the latter.

background immediately below. This will be followed by a brief discussion of approaches aimed at dealing with point 4.

Models for the linewidth broadening

The linewidth of a periodically-driven resonator is generally related in a relatively simple manner to damping. For example, starting from the LLG equation one obtains an expression for the ferromagnetic resonance (FMR) linewidth given by equation 1.14

$$\Delta f = 1.16\alpha f \qquad (1.14)$$

in the absence of anisotropies, where the factor of 1.16 is related to the Lorentzian shape of the FMR resonance and α is the Gilbert damping parameter [65].

In contrast, the linewidths of dc-driven oscillators (sometimes called self-oscillators or auto-oscillators), of which dc-driven spin-torque oscillators are examples, are generally the result of classical decoherence processes [66, 63], i.e. fluctuations of the oscillation frequency or amplitude (or both) over time. Thus, it is important to distinguish between the (perhaps) more familiar linewidth of a periodically-driven resonator and the linewidth of a dc-driven oscillator, since the two have very different physical meanings. In the rest of this dissertation the word linewidth will be used to refer exclusively to the auto-oscillation linewidth of a dc-driven oscillator. The sources of decoherence in spin-torque oscillators are either related to temperature effects (see [67] or [63] and references therein) or to chaotic effects. The chaotic effects have been studied mainly using micro-magnetic simulations [68, 69]. The temperature effects have also been studied analytically and can be divided into two broad types:

1. Those due to jumping between modes that are closely-spaced in frequency [67], for which the contribution to the linewidth can be described approximately by equation 1.15:

$$\Delta f = \frac{f}{2\pi^2} Exp\left(\frac{-E_B}{k_B T}\right) \tag{1.15}$$

where E_B is the energy barrier for jumping out of the precessional state with frequency f, k_B is the Boltzmann constant and T is the temperature.

2. Those based on the effect of Gaussian thermal noise in a nonlinear system, described in [63] and references therein. The details of the model are developed for single-domain oscillators. In general the linewidth needs to be computed numerically given the parameters of the oscillator, but there are two limiting cases that produce relatively simple expression for the temperature dependence. One of these is the case of low T and low Δf, where the linewidth is predicted to have the dependence given by equation 1.16

$$\Delta f \propto \frac{k_B T}{\mathcal{E}} \tag{1.16}$$

where $\mathcal{E}$ is the average energy in the oscillator. In the case of moderate temperatures and large linewidths, the predicted dependence is given by equation 1.17.

$$\Delta f \propto \sqrt{\frac{k_B T}{\mathcal{E}}} \tag{1.17}$$

A $T^{1/2}$ dependence was also derived earlier from different arguments [67], but there it was found to account for the experimental variation of the linewidth in the low (<110 K) temperature range. So far, the most comprehensive testing of the theoretical model from which equations 1.16 and 1.17 are derived was performed by Boone *et al.* in 2009 [70], who found a good agreement with experiment for moderate oscillation amplitudes ($< 70°$), at a bath temperature of 4.2 K, for bias conditions where only one oscillation mode was excited.

Experimentally, the narrowest linewidths do not occur in uniformly-magnetized nanopillar structures. Rather, they have been seen in the point-contact geometry ($\Delta f = 1.89$ MHz at $f = 34.4$ GHz for a 11000 Oe field [71], and $\Delta f = 0.58$ MHz at $f = 0.18$ GHz for a 25 Oe field [72]) or in nanopillars where the magnetization of one of the layers has a vortex configuration ($\Delta f = 0.28$ MHz at $f = 1.14$ GHz for a 480 Oe field [61]), which will be described in more detail in the chapters on experimental results. These are values obtained at room temperatures. In general, narrower values are obtained as the oscillators are cooled down, though a monotonic variation with temperature, which the model described in Ref. [63] predicts, is not always observed. Nanopillars with approximately single-domain magnetization typically have linewidths of tens to hundreds of MHz at frequencies, in the range of 3-6 GHz. It is not entirely clear why the single-domain nanopillars exhibit broader linewidths, but one factor may be the relatively smaller magnetic volume of the oscillating layers in these structures, which makes them more susceptible to thermal noise (c.f. equations 1.16 and 1.17, where $\mathcal{E}$ increases with the magnetic volume of the oscillating layer). The spatial structure of these oscillations also plays an important role[8]. A dramatic example of the role of the magnetic structure over purely thermal effects occurs in certain MTJ's with a very thin MgO insulating barrier [73], in which the linewidth can decrease by more than an order of magnitude after applying a large "conditioning" voltage bias. As Praveen Gowtham in our group has shown, this occurs as a result of the formation of highly-localized magnetic conduction channels across the barrier. More work on the role of the magnetic configuration has been undertaken by Oukjae Lee in our group, who has recently been modeling the coupling between different regions of an oscillating

---

[8]The role of the spatial configuration is taken into account in a simplified way by the model of Ref. [63], which makes predictions about the linewidth variation with the direction of the applied field.

layer, finding that linewidth broadening can be enhanced in cases where the intralayer coupling is weak, allowing different regions of the sample to oscillate at slightly different frequencies as a result of variations in the local effective field. I will describe additional findings from my own experiments in the results chapters.

Increasing the emitted power

As mentioned earlier, one of the main goals of current research in spin-torque oscillators is to increase the power output. Two main approaches have been taken in this direction. One is by moving from spin-valves to MTJ's. This was not possible until only about two years ago, because tunnel barriers with a low enough resistance-area product needed to sustain the required applied voltages without breaking down (~2 $\Omega\mu^2$) could not be fabricated. Recently, however, a number of experiments have demonstrated STT-driven oscillations [74, 73, 75]. The devices in Ref. [75] are the result of a natural step forward, combining the narrow linewidth of vortex oscillators [61] (its discovery and properties in spin valve nanopillars are described below, in the results chapter) with the large power output of MTJ, resulting in maximum output powers of ~5 nW, with a 1.1 MHz minimum linewidth at a frequency of ~0.77 GHz. This represents a power increase of about 3 orders of magnitude over a comparable spin valve vortex oscillator. The result is particularly encouraging since the MTJ's used in that study were relatively far (the maximum TMR value is only about 10%) from the state of the art (over 100% TMR for low resistance-area product barriers).

The second approach to increasing the power (and possibly improving the coherence) of the oscillations is the building of large arrays of spin-torque oscil-

lators that are phase-locked, in other words all oscillators in the array tend to synchronize and have the same frequency and phase. Phase-locking allows for
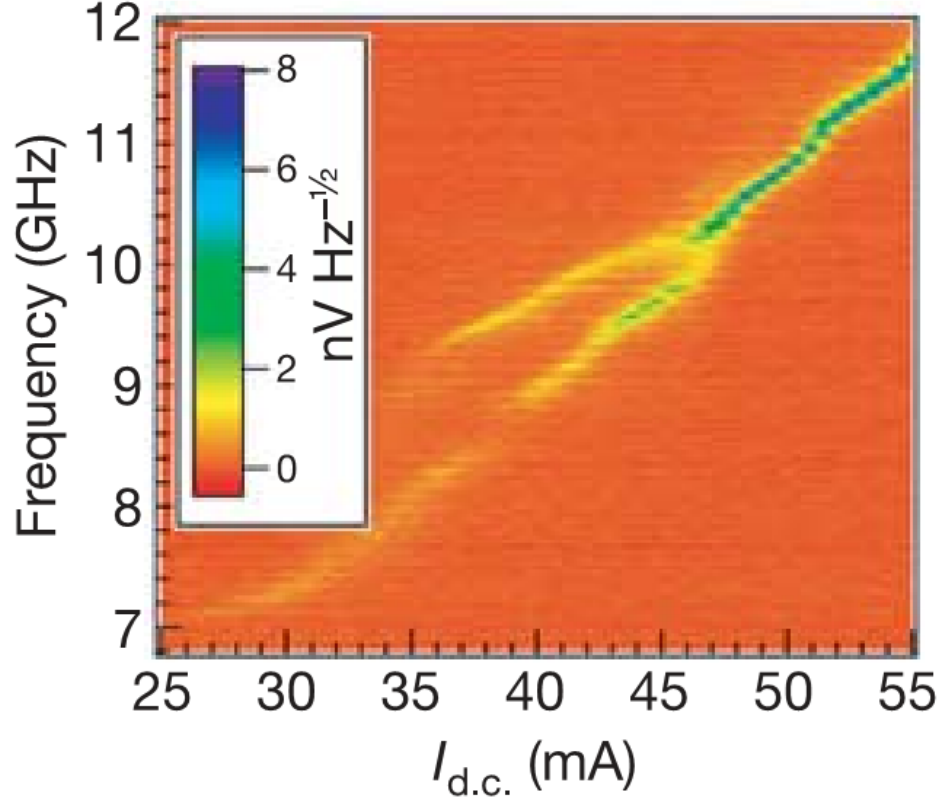
Figure 1.16: Illustration of phase-locking of 2 STT oscillators, with 80 nm nominal diameters, located at 150 nm from each other. The figure shows the two oscillators initially having different frequencies, and then phase-locking at a current bias value of ~46 mA. (Modified from [76].)

a faster-than-linear increase in the output power as a result of near-perfect correlations between the outputs of the oscillators. For example, for two oscillators, the total output power P_{1+2} would scale as

$$P_{1+2} = P_1 + P_2 + 2\sqrt{P_1 P_2} \tag{1.18}$$

where P_1 and P_2 are the output powers of the two oscillators in the absence of

synchronization. This coupling is possible because STT oscillators are nonlinear systems. The first experimental realizations of mutual phase coupling between 2 STT oscillators were published in 2005 [77, 76] (see Fig. 1.16). More recently, 4 vortex oscillators were phase locked by means of the antivortices formed between them, also in a point-contact geometry [78]. While these examples rely on coupling by means of spin waves emitted by the different oscillators, the coupling mechanism could also occur be by means of dipolar field interactions, or electric coupling [79], that is by means of the oscillatory voltage produced by the STT devices. These mechanisms have not yet been demonstrated experimentally, the difficulties being, for the former, that it is difficult to fabricate nanopillars that are close enough to each other to couple by fields, and for the latter, that the emitted electric signal is generally too weak to allow efficient coupling (with the possible exception of MTJ's). In addition, a major challenge for the realization of any large array of phase-coherent STT oscillators results from the broad distribution of the properties of these oscillators, as fabricated.

1.3.8   Spin-transfer outside the trilayer paradigm

Spin-transfer torques have also been studied in metallic nanowires, where they can induce translation of domain walls, or in ferromagnetic semiconductors (typically the p-type ferromagnetic III-V semiconductor (Ga,Mn)As). Below, I will give a very brief overview of spin-transfer in metallic nanowires. Detailed reviews can be found, for example in Ref. [80] (domain wall motion) and [81] (semiconductors).

STT and domain walls

The main difference between STT in trilayers and STT in single-layer ferromagnetic metallic nanowires is the form of the spin-torque in the equation of motion. This is due to the fact that the magnetization vector in wires varies continuously, unlike the abrupt transitions between layers in a nanopillar or point-contact geometry. Thus, instead of the last term in equation 1.12, the torque takes the form given by equation 1.19

$$\tau_{DW} = -(\mathbf{v_J} \cdot \boldsymbol{\nabla})\hat{\mathbf{M}}(\mathbf{r}) + \beta\hat{\mathbf{M}}(\mathbf{r}) \times (\mathbf{v_J} \cdot \boldsymbol{\nabla})\hat{\mathbf{M}}(\mathbf{r}) \tag{1.19}$$

where $\mathbf{v_J} = -(\gamma_0\hbar P|\mathbf{J}|)/(2eM_S)$, $\mathbf{J}$ is the charge current density vector and P is the spin polarization [20, 80]. For a uniform current density, the domain wall undergoes translation at speed v_J (for J larger than a certain threshold value). The second term describes two additional contributions: i) the contribution to the torque when the spin current cannot follow the local magnetization adiabatically (this is significant in structures with large magnetization gradients), and ii) an additional contribution due to damping effects. The magnitude of β is currently a matter of debate, partly because its effects are not easy to separate experimentally from the non-adiabatic effects, which depend both on the equilibrium structure of the domain wall, and on its deformation as it encounters wire defects in its path. In the presence of a non-zero β factor, the intrinsic threshold for initiating domain wall motion in a defect-free wire becomes zero. Thus a large β factor would be of importance for potential applications.

CHAPTER 2

A BRIEF INTRODUCTION TO MAGNETIC VORTICES

2.1 What is a magnetic vortex?

A magnetic vortex is a type of magnetization distribution characterized by an in-plane curling of the local moment. An ideal magnetic vortex has zero out-of-plane component everywhere except in the central region (the core) (see Fig. 2.1). It is characterized by two topological charges: i) the chirality, C, which refers to the direction of curling of the in-plane magnetization, and ii) the polarity, p, which refers to the orientation of the out-of-plane core magnetization[1]. In general the polar angle of the magnetization, $\theta(\mathbf{r})$, can be approximated by a bell-shaped function, such as the one suggested in Ref. [83]:

$$\theta(\mathbf{r}) = \begin{cases} 2p \ tan^{-1}(r/R_c) & r < R_c \\ p\frac{\pi}{2} & r \geq R_c \end{cases} \tag{2.1}$$

where r is the radial coordinate in the disk plane and R_c is the core radius.

2.1.1 Energy contributions

In order to understand under what conditions magnetic vortices can form, it is necessary to look at the contributions to the free energy of a magnet. The most important contributions are given by equation 2.2:

$$E_{TOT} = E_{EX} + E_{M-S} + E_Z + E_{M-C} \tag{2.2}$$

---

[1]A third topological charge, the vorticity is used to distinguish between a vortex and an antivortex. In an antivortex the magnetization curls anti-clockwise if one moves around the core in a clockwise direction.
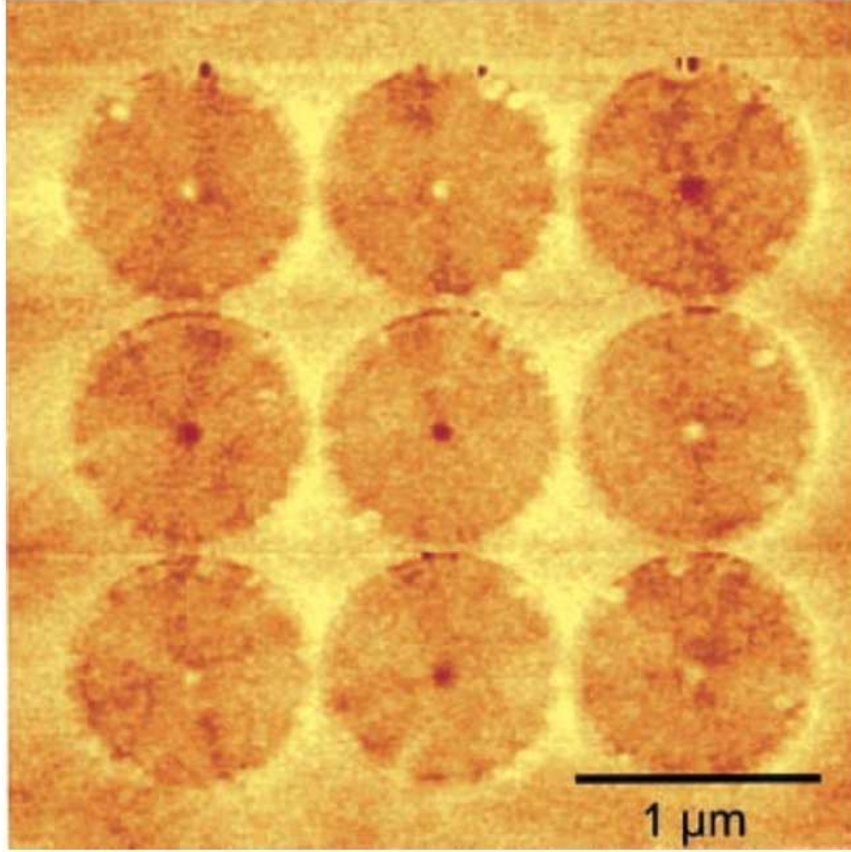
Figure 2.1: Magnetic force microscopy (MFM) image of a vortex in a 50 nm thick $Ni_{80}Fe_{20}$ micro-structure. The contrast varies from light to dark via orange, indicating the out-of-plane magnetization. The vortex core was resolved here for the first time. (From [82].)

where E_{EX} is the exchange energy, which in a ferromagnet is minimized for parallel orientation of nearest neighbors, E_{M-S} is the magneto-static energy, E_Z is the Zeeman energy due to the applied field, and E_{M-C} is the magneto-crystalline anisotropy energy, which favors orientation of the magnetization along certain crystallographic directions. In Py, E_{M-C} is very close to zero and can be ignored. At zero field, the magnetic configuration will then be primarily determined by the interplay between the exchange and magneto-static contributions.

The magneto-static contribution is minimized when the magnetization at the edges of the structure is parallel to the edges, resulting in total magnetic flux closure within the ferromagnetic material, but this of course increases the exchange energy. In small structures, where the required radius of curvature would be very small, the exchange energy cost for following the surface is high, so the magnetization tends to remain uniform. For larger structures, however, the magneto-static contribution is more significant, while the larger radius of curvature results in a lower exchange cost associated with the flux closure configuration, so the magnetization curls into a vortex.

The dimensions at which the transition between the single-domain and the vortex configuration occurs in the phase diagram are usually expressed in term of the "exchange length," $l_{ex} = \sqrt{A/(2\pi M_s)}$ [84], which for Py is about 4 nm (here A is the exchange constant, which characterizes the strength of the ferromagnetic exchange interaction)[2]. The core, which points out-of-plane in order to avoid the very large exchange energy associated with anti-parallel in-plane moments, has a radius R_c of approximately $3l_{ex}$. In even larger magnetic structures, the surfaces (and overall shape of the ferromagnet) will still affect the magnetization, but more complex domain structures can occur, with effects due to the magneto-crystalline anisotropies and crystal structure becoming more important.

---

[2]Reference [84] describes the phase diagram for the transition from a single-domain to a vortex configuration in the case of a circular disk. Although the result has, in general, a complicated form it has a relatively simple asymptotic behavior for the case of a very thin disk compared to l_{ex}. In this limit the maximum single-domain radius R_{SD}^{max} is predicted to vary as $R_{SD}^{max} = l_{ex}^2/(0.7\pi L)$, where L is the disk thickness.

2.1.2 Quasi-static field-driven reversal

The quasi-static reversal of the magnetization involving vortex formation is very different from reversal through uniform rotation of a single-domain, as illustrated in Fig. 2.2. This provides an important means of identifying the pres-
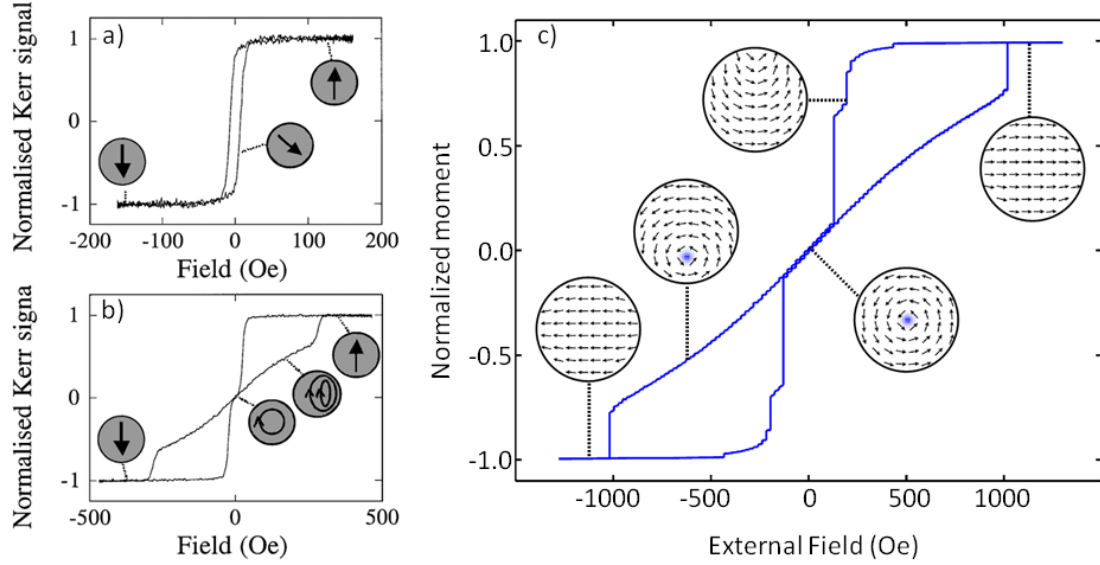
Figure 2.2: Quasi-static magnetization reversal loops comparing the single-domain and a vortex cases. a), b) Normalized Kerr microscopy loops (signal is proportional to normalized magnetization) for two 10 nm thick disks with composition $Ni_{80}Fe_{14}Mo_5$, showing a) a single-domain reversal mechanism for a 100 nm diameter sample, and b) a vortex reversal mechanism for a 300 nm diameter sample. (Modified from [85].) c) Simulated vortex reversal loop for a magnetic disk, showing the micromagnetic configuration at key parts of the loop. (Modified from [86].)

ence of a vortex even when the magnetization configuration cannot be readily imaged, as I will describe in the next chapter. In the case of uniform rotation of a single-domain, only one hysteresis loop is observed (Fig. 2.2a)). Reversal via a

vortex state, involves two hysteresis loops (Fig. 2.2b)). These correspond to the nucleation (annihilation) of the vortex at low (high) values of the applied field. The region between the two annihilation fields is reversible. It corresponds to the displacement of the vortex core towards the edge of the dot as the vortex is deformed such that region having magnetization nearly parallel to the applied field increases, while the opposite region shrinks. Vortex annihilation occurs when the core reaches the edge of the dot and is forced out.

2.2 Fundamental dynamic excitations of a magnetic vortex

The dynamic excitations of a magnetic vortex can be classified according to three main types according to their symmetry: i) a translational mode (precession of the core), ii) radial modes (nodes of the spatial distribution of the spectral power of the magnetization oscillations occur along the radius), and iii) azimuthal modes (nodes occur along the circumference). The experiments performed for this thesis deal exclusively with the first type, the translational (gyrotropic) mode. Next, I will provide some background on this mode.

2.2.1 Gyrotropic mode

The lowest frequency excitation of a magnetic vortex corresponds to a precession of the vortex core around its equilibrium position and is referred to as the gyrotropic mode. It was first experimentally observed (by means of magnetic imaging) in 1984 by Argyle *et al.* [87] in a 800 nm thick easy-plane garnet film, where a vortex formed at the intersection between two 90° Néel walls. The first

observation in an microstructure containing only the vortex was made by Park *et al.* in 2003, using time-resolved Kerr microscopy on single-layer Py disks with a thickness of 60 nm and diameter ranging between 500 nm and 2 μm [88]. This study used short magnetic field pulses to excite the vortex and then detected the relaxation back to equilibrium. Figure 2.3 shows these results.
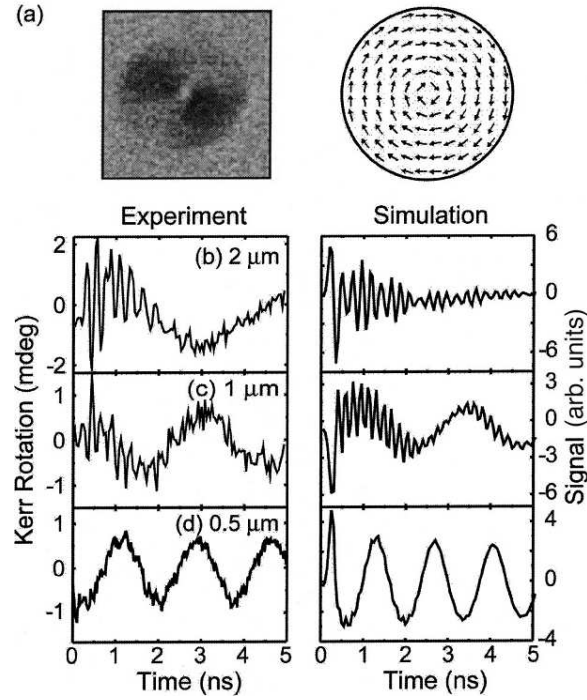
Figure 2.3: Observation of the gyrotropic mode of an isolated vortex. a) Magnetic force microscope image of the static vortex in a 500 nm diameter Py disk (left), and simulated structure (right). b), c) and d) show the time dependence of the Kerr rotation (proportional to the magnetization) (left) and the simulated magnetization (right) near the center of the disk, for three different diameters (indicated on the figure). The low-frequency component of the time traces is due to the gyrotropic mode. (From [88].)

Thiele-Huber analytical approach

The most common analytical model used to study the gyrotropic mode is based on an approach for calculating the dynamics of a moving magnetic structure developed by Thiele in 1973 [89]. Starting from the Landau-Lifshitz-Gilbert equation, he derived an equation for the forces acting on a magnetic structure that is assumed to move *without* distortion, which essentially states that the net force is zero for an inertia-free vortex:

$$\mathbf{F^g} + \mathbf{F^r} + \mathbf{F}^\alpha = 0 \tag{2.3}$$

In this equation $\mathbf{F^g} = \mathbf{G} \times \mathbf{v}$ is a Magnus-type force acting perpendicular to the velocity ($\mathbf{v} = d\mathbf{X}/dt$, where $\mathbf{X}$ is the position of the vortex core with respect to the center of the disk) of the magnetic structure, $\mathbf{F^r} = \frac{\partial W}{\partial \mathbf{X}}$ is the reversible force on the magnetic structure (due to external applied field as well as internal effects, such as exchange energy, internal magnetostatic energy etc), and $\mathbf{F}^\alpha = \tilde{\tilde{\mathbf{D}}} \cdot \mathbf{v}$ is the dissipative force; $\mathbf{G}$ is the gyrocoupling vector, W is the energy of the displaced vortex, and $\tilde{\tilde{\mathbf{D}}}$ is the dissipation dyadic. In polar co-ordinates, the expressions for $\mathbf{G}$ and $\tilde{\tilde{\mathbf{D}}}$ are given by equations 2.4 and 2.5

$$\mathbf{G} = -\frac{M_s}{\gamma_0} \int sin\theta(\mathbf{r})\nabla\theta(\mathbf{r}) \times \nabla\phi(\mathbf{r}) \, d\mathbf{r} \tag{2.4}$$

$$\tilde{\tilde{\mathbf{D}}} = -\frac{\alpha M_s}{\gamma_0} \int \left(\nabla\theta(\mathbf{r}) \otimes \nabla\theta(\mathbf{r}) + sin^2\theta(\mathbf{r})\nabla\phi(\mathbf{r}) \otimes \nabla\phi(\mathbf{r})\right) \, d\mathbf{r} \tag{2.5}$$

where $\theta(\mathbf{r})$ and $\phi(\mathbf{r})$ are the polar and azimuthal angles of the local magnetization, respectively, at position $\mathbf{r}$ (α is the Gilbert damping parameter). In the harmonic approximation, the restoring force $\mathbf{F^r}$ will take the form

$$\mathbf{F^r} = -\frac{\partial W}{\partial \mathbf{X}} = -\kappa\mathbf{X} \tag{2.6}$$

for a positive constant κ that depends on the total energy of the displaced vortex, and which I describe more detail further below. In the case of weak damping

the angular frequency of the gyrotropic mode is then given by:

$$\omega_G^0 = \frac{\kappa}{|\mathbf{G}|} \tag{2.7}$$

Equation 2.6 for W is, of course, only valid for a circular disk. In the case of an ellipse there are two different constants, one for displacements of the core along the major axis (κ_M) and one for displacement along the minor axis of the ellipse (κ_m), with the frequency being determined by equation 2.7 with an effective constant $\kappa_{eff} = \sqrt{\kappa_M \kappa_m}$. Due to the lower confinement of the core along the major axis of the ellipse than along the minor axis, κ_M is expected to be smaller than κ_m. This is confirmed by the micromagnetic simulation studies in Ref. [90].

Thiele's formalism was applied by Huber [91] to the specific case of a 2-dimensional vortex (with 3-component spins) in the continuum approximation [92]. Using $\nabla\phi(\mathbf{r}) = q\hat{\phi}(\mathbf{r})/r$ (q is the vorticity topological charge, which is 1 for a vortex and -1 for an antivortex), and the assumption that the spins lie in plane far from the vortex core and are perfectly out-of-plane at the core, he found that $\mathbf{G}$ is given by a very simple expression:

$$\mathbf{G} = -2\pi \frac{M_s L}{\gamma_0} q p \hat{\mathbf{z}} \tag{2.8}$$

where p is the vortex core polarity (± 1) and L is the disk thickness. Only the values of $\theta(\mathbf{r})$ at the boundary and at the center are necessary for the calculation of $\mathbf{G}$ in the case of a 2-dimensional vortex. Since the dominant contribution to $\tilde{\mathbf{D}}$ comes from the region far away from the core, where the spins are nearly in-plane and $\theta(\mathbf{r})$ has only a small gradient, $\tilde{\mathbf{D}}$ becomes a diagonal tensor:

$$D_{xx} = D_{yy} = D = -\frac{\alpha M_s L}{\gamma_0} \pi ln\left(\frac{R}{a}\right) \tag{2.9}$$

where R is the outer radius of the vortex and a is the lattice parameter of the system. (The expressions above are actually for a thin disk of thickness L where

there is no variation in the spin structure along the thickness. In the case of an infinitely thin 2-d disk the factor of L would be absent from these expressions and M_s would have the meaning of magnetic moment density per unit area.)

The restoring energy term W was first computed only about nine years ago by Guslienko, Metlov *et al.*. There are two main methods for estimating W for a 2-dimensional vortex. The first method (usually referred to as the *rigid vortex approximation*) [93] assumes that the vortex is rigid and consequently moves without deformation, while the second method (usually referred to as the *surface charge free* or *two-vortices* approximation) [84] assumes that the vortex deforms dynamically during its motion in order to satisfy the strong pinning conditions at the disk boundary (i.e. no surface magnetic "charges"). The second model provides better agreement with micromagnetic simulations and experiment for isolated dots [94, 95], but cannot account for coupling between vortices in arrays of adjacent disks. It predicts an oscillation frequency, which for disks with small thickness L compared to the radius (i.e. $\beta = L/R$ is small) takes the approximate form [94, 96]:

$$\omega_G^0 = \frac{20}{9}\gamma_0 M_s \beta (1 - \frac{4}{3}\beta) \tag{2.10}$$

which is in good agreement with experiment for $\beta \leq \sim 15\%$. For larger aspect ratios the analytical method increasingly overestimates the frequency, as a result of the gradual failure of the various approximations made under the assumption of a 2-dimensional vortex structure [95]. The devices studied for this thesis have aspect ratios on the order of unity, and consequently the analytical predictions are not quantitatively accurate. In some cases, the analytical predictions can even be qualitatitvely inaccurate. This is a direct consequence of the small lateral dimensions that are, as mentioned in the previous chapter, characteristic of spin-torque nanopillars. I will discuss the effects of the small dimensions in

detail in the chapters dedicated to my experimental results.

2.2.2 Radial and azimuthal modes of magnetic vortices

Under excitation by magnetic fields radial and azimuthal modes of vortices have also been observed. In the case of these modes the magnetization dynamics do not correspond to a translation of the vortex core. The radial
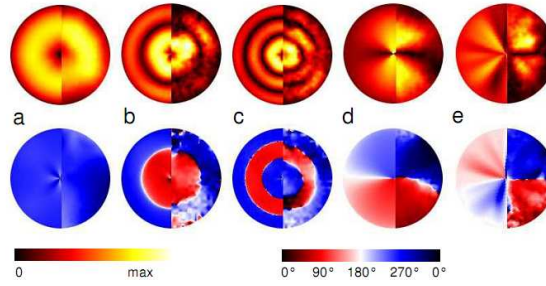
Figure 2.4: Images of radial and azimuthal modes of a vortex in a single-layer Py disk with a radius of 3 μm and thickness of 15 nm, showing the amplitude of the modes on the top row and the phase on the bottom row. The modes were excited by locally-generated magnetic field pulses. Due to the spatial nonuniformity of the pulses, azimuthal modes are also excited, although the field is predominantly out-of-plane. The left part of each image is obtained by micromagnetic simulations and the right part by Fourier transform Kerr imaging. a) Radial mode with 1 node, and f = 2.80 GHz. b) Radial mode with 2 node, and f = 3.91 GHz. c) Radial mode with 3 nodes, and f = 4.49 GHz. d) Azimuthal mode with 1 node, and f = 2.08 GHz. Two such orthogonal, degenerate modes can be excited due to the symmetry of the disk. (The degeneracy is lifted by interaction with the gyrotropic mode for smaller disk sizes [97].) e) Azimuthal mode with 2 nodes, and f = 1.69 GHz. (From [98].)

modes are excited most efficiently by an axial field [99, 100], while the azimuthal modes are excited most efficiently by an in-plane field [100, 97]. Fig. 2.4 illustrates the spatial structure of these two types of modes, obtained by Fourier transform imaging [101]. These modes cannot be studied based on the Thiele-Huber formalism. Instead, the typical analytic approach involves a treatment of small deviations from the static vortex magnetization and computation of magnon eigenstates with cylindrical symmetry [102, 103, 104].

2.3 Spin-torque driven vortex oscillations

2.3.1 Overview

While the initial experimental studies of vortex dynamics all used magnetic fields (either short pulses or continuous ac fields at resonance) to investigate their dynamics, in the last few years increasing attention has been given to spin-torque as a means of exciting vortex dynamics. Spin-torque, as discussed earlier, is more efficient and can also lead to different types of dynamics than those excited by magnetic fields, as a result of its different angular dependence.

The first published work on using spin-torque with magnetic vortices was a series of calculations published by Shibata *et al.* in 2006 [105]. In the case of a dc current applied in the CIP geometry by normal leads attached to the edges of a single-layer magnetic disk, they predicted a reversible displacement of the vortex perpendicular to the current direction, occurring via a spiral motion (around an axis perpendicular to the plane and centered at the final position of the core) whose direction of rotation depends on the core polarity and sign of the cur-

rent. The direction of the final displacement and its magnitude depend on the current magnitude and sign, respectively (the direction of displacement also depends on the vortex polarity). The spiral motion would occur at the gyrotropic frequency. Interestingly, they predict the absence of an intrinsic critical current (unlike domain wall motion or switching of a uniform nanomagnet discussed in the previous chapter). In 2006, the first experimental observation of the resonant excitation of the gyrotropic mode by an ac current was also made [106], in the geometry discussed above. Detection was relatively inefficient, being due to the AMR effect.

The possibility of exciting the gyrotropic precession in a spin valve structure by means of a dc current, which had not been previously predicted, was demonstrated in 2007 [107, 61]. Chapter 3 describes the details of this experiment. Around the same time the spin torque team at NIST also published results suggesting a *possible* observation of gyrotropic precession in the point-contact geometry [108, 72]. In 2008, Mistral *et al.* [109] published additional results that demonstrated dc-driven gyrotropic oscillations in point-contacts, and presented an analytical model of the spin-torque effects (for a CPP spin valve in the point-contact geometry) grafted to the Thiele-Huber approach. Their calculations predict that an in-plane spin polarization can lead only to a stable vortex translation, but not to oscillations, which would instead require an out-of-plane component of the spin polarization. Experimentally, I found that this does not hold, at least in our nanopillar devices. I will describe a possible way to reconcile this discrepancy in Chapter 5. This could occur in conjunction with another possible solution, which was suggested recently by Khvalkovskiy *et al.* [110]. They show analytically that a sufficiently non-uniform static polarizer[3] config-

---

[3]The term polarizer is used in this thesis to refer to the ferromagnetic layer of a CPP spin valve that does not have a stable vortex configuration, i.e the thinner layer in the devices dis-

53

uration can also lead to persistent precession of the vortex, even when the polarization is entirely in-plane. The results of that study also show that even a uniform, in-plane spin polarization can excite persistent dynamics, provided it varies in time.

2.3.2 Analytical description of vortex core precession driven by spin-torque

Expressions for the force due to the spin current

Earlier in this chapter I introduced equation 2.3, which describes the precessional dynamics of the vortex core. Although that equation can be used to calculate the gyrotropic frequency it cannot be used to determine the complete motion of the vortex because it includes no driving term. Here, I would like to describe briefly the role of adding a fourth term, $\mathbf{F}^{st}$, due to the spin-torque, which acts so as to cancel out the damping, leading to steady-state precession of the core upon application of a dc current bias. In the Thiele-Huber approach, this term has the form [109]

$$\mathbf{F}^{st} = \mathbf{F}^{st}_\perp + \mathbf{F}^{st}_\parallel = \frac{\hbar PI}{2|e|LR^2}(\mathbf{f}^{st}_\perp + \mathbf{f}^{st}_\parallel) \tag{2.11}$$

where $\mathbf{f}^{st}_\perp$ and $\mathbf{f}^{st}_\parallel$ are the given by:

$$\mathbf{f}^{st}_\perp = \int \eta_\perp(\mathbf{r})\sin^2\theta(\mathbf{r})\nabla\phi(\mathbf{r})\,d\mathbf{r} \tag{2.12}$$

and

$$\mathbf{f}^{st}_\parallel = -\int \eta_\parallel(\mathbf{r})\left(\nabla\theta(\mathbf{r})\sin\phi(\mathbf{r}) + \frac{1}{2}\nabla\phi(\mathbf{r})\sin2\theta(\mathbf{r})\cos\phi(\mathbf{r})\right)d\mathbf{r} \tag{2.13}$$

cussed in the experimental chapters.

Here P is the magnitude of spin polarization of the current, I is the applied current, e is the electron charge, $\eta_\perp(\mathbf{r})$ is the normalized component of the incident spin polarization perpendicular to the device plane and $\eta_\parallel(\mathbf{r})$ is the normalized component in the plane. One implication of equations 2.12 and 2.13 is that for a planar polarizer ($\eta_\perp(\mathbf{r}) = 0$) the torque acts on the vortex core, while for a perpendicular polarizer ($\eta_\parallel(\mathbf{r}) = 0$) it acts on the region outside the core [110].

Using the previously-mentioned *surface charge free* ansatz for the in-plane magnetization distribution equation 2.13 simplifies, in the case of a steady circular orbit, to [110]:

$$\mathbf{F}_\parallel^{\mathrm{st}} = \frac{\hbar P p R_c I}{2|e|R^2}(\eta_\parallel(\mathbf{X}) \cdot \hat{\chi})\hat{\chi} \tag{2.14}$$

where $\hat{\chi}$ is a unit vector in the azimuthal direction in physical space (as opposed to spin space) to first order in R_c (and assuming $R_c \ll R_0$, where R_0 is the steady-state orbit radius). Thus, the torque due to the in-plane component of the magnetization depends on the vortex core polarity p. Moreover, equation 2.14 shows that if $\eta_\parallel(\mathbf{r})$ is uniform in space, then this torque component averages out to zero over a full orbit of the vortex core, so only a non-uniform (or time-dependent) in-plane spin-polarization of the current should lead to persistent oscillations of the vortex. Since $\mathbf{F}_\parallel^{\mathrm{st}}$ does not depend on the orbit radius R_0, but $\mathbf{F}^\alpha$ does (through $\dot{\mathbf{X}} = \omega\hat{\mathbf{z}} \times \mathbf{X}$) it is possible to extract R_0 as a function of I and ω for a purely in-plane polarizer by requiring that the net energy change due to the spin-torque and damping forces over a full orbit should be zero in the steady state. The answer depends on the spatial distribution of $\eta_\parallel(\mathbf{r})$ through the integral of the dot product in equation 2.14 over the azimuthal angle (and within this model will be non-zero only for non-uniform spin polarization $\eta_\parallel(\mathbf{r})$).

The calculation of $\mathbf{F}_\perp^{\mathrm{st}}$ based on equation 2.12 is more problematic because

of the assumption implicit in the Thiele approach that translational motion of a soliton (such as a magnetic vortex) follows the expression $\dot{\mathbf{M}} = -(\dot{\mathbf{X}} \cdot \nabla)\mathbf{X}$. This assumption fails near the disk boundary where a large contribution to $\mathbf{F}_\perp^{\text{st}}$ originates. Khvalkovskiy *et al.* have used a generalized version of the Thiele approach[4] to compute this force term, obtaining [111], in the case of a steady circular orbit:

$$\mathbf{F}_\perp^{\text{st}} = \frac{\hbar P \eta_\perp R_0 I}{2|e|R^2}\hat{\chi} \tag{2.15}$$

for the case of a uniform perpendicular polarization $P\eta_\perp$. There are two main differences between $\mathbf{F}_\perp^{\text{st}}$ and $\mathbf{F}_\parallel^{\text{st}}$: i) only $\mathbf{F}_\parallel^{\text{st}}$ depends on the core polarity p, and ii) only $\mathbf{F}_\perp^{\text{st}}$ depends on the steady-state orbit radius R_0. A consequence of the second point is that for the case of a purely perpendicular polarizer, R_0 and I_{c1} (the critical current for exciting steady-state oscillations) can only be computed by including higher-order in R_0/R terms of D and ω_G. (The orbit radius as computed in ref. [96] has a fairly complicated form, but depends as the square-root of the overcriticality $(I - I_{c1})/I_{c1}$.)

Full equation of motion for spin-torque driven vortex precession

Given the terms that were introduced so far, I can write down a more explicit[5] form for the equation of motion for the vortex in the steady-state in the presence of spin-torque, based on the Thiele formalism:

$$G\hat{\mathbf{z}} \times \dot{\mathbf{X}} - \kappa(I)\mathbf{X} + D\dot{\mathbf{X}} + \mathbf{F}_\perp^{\text{st}}(I) + \mathbf{F}_\parallel^{\text{st}}(I) = 0 \tag{2.16}$$

---

[4]This method also predicts some corrections to D, yielding $D = -\frac{\alpha M_s L}{\gamma_0}\pi\left[ln\left(\frac{R}{2l_{ex}}\right) + \frac{3}{4}\right]$.

[5]The previous calculations of the terms of the equation were valid for zero applied magnetic field. In order to introduce magnetic-field dependence into the equation, it is necessary to account for the variation of the polarizer orientation and the change in the vortex magnetization with applied field. To date, the only published results are for the case of a point-contact to an extend film, where certain simplifying assumptions can be made [109]. the

where $\kappa(I) = \omega_G(I)/G$ is the current-dependent restoring term, which as explained above may actually include a term proportional to R_0^2 (leading in that case to a cubic restoring force, that is a quartic potential energy W).

Current-dependence of the gyrotropic frequency

In the presence of the applied current, the frequency of the oscillations ω_G is modified with respect to ω_G^0 by two current dependent terms, so it takes the form [96]:

$$\omega_G(I) = \omega_G^0 + \omega_G^{Oe}(I) + \omega_G^1(I) \tag{2.17}$$

The second term on the right-hand side of equation 2.17 is due to an additional contribution to the restoring force which is due to the Oersted field of the current, and is approximately given by:

$$\omega_G^{Oe}(I) = \frac{0.54\gamma_0 C}{Rc} I \tag{2.18}$$

where 0.54 is a dimensionless number, c is the speed of light and C is the vortex chirality (direction of curling of the in-plane magnetization), which by convention is +1 if the vortex curls in the same direction as the Oersted field and −1 in the opposite case. The third term of equation 2.17 is a second-order correction in R_0/R to the small-radius vortex precession frequency ω_G^0. It is given by:

$$\omega_G^1(I) = k(I - I_{c1})/I_{c1} \tag{2.19}$$

where k is given by another fairly complicated expression which depends on ω_G^0 and I_{c1} and the nonlinear damping constant D [96].

2.4 Control of the polarity and chirality using spin-torque

In addition to the study of the gyrotropic mode, the control of the polarity and chirality of a vortex by means of STT has also been studied. From the stand-
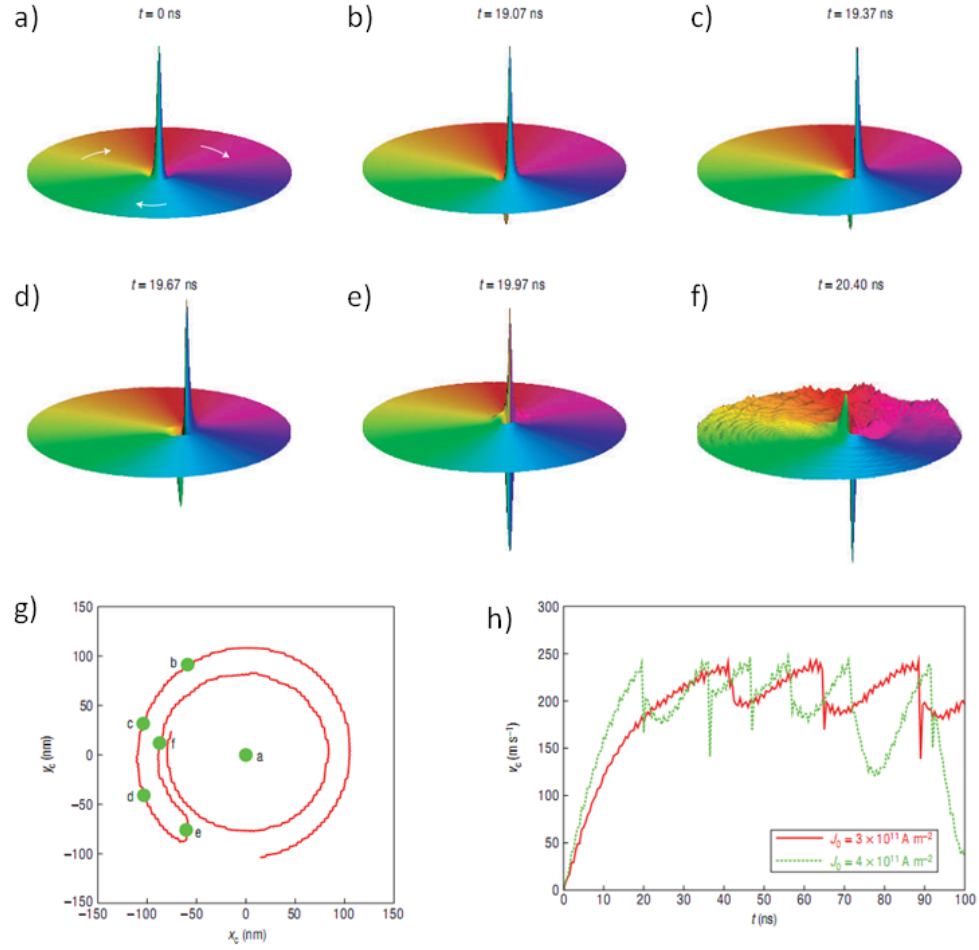
Figure 2.5: Micromagnetic simulations of vortex core switching under resonant ac current excitation in a 50 nm thick single-layer Py disk with a radius of 500 nm. a)-f) Simulations of the magnetization near the core region. g) Simulated trajectory, showing the core positions corresponding to the configurations in a)-f). h) Simulated time trace of the vortex velocity, showing repeated switching event for two different current values. (Modified from [112].)

point of applications this is motivated by the possibility of using each of these two degrees of freedom as a bit of information. The possibility of switching the core polarity in a single-layer Py disk in the CIP geometry was demonstrated by Yamada *et al.* in 2007 [112]. They found that by applying an ac current near the gyrotropic frequency the vortex can be accelerated in a spiral trajectory. As it accelerates, the vortex distorts, leading to the eventual switching of the polarity when the vortex speed becomes about 250 m/s (independent on the current amplitude). The motion is then repeated (with the opposite direction of precession), leading to another switching event (see Fig. 2.5). Since the core polarity switches periodically the maximum switching probability with continuous ac excitation is 50%. Using ac pulses with an amplitude-dependent length should be able to lead to 100% switching probability in principle. However, because the switching involves emission of spin-waves with a chaotic character, there is a large variation in observed switching times, which might make accurate pulse timing difficult. Switching of the core using dc current has been predicted through analytical calculations [113] or micromagnetic simulations [114]. No definite experimental demonstration has been published so far. In the appendix I will briefly describe my experimental efforts to test these predictions, which are still in progress. A scheme for control of the vortex chirality using appropriately-shaped current pulses in a nanopillar has also been proposed (based on micromagnetic simulations) [115].

MAGNETIC VORTEX OSCILLATIONS DRIVEN BY DC SPIN-POLARIZED CURRENT

3.1 Introduction

While it was known that spin-torque switching of a magnetic element can sometimes occur via non-uniform magnetic states [116], a central remaining question at the time I performed these experiments was whether spin-torque can be used to efficiently excite steady-state magnetization oscillations in strongly non-uniform magnetic configurations in a manner suitable for fundamental investigations of nanomagnetic dynamics and improved device performance. A relatively simple type of non-uniform magnetic structure is a magnetic vortex, the lowest-energy configuration of magnetic structures just above the single-domain length scale [82, 117]. Previous studies, typically performed on single-layer permalloy (Py) structures, focused on the transient or resonant response of a magnetic vortex to an applied magnetic field and identified the lowest excitation mode of a vortex as a gyrotropic precession of the core [94, 88, 118, 95]. It has also been demonstrated that the vortex core polarization can be efficiently switched by short radio-frequency magnetic field pulses [119] or by electrical currents [112]. Recently, the spin-transfer effect has been used to drive a magnetic vortex into resonant precession by means of an alternating current incident on a single Py dot [106]. Here I demonstrate by means of direct frequency-domain measurements that a dc spin-polarized current can drive highly coherent gigahertz-frequency steady-state oscillations of the magnetic vortex in a nanoscale magnetic device. The high sensitivity of the technique I used means

that fine changes in the details of the vortex oscillations, such as due to device or material inhomogeneities, can be readily detected.

3.2   Device details
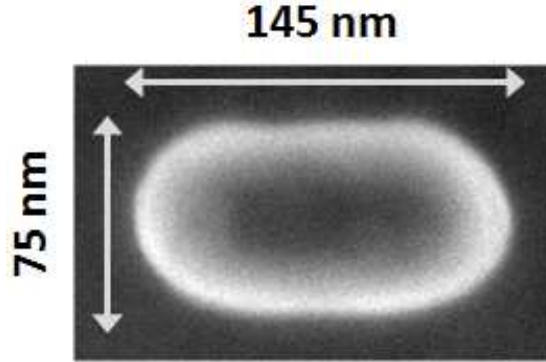
Figure 3.1: SEM image of a vortex nanopillar: top view.

The samples I studied have a spin valve geometry consisting of a thick (60 nm) Py (Py = $Ni_{81}Fe_{19}$) ferromagnetic layer and a thin (5 nm) Py ferromagnetic layer separated by a 40-nm-thick Cu spacer. The thickness of the 60 nm Py layer is chosen to be above the threshold thickness necessary for the nucleation of a magnetic vortex [120]. Electron-beam lithography and ion milling were used to define and etch the spin valves resulting in pillar-shaped devices (Fig. 3.1 and Fig. 3.2d), left inset). The devices used for this experiment had ~160 nm × ~75 nm elliptical cross-sections. The sample is dc current-biased along the pillar axis through Cu electrodes. Relative oscillations of the magnetizations of the two Py layers produce a time-varying voltage via the giant magneto-resistance (GMR) effect. This oscillatory output is then detected using a 30 Hz - 50 GHz spectrum analyzer. The measurements were performed at room temperature

for static magnetic fields applied either perpendicular to the ellipse plane ($H_\perp$) or in-plane, parallel to the ellipse major axis ($H_\parallel$). I observe coherent microwave signals only when electrons flow from the thin Py layer towards the thick Py layer, which is defined as the positive current polarity.

3.3   Experimental observation of steady-state vortex oscillations

Figure 3.2a) shows the dependence of the differential resistance ($\mathrm{d}V/\mathrm{d}I$) of one of the nanopillar devices on $H_\parallel$. The differential resistance curve has the typical features associated with vortex nucleation and annihilation (cf. Fig. 3a) in Ref. [85]). Micromagnetic simulations based on the OOMMF package [121] confirm the existence of a vortex in the thick layer, while the thin layer magnetization is quasi-uniform due to the layer's reduced thickness, which makes the vortex state energetically unfavorable [120]. As $H_\parallel$ increases from zero the differential resistance decreases gradually as the vortex core approaches the device boundary. For $|H_\parallel| >{\sim}650$ Oe the vortex is annihilated and both the thick and the thin layers are in quasi-uniform magnetization states with magnetic moments aligned with the field and the device resistance at its minimum. As $H_\parallel$ is reduced, near ±200 Oe the thin layer moment reorients due to the interlayer dipole field interaction [44], becoming antiparallel to the thick layer moment. The additional switching near $H_\parallel = \pm100$ Oe corresponds to vortex nucleation, which reduces the GMR from its maximum value in the uniform, antiparallel configuration. Discrete steps in $\mathrm{d}V/\mathrm{d}I$ are observed for both out-of-plane (not shown) and in-plane applied fields, resulting from intermittent pinning of vortex due to material defects and device shape imperfections [122, 123]. Due to the thermally activated nature of the vortex nucleation, in some scans, such as the
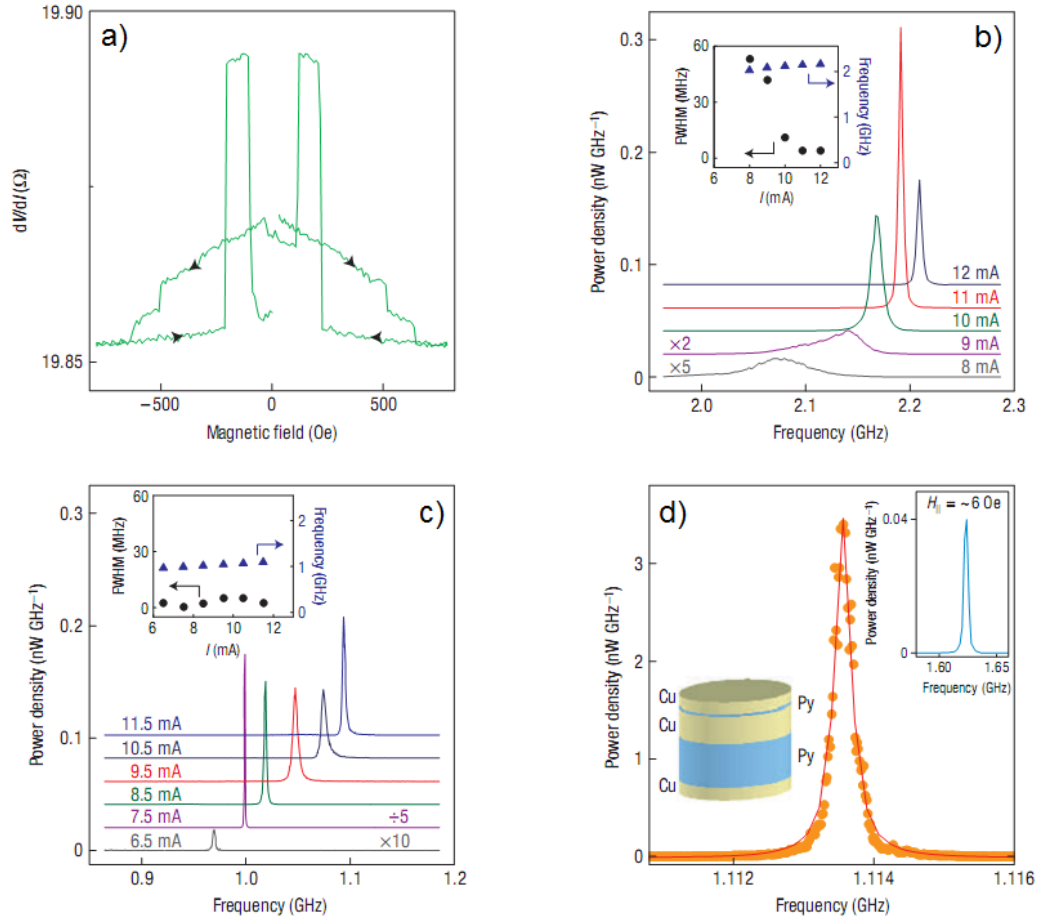
Figure 3.2: GMR and microwave data for sample 1. **a,** Differential resistance for $I = 0$ as a function of $H_\parallel$. The included lead resistance in (a) and (b) is ~12 Ω. The black arrows indicate the field scanning direction. **b,** Microwave spectra as a function of dc current bias for $H_\perp = 1600$ Oe. *FWHM* (circles) and f (triangles) as a function of I (inset). **c,** Microwave spectra as a function of dc current bias for $H_\parallel = 540$ Oe. *FWHM* (circles) and f (triangles) as a function of I (inset). The curves in (b) and (c) are offset by 0.02 nW/GHz along the vertical axis for clarity. **d,** Microwave peak with $\Delta f = 2.8 \times 10^2$ kHz and $f/\Delta f = 4.0 \times 10^3$ for $H_\parallel = 480$ Oe and $I = 9.0$ mA. The continuous line is a Lorentzian fit to the data. Sample layout (left inset). Microwave peak for $I = 10$ mA and $H_\parallel \sim 6$ Oe (right inset).

one shown in Fig. 3.2a), the parallel configuration is preferred near $H_\parallel = 0$ when ramping down the field from negative values. A scan performed immediately afterwards indicates that the vortex is nucleated again near 200 Oe.

To study the spin-torque excitation of vortex oscillations the dc bias current I was varied while keeping H, either $H_\parallel$ or $H_\perp$ fixed. Previous works on vortex-free spin valves have established a link between persistent spin-torque magnetization dynamics and peaks or dips in dV/dI vs. I scans (e.g. Ref. [124] and Ref. [44]). I do observe such features, but they have a relatively small amplitude, which is consistent with the relatively small amplitude of the vortex oscillations. Therefore the signatures of vortex oscillations in the I-V's are not as compelling as they are in vortex-free spin valve nanopillar devices. Consequently, I focused on frequency-domain measurements to establish the existence and study the character (e.g. linewidth, amplitude, and frequency) of these vortex oscillations. As expected, microwave dynamics are observed only for values of $H_\parallel$ between the positive and negative vortex annihilation fields. Figure 3.2b) shows typical frequency-domain measurements of the GMR signal for $H_\perp = 1600$ Oe, as a function of I for sample 1, measurements that are indicative of the excitation of a single strong mode of persistent high-frequency magnetization dynamics in the structure. While I usually observe only one dominant microwave mode under the H and I conditions of interest here, depending upon the bias and sample I sometimes find multiple modes. In general, the power in the second harmonic signal is less than 10% of that in the fundamental, consistent with a nearly sinusoidal oscillation in the time domain.

3.4   Observation of narrow linewidths

The linewidth typically ranges between 60 MHz and <0.3 MHz as the field and current bias conditions are varied. For sample 1, as I is increased for $H_\perp$ =1600 Oe, the full width at half-maximum (Δf) decreases, while the power density increases rapidly, reaching a maximum at I = 11 mA (Fig. 3.2b)). The oscillation frequency (f) increases nearly linearly with I (Fig. 3.2b), inset) at a rate of ~30 MHz/mA. Figure 3.2c) shows the current dependence of the microwave oscillations for the same sample but for a lower field, $H_\parallel$ = 540 Oe. Both Δf and the power density show less variation with I than for the $H_\perp$ case, but the frequency f again exhibits an approximately linear dependence on I (Fig. 3.2c), inset) with a similar rate of change of ~25 MHz/mA.For both in-plane and out-of-plane fields, the oscillations are characterized by $f/\Delta f$ factors that can be $> 10^3$. Figure 3.2d) shows a high-resolution plot of a peak with Δf = 2.8 x 10^2 kHz and $f/\Delta f$ = 4.0 x 10^3, observed for $H_\parallel$ = 480 Oe and I = 9.0 mA. The largest $f/\Delta f$ factors previously observed in a spin-torque oscillator, on the order of 10^4 at ~34 GHz, were obtained in applied magnetic fields that were one order of magnitude larger than for the data in Fig. 3.2d) [71]. As might be expected from a vortex system, I have observed coherent oscillations ($f/\Delta f > 10^2$) for $H_\parallel$ as small as ~6 Oe (Fig. 3.2d), right inset). This demonstrated the possibility to obtain steady-state oscillations of the magnetization in effectively zero applied field. Chapter 4 presents an experiment I performed at zero field over a wide range of current bias.

3.5 Micromagnetic simulations using OOMMF

To gain more in-depth understanding of the vortex oscillations I compared the data to OOMMF micromagnetic simulations of the Landau-Lifshitz-Gilbert (LLG) equation with an additional spin-transfer term[1]. (Details of the simulations are provided in the Methods section at the end of this chapter.) Figure 3.3a) shows the equilibrium configuration of the vortex in the thick ferromagnetic layer for $H_\perp$ =200 Oe, in the absence of spin-torque. The initial magnetic configuration of the thin ferromagnetic layer (not shown) is nearly uniform, with the in-plane component of the magnetic moment pointing in the –x direction.

The simulation indicates that the vortex enters an oscillatory regime (Fig. 3.3b)) in the presence of a spin-polarized current I with positive polarity, with the core precessing in a larger trajectory at the top surface of the thick layer than at the bottom. This motion occurs as a consequence of the transfer of spin-angular-momentum from the incident current to the local moments near the top surface of the thick layer. The resulting torque on the vortex drives it away from its equilibrium position into a trajectory that is further determined by magnetostatic restoring forces [118]. The spin-polarization of the incident current has a spatial distribution that replicates the magnetic structure of the thin ferromagnetic layer, which itself undergoes periodic oscillations from its quasi-uniform, in-plane equilibrium state. These thin layer oscillations have the basic character of periodically flexing the thin layer magnetization into configurations with C-state and S-state-like components, depending upon the details of the simulation conditions, as the vortex precesses. Later in this Chapter, as well as in Chapter 4 I will discuss additional results from experiments and mi-

---

[1]In order to perform these simulations I modified the internal C code of OOMMF to allow for real-time updating of the spin-polarization as a result of the magnetization dynamics.

cromagnetic simulations which indicate that more complex thin layer dynamics are possible, depending on the direction of applied field and current bias.
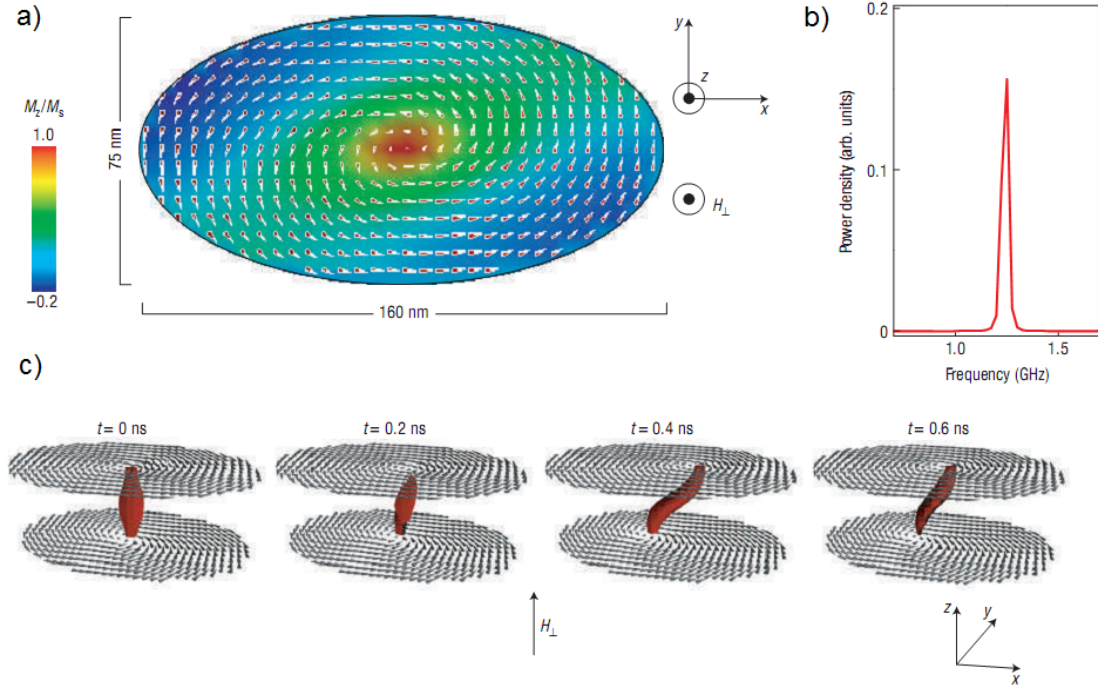
Figure 3.3: Micromagnetic simulation for I =6.6 mA and $H_\perp$ =200 Oe. **a,** Initial magnetic configuration of the thick magnetic layer showing in-plane components (arrows) and z-component (color shading). The cross-section is taken at the top surface of the thick ferromagnetic layer. **b,** Power density spectrum of the y-component of the thick layer magnetization showing a peak at f =1.25 GHz. **c,** Magnetic configuration of the thick layer, showing the in-plane components (arrows) of the layer's upper and lower surfaces and the vortex core (red), at 0.2 ns intervals. The maximum core displacement for these values of I and H is ~20 nm. The magnetization of the thin layer (not shown) is quasi-uniform, with its in-plane components undergoing small-amplitude oscillations from the −x direction, as described in the text.

3.6 Current dependence of the oscillations

The simulations predict an increase in the oscillation frequency with I at a rate of ~30 MHz/mA, consistent with the experimentally observed rate of 20-50 MHz/mA, a result which can be attributed in part to the stronger confinement of the vortex motion due to the increasing Zeeman energy associated with the Oersted field[2]. At the edges of the device, the Oersted field can be as large as ~20 Oe/mA (at the ends of the minor axis) and ~15 Oe/mA (at the ends of the major axis). Thus, the oscillation frequency of the spin-torque vortex dynamics agrees closely with the relaxational eigen-frequency of the gyrotropic core motion in the effective potential due to magnetostatic and Zeeman contributions. The simulations also show that the motion of the vortex is asymmetric about the equilibrium position of the vortex. This symmetry breaking is due to the quasi-uniform spin polarization incident from the thin layer and typically results in an elongated vortex trajectory that is rotated by roughly 45° with respect to the ellipse axes (Fig. 3.3c)). As the vortex follows this elongated trajectory it undergoes periodic distortions from the ideal cylindrically symmetric shape, which in turn cause oscillatory changes in the magneto-resistance of the nanopillar device, the origin of the microwave voltage. Thus, direct comparison with the theory of Ref. [94] cannot be achieved due to the non-ideality of the vortex core and the elliptical shape of our devices. For I greater than ~20 mA, the simulations indicate that the vortex begins to deform significantly due to the large spin-torque, while the GMR signal becomes more chaotic, in agreement with experimental observations on device 1 that the peak broadens and eventually disappears for I greater than ~15 mA.

---

[2]The crucial role played by the Oersted field was also confirmed through detailed analytical calculations of a point-contact device shortly after I published these results [109].

For negative *I* bias the electrons that impinge on the thin layer have acquired a vortex-shaped spin polarization distribution in passing previously through the thick layer. The OOMMF micromagnetic simulations show that the resulting spin-torque acting on the thin layer causes the nucleation of a vortex in this layer. As the magnetization of the thin layer becomes aligned with the spin-polarization the spin-transfer torques on both the thick and thin layers vanish, leading to a stationary steady state, consistent with no coherent microwave oscillations being observed experimentally for negative *I*. When the current is turned off in the simulation, the thin layer magnetization unwinds to the quasi-uniform state due to the shape anisotropy field.

3.7   Dependence on the applied magnetic field direction

The measured vortex oscillation frequency f shows qualitatively different behaviors for $H_\perp$ and $H_\parallel$, with f increasing with H in the first case (Fig. 3.4) and decreasing in the second case (Fig. 3.5), a trend that is reproduced by the simulations. Increasing $H_\perp$ reduces the non-uniformity of the magnetic vortex along the z axis, bringing it closer to an ideal vortex, while the opposite occurs for in-plane applied fields. Thus, I attribute the field-dependence of f to this straightening (deformation) of the vortex for $H_\perp$ ($H_\parallel$) [95]. Uncertainties in the device dimensions introduce a maximum relative uncertainty of ~20% in the values of f obtained from the simulations. While the $H_\perp$ data for sample 2 shown in Fig. 3.4 exhibits a monotonic frequency dependence with a single oscillation mode, the sample 1 data for $H_\parallel$ (Fig. 3.5) includes a series of small discontinuities between roughly linear regions, as well as several regions where two or three peaks coexist in the time-average spectrum. I attribute these jumps in
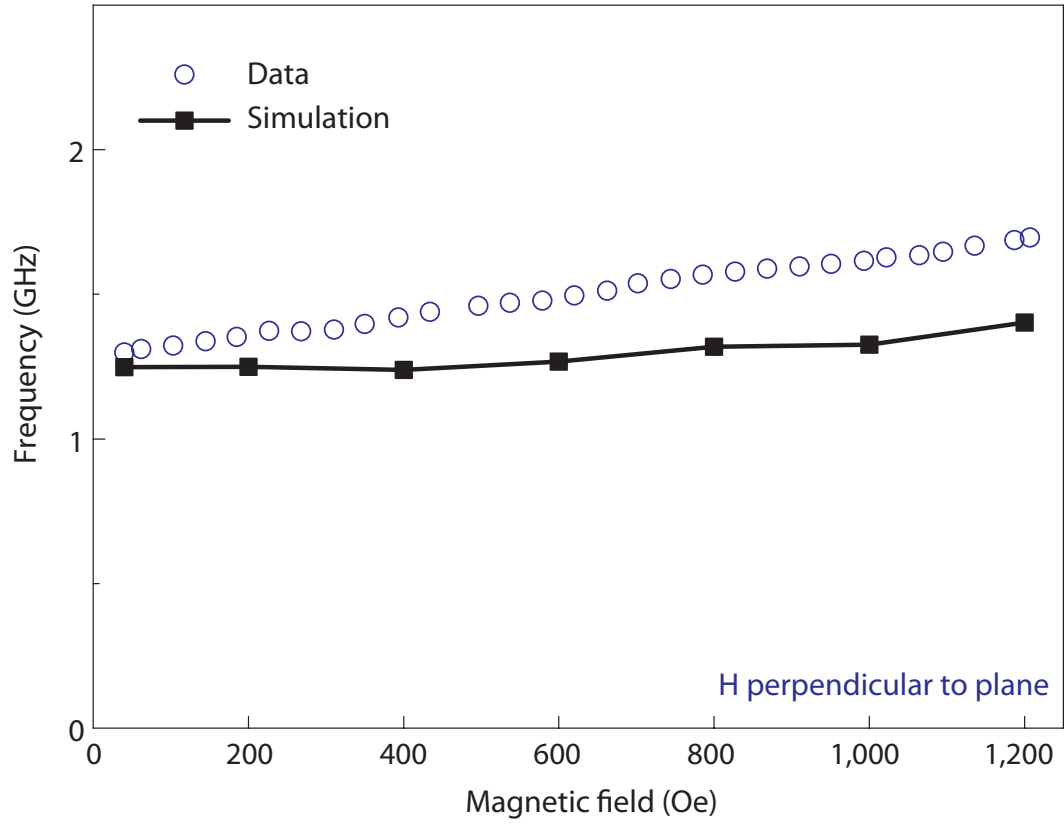
Figure 3.4: Dependence of microwave frequencies on $H_\perp$ for sample 2. The blue dots show the sample 2 data as a function of $H_\perp$ for I =6.6 mA. The black squares indicate the results from micromagnetic simulations on a 160 nm x 75 nm ellipse.

the oscillation frequency to abrupt changes in the details of the vortex's confining magnetostatic potential due to magnetic defects in the thick Py layer, or to abrupt changes in the polarization distribution of the incident spin-torque current due to defects in the thin Py layer. The presence of such defects, which could be intrinsic, or due to shape anomalies or antiferromagnetic surface oxides [125], is confirmed by the existence of irregularities in the GMR field scan (Fig. 3.2a)) near the field values where the f vs. $H_\parallel$ data show discontinuities. As a result of these defects, in certain bias regimes the vortex can undergo jumps between slightly different, metastable trajectories, corresponding to transitions between local minima of the confining potential. Evidence for such metastable trajectories can be seen in the lower inset in Fig. 3.5 where for $H_\parallel$ = 350 Oe, three distinct microwave peaks, with approximately 60 MHz separations, are observed in the time-averaged spectrum. The sampling rate for the data in Fig. 3.5 is 5 MHz/sec, corresponding to a sampling time of ~38 seconds for the data in the lower inset. Using the arguments from reference [67], if I assume that the linewidths of these peaks are entirely due to jumping between the metastable trajectories[3], I calculate that the dwell times for these trajectories range between ~29 and ~159 ns, based on the observed linewidths, which range between ~11 and ~2 MHz, respectively. In studies of the transient oscillation of single vortices in micrometer scale Py disks, the vortex gyrotropic frequency has been observed to fluctuate by a factor of three or more as changes in the dc field move the vortex equilibrium position between pinning sites as little as 10 nm apart [126]. Here I am observing finer changes in the average frequency of persistent vortex motion due to what must be only small changes in the confining potential when averaged over a trajectory that, according to the simulations,

---

[3]In Chapter 4 I will present direct evidence of mode jumping at zero field, where I have observed a maximum of two distinct modes, which are related not to defects, but to changes in the magnetic configuration.

displaces the core ~ 20 nm or more from its equilibrium position.
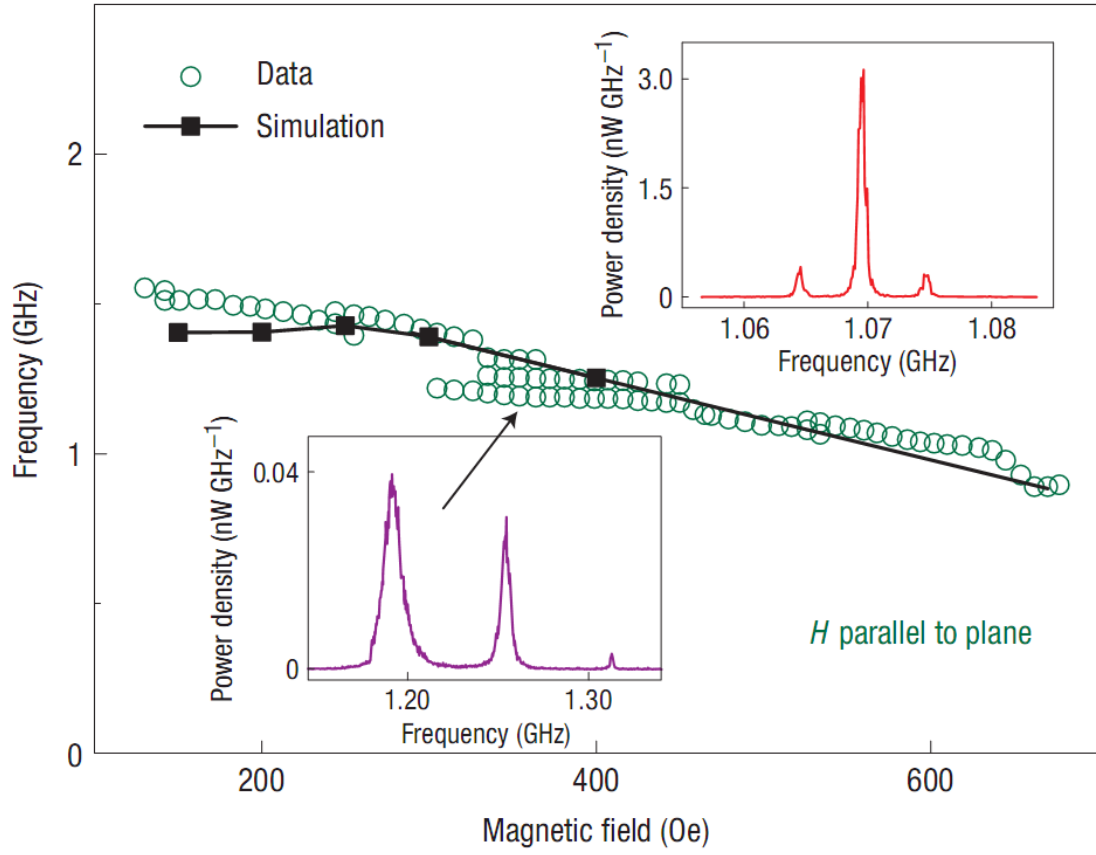
Figure 3.5: Dependence of microwave frequencies on $H_\parallel$ for sample 1. The green dots show the sample 1 data as a function of $H_\parallel$ for I =12 mA. The black squares indicate results from simulations on a 160 nm x 75 nm ellipse. Power density plot for $H_\parallel$ = 350 Oe (lower inset). Demonstration of frequency modulation of a microwave peak, showing first-order side-bands (upper inset). The dc applied magnetic field is $H_\parallel$ =550 Oe and the dc current is I =9 mA. The frequency modulation is induced by an oscillating magnetic field H_{FM} with a frequency f_{FM} =5 MHz, applied along the minor axis of the ellipse.

3.8 Discussion of the oscillation linewidths

The spin-torque-driven vortex oscillations can exhibit significantly narrower linewidths than spin-transfer oscillations in vortex-free magnetic nanopillar spin valves whose minimum linewidths vary between ~550 MHz (at $f \sim 6.5$ GHz) [45] and ~10 MHz (at $f \sim 9.2$ GHz) [127] at room temperature. Since random noise is one of the main sources of linewidth broadening in a self-oscillator [66, 128] one possible reason for this difference is the larger magnetic volume[4] involved in the vortex oscillation and the relatively weak dependence of the oscillation frequency on magnetic field. I argue that the relevant vortex oscillation volume is the entire thick layer, since all spins in the layer are coupled through exchange and magnetostatic interactions. This layer has a considerably larger volume than the oscillating layer in the vortex-free nanopillar experiments. The larger volume reduces the amplitude of the random Langevin magnetic field associated with the thermal fluctuations, while the weak field dependence reduces the effect of this fluctuation field on the oscillation linewidth [67]. Conversely, the narrow linewidth results in this vortex oscillator being a sensitive indicator of magnetic defects in the nanostructure. If some of the magnetic defects that contribute to the non-ideal confining potential are sufficiently uncoupled to the rest of the magnetic system that they thermally fluctuate in a quasi-independent manner, they will collectively modulate the precessional frequency and broaden the oscillator linewidth. As the field and current bias conditions change, the vortex core samples different regions of the nanoscale device, and hence different defect ensembles. Improvements in materials and device fabrication should reduce these variations with bias and further narrow

---

[4]As discussed in Chapter 1 the very shape of the vortex might itself be an important factor affecting the linewidth, but it is still not well understood to what extent this might be the case.

the oscillator linewidth beyond what we have demonstrated here in this initial experiment. Nevertheless, the oscillator is already sufficiently robust that relatively low frequency electromagnetic signals can be coherently detected, as demonstrated in the upper inset of Fig. 3.5, which shows the mixing response to an external 5 MHz magnetic field H_{FM} applied in plane.

3.9 Vortex dynamics under out-of-plane magnetic fields

In the case of applied fields perpendicular to the plane, Giovanni Finocchio and I have later performed additional studies, based largely on micromagnetic simulations. For this, we did not use OOMMF. Instead we used a different code, developed by him and his collaborators, which he adapted (similar to my previous work on OOMMF) to allow simulation of adaptive spin-polarization and torque on both layers, as described in detail below. Unlike OOMMF, this code also allows for the modeling of certain finite temperature effects.

3.9.1 Micromagnetic model for simulations done with a code different from OOMMF

For this micromagnetic modeling study we used a device geometry similar to that in Ref. [61] (Py (5nm)/Cu (40nm)/Py (60nm) of elliptical cross sectional area (160nm×75nm)). The dynamics were simulated by solving the Landau-Lifshitz-Gilbert-Slonczewski (LLGS) equation [129, 130] with the magnetostatic field being computed self-consistently for the entire spin-valve. The spin transfer torque effect in the thinner Py-layer is simulated according to the following

equation:

$$T(\mathbf{m}_p, \mathbf{m}_f) = \frac{g \; |\mu_B| \; j\varepsilon(\mathbf{m}_f, \mathbf{m}_p)}{e\gamma_0 \; M_S^2 L_F} \Big(\mathbf{m}_f \times (\mathbf{m}_f \times \mathbf{m}_p) - \alpha \mathbf{m}_f \times \mathbf{m}_p\Big) \qquad (3.1)$$

where g is the gyromagnetic splitting factor, γ_0 is the gyromagnetic ratio, μ_B is the Bohr magneton, j is the current density assumed to be spatially uniform over the entire device, L_F and M_S are the thickness and the saturation magnetization for the thinner Py-layer, e is the electron charge. Here $\mathbf{m}_f$ and $\mathbf{m}_p$ are respectively, the magnetization of the thinner Py-layer and of the top layer of the thicker Py-layer, where the latter is used as the polarizer layer for the spin-torque computation (the cell used for the discretization is $5 \times 5 \times 5$ nm^3). $\varepsilon(\mathbf{m}_f, \mathbf{m}_p) = 0.5P(\chi + 1)/\big(2 + \chi(1 - \mathbf{m}_p \bullet \mathbf{m}_f)\big)$ is the polarization function which characterizes the angular dependence of the spin torque term, P is the current spin-polarization factor and χ is the giant-magneto-resistance asymmetry parameter. We compute the torques individually for each discretization cell, assuming ballistic transport.

The spin transfer torque effect in the thicker Py layer is simulated according to:

$$T(\mathbf{m}_p, \mathbf{m}_f) = -\frac{g \; |\mu_B| \; j\varepsilon(\mathbf{m}_p, \mathbf{m}_f)}{e\gamma_0 M_{SP}^2 L_P} \Big(\mathbf{m}_p \times (\mathbf{m}_p \times \mathbf{m}_f) - \alpha \mathbf{m}_f \times \mathbf{m}_p\Big) \qquad (3.2)$$

where $\varepsilon(\mathbf{m}_p, \mathbf{m}_f) = \varepsilon(\mathbf{m}_f, \mathbf{m}_p)$, where $\mathbf{m}_f$ is now the polarizer layer, M_{SP} is the saturation magnetization for the thicker Py-layer, L_P is the thickness over which the spin torque effect is exerted in the thicker Py layer and because the spin diffusion length in the Py is ~5 nm [131] we set this to be the thickness of the top discretized layer, i.e. the one closest to the thin Py layer. The magneto-resistance signal is computed over all ballistic channels as $r(\mathbf{m}_p, \mathbf{m}_f) = \frac{1}{N_f} \sum_{i=1}^{N_f} r_i(\mathbf{m}_{i,p}, \mathbf{m}_{i,f})$, where N_f is the number of computational cells of the thinner layer and $r_i(\mathbf{m}_{i,p}, \mathbf{m}_{i,f})$ is the magneto-resistance signal of the ith computational

cell of the thinner layer ($\mathbf{m}_{i,f}$) computed with respect to the ith computational cell of the top discretized layer of the thicker layer ($\mathbf{m}_{i,p}$) by using a cosine angular dependence $r_i(\mathbf{m}_{i,p}, \mathbf{m}_{i,f}) = 0.5\,[1 - \cos(\theta_i)]\,(\cos(\theta_i) = \mathbf{m}_{i,p} \bullet \mathbf{m}_{i,f})$.

For the simulations we employ a Cartesian coordinate system where the x-axis is the easy axis of the ellipse and the y-axis is the hard in-plane axis. By convention, positive current polarity corresponds to electron flow from the thinner to the thicker layer (+z-axis) of the spin valve, and we use: $M_S = M_{SP} = 650$ kA/m, $\chi = 1.5$ and $P = 0.38$, an exchange constant $A = 1.3 \times 10^{-11}$ J/m, and a damping parameter $\alpha = 0.01$. For the static case of no spin-torque current we simulated the magnetic behavior of the spin-valves by solving the Brown equation ($m \times h_{eff} = 0$), with a residual of $\leq 10^{-7}$ considered to be sufficiently low.

3.9.2   Magnetization reversal under perpendicular field

We simulated the magnetic hysteresis loop (Fig. 3.6a) bottom) of the device structure, and qualitatively captured the major features of the giant magneto-resistance behavior as measured experimentally for near zero current bias (Fig. 3.6a) top). In particular, above point A (above applied fields larger than 200 mT) the vortex polarity is +1 (parallel to the field). As the field is swept to negative values, the polarity of the vortex core switches to -1 at point B ($\mu_0 H = -200$ mT). As the field is then swept back to positive values the core polarity switches back to +1 at point A ($\mu_0 H = 200$ mT). At zero field, point C the simulation shows the vortex core located near the center of the ellipse, with a small offset in the hard-in-plane axis due to the magnetostatic coupling
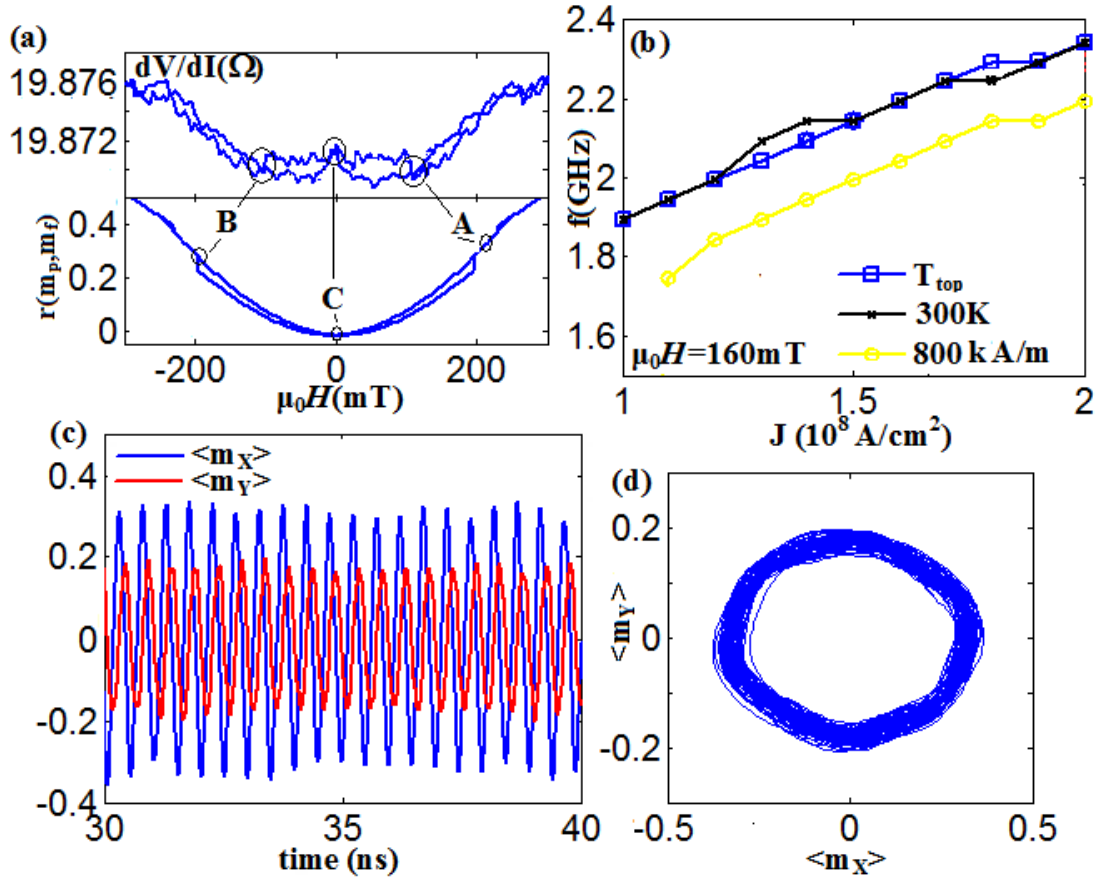
Figure 3.6: Differential resistance and simulated dynamics for a field applied perpendicular to the plane. a) experimental differential resistance (top) and simulated magnetoresistance (bottom) vs. out-of-plane field. b) frequency of the vortex self-oscillation as function of current density ($\mu_0 H$ = 160 mT) for different model parameters. The functional dependence are simulated with the spin transfer exerted on the top section only: T_{top} (T = 0 K, M_{SP} = 650 kA/m), 300 K (T = 300 K, M_{SP} = 650 kA/m), and 800 kA/m (T = 0K, M_{SP} = 800 kA/m). c) Temporal evolution of the x and y component of the average normalized magnetization for J = 1.3 × 10^8 A/cm^2, and d) projection of the trajectory in the $< m_X >$-$< m_Y >$ plane. The simulations in c) and d) are at T = 0 K.

with the thin Py-layer whose magnetization is aligned uniformly along +x or -x direction depending on the magnetic history. In the computation the field is tilted by 1° away from perpendicular direction along the +x direction to control the in-plane magnetization component. The magnetic configuration of the thinner Py-layer remains uniform for each value of field. The major quantitative difference between the simulated magnetic behavior and the experiment is that in the experimental loop, the switching fields of the vortex core polarity are ~ ±150mT, while the simulated values are somewhat larger, ~ ±200 mT. This is most likely because thermal effects were not taken into account in the simulation of the near zero-current, magnetization loop. Possible shape imperfections due to device-to-device variations might also play a role.

3.9.3   Frequency and trajectory of the steady-state oscillations

We systematically studied the behavior of this device structure under the application of a bias current sufficient to excite persistent dynamics, for a range of magnetic fields applied perpendicular to the plane of the thin film layers. In the case of a perpendicular field of 160mT (vortex polarity +1) the simulated vortex dynamics were characterized by a main excited mode with frequency in the range 1.8-2.2 GHz (Fig. 3.6b) T_{top} line). The frequency of this mode exhibits "blue shifting" as function of current, in agreement with experimental observations [61]. The simulated magnetization dynamics have a steady-state character, as can be observed from the temporal evolution of the average normalized magnetization of the thicker Py-layer ($< m_X(t) >$, $< m_Y(t) >$, Fig. 3.6c), $J = 1.3 \times 10^8$ A/cm^2), and the trajectory in the $< m_X >$-$< m_Y >$ plane (Fig. 3.6d)). The vortex core moves in counter-clockwise sense [94] with a quasi-elliptical

trajectory. The experimental "blue shift" functional dependence of the oscillation frequency on the out-of-plane field for a fixed current is also confirmed by our simulations which reveal that the average radius of the vortex trajectory increases with perpendicular field bias (not shown). For example for a current density of $J = 1.0 \times 10^8$ A/cm^2, the average y-component of the magnetization oscillate from -0.08 to 0.08 at 100 mT and from -0.15 to 0.15 at 160 mT[5]. Fig. 3.7a) shows how the vortex positions (trajectories) differ, for the case of $\mu_0 H = 160$ mT, for two different bias current densities, $J = 1.0 \times 10^8$ A/cm^2 ('+') and $J = 2.0 \times 10^8$ A/cm^2 ('o') where we see that the average orbit also increases with current bias. Fig. 3.7b) shows snapshots of the z-component of the magnetization of the top portion of thick layer at two different times during the vortex precessional period. (All results in Fig. 3.7 were obtained for $T = 0$ K.) The trajectories from this simulation of vortex dynamics in a uniform spin valve structure differ from those obtained previously for point-contact geometries in which the vortex moves into and out of the contact region, alternating its polarity and consequently the sense of rotation. [132] Our analysis of the simulation results indicate that the deviations from a pure elliptical trajectory are due to the strong non-uniform configuration in the thinner Py-layer, as shown, for example, in 3.7c) (left and right snapshots). In general, in the case of a significant field perpendicular to the plane, these non-uniform configurations are present even at the minimum current at which the vortex dynamics are excited. In contrast, at zero and near-zero applied field, above the onset current for vortex dynamics the magnetization of the thinner layer oscillates in a quasi-uniform configuration up to the current value that nucleates a second vortex in the thin layer and the GMR-signal then becomes the result of the relative motion of the two vortex

---

[5]We also see that the radius of oscillation increases from $\sim 10 - 15$ nm at zero external field to ~ 30 nm at 160 mT

cores (not shown). [133]
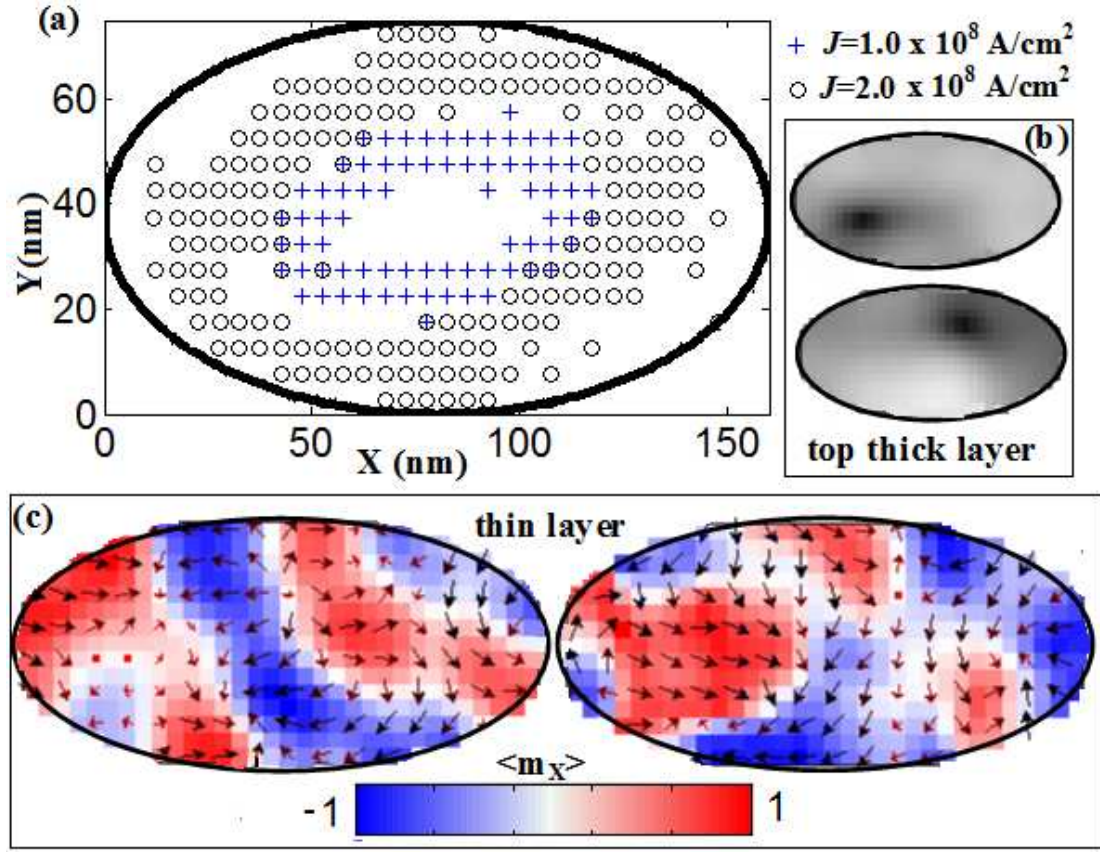
Figure 3.7: Micromagnetic details of vortex oscillations for a field applied perpendicular to the plane and $T = 0$ K. a) spatial positions of the vortex core during its dynamics for two values of current densities $J = 1.0 \times 10^8$ A/cm² ('+') and $J = 2.0 \times 10^8$ A/cm² ('o'). b) two snapshots of the vortex core position (the grayscale represents the amplitude of the z-component of the magnetization). c) corresponding snapshots of the thinner Py-layer magnetization during the vortex dynamics in the thicker Py-layer. The arrows indicate the in-plane magnetization direction.

3.9.4   Effect of varying the parameters

We studied the effect of several model parameters on the frequency of the vortex precession mode. We found no significant change in the dynamics if the torque is distributed across the whole thicker Py-layer or just to the top discretized section of this layer. As expected for a large magnetic volume system, we also find that including a thermal field [134, 135, 136] (T=300K, Fig. 3.6b) 300K line) does not affect the frequency of the dynamics, as illustrated by the two spectra in Fig. 3.8, which were computed via the micromagnetic spectral mapping technique, [137, 138] for $J = 1.3 \times 10^8$ A/cm^2. We do find a dependence of the frequency on the saturation magnetization of the thicker Py-layer, such that the frequency of the vortex dynamics decreases, and the onset current increases when increasing M_{SP} to 800 kA/m, as shown in Fig. 3.6b). The frequency decrease with increasing saturation magnetization is in qualitative agreement with analytical results in point-contact geometries based on the rigid vortex model published in Ref. [109] for the case of a magnetic field applied perpendicular to the sample plane (see equation 4 in Ref. [109]).

Finally, we compare our numerical frequencies with the experimental dynamical data (Fig. 1(b) of Ref. [61]). We determined the proportionality factor κ between the experimental and the simulated currents using the same scaling procedure employed in Ref. [139], and obtained a quite reasonable value κ=0.65. The inset of Fig. 3.8 shows a comparison between the experimental and computed frequency of the vortex self-oscillation at 300K and as can be observed, there is good agreement. Since the 50 ns simulation length limits the linewidth resolution to ~ 20 MHz the linewidth values computed numerically cannot be compared to the experimental data when the experimental linewidths are less
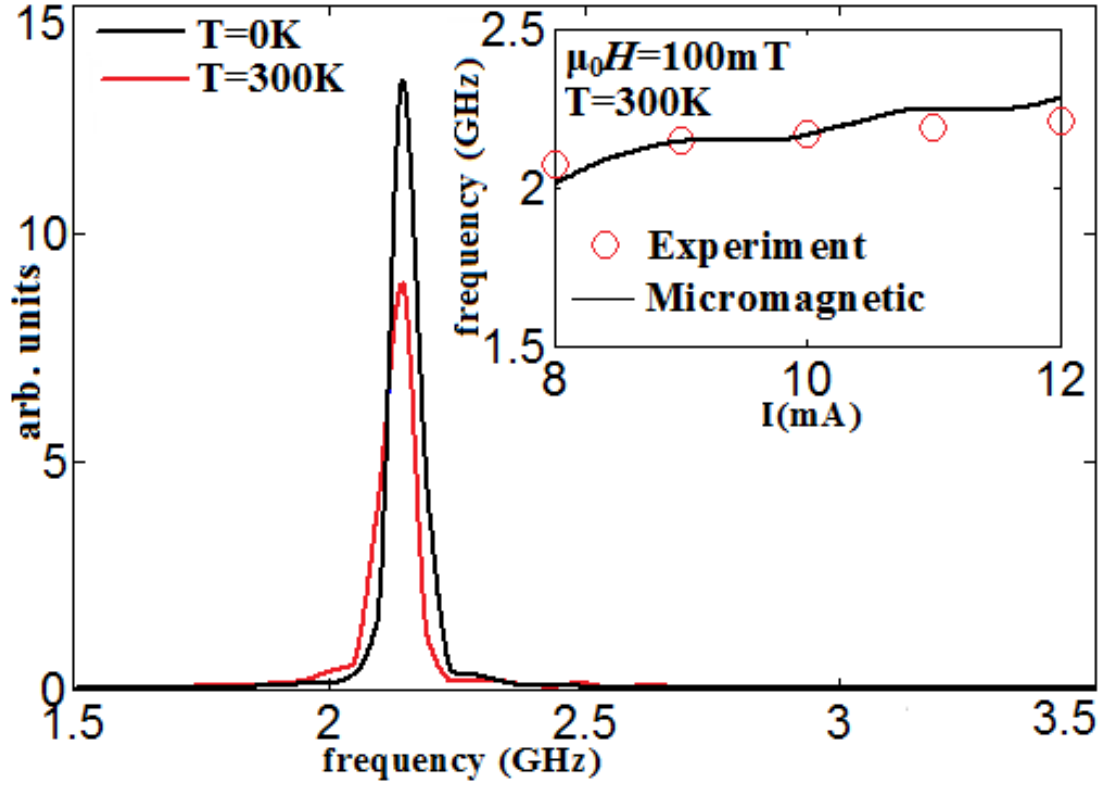
Figure 3.8: Simulated temperature dependence of the vortex oscillation spectra for a field applied perpendicular to the plane. (main panel) spectra of the y-component of the magnetization computed by means of the micromagnetic spectral mapping technique ($J = 1.3 \times 10^8$ A/cm^2) for $T = 0$ K (black line) and $T = 300$ K (blue line). Inset: comparison between numerical and experimental data reported in Figure 1(b) of Ref. [61] ($T = 300$K, $M_S = 650$ kA/m).

than ~ 20 MHz, which is in fact the case for the majority of the data in Ref. [61]. Moreover, the numerical linewidths are computed for the magnetization signal[6], while the experimental values are due to the GMR signal and are therefore expected to differ. However, the simulations do reproduce the expected broadening of the linewidth in the presence of finite temperature effects.

---

[6]The spectra were computed from the y-axis magnetization component averaged across the top discretization layer of the thick ferromagnet.

Thus, the micromagnetic simulations for perpendicular fields reproduce the correct frequency dependence on current amplitude, a "blue shift," and show that: (i) the vortex core moves in the thicker Py-layer in an quasi-elliptical trajectory; (ii) the thinner Py-layer magnetization is in highly non-uniform configuration that changes dynamically as the vortex precesses about its trajectory; and (iii) that the mean radius of vortex orbit increases with the amplitude of an out-of-plane applied field. The results also show that the combined spin-torque and magnetic coupling between the magnetic layers plays a crucial role in the explanation of the features of the magnetoresistance-field hysteresis loop and in obtaining persistent vortex precession. Given the importance of the coupling between the polarizer layer and the layer containing the vortex in determining the existence of the vortex precession it seems reasonable to surmise that the details of the precessional dynamics, e.g. linewidth, also depend critically upon this coupling.

3.10   Conclusions

My direct frequency-domain measurements demonstrate that a dc spin-polarized current can efficiently drive persistent microwave-frequency oscillations of a strongly non-uniform nanomagnetic state. This extends the range of known motions that can be excited by spin-polarized currents and provides a new avenue for studying the properties of magnetic vortices. Compared to the dynamics of uniform nanomagnets, the spin-torque-driven precession of a magnetic vortex exhibits linewidths that can be orders of magnitude narrower. In addition, the sensitivity of the vortex oscillator linewidth and frequency to local magnetic defects in the nanostructure makes it a powerful new nanoscale

probe of magnetic thin film materials. This sensitivity also points to possible device improvements that could lead to even narrower linewidths. The high coherence and the ability to electrically tune the oscillation frequency suggest that this new spin-torque vortex oscillator effect could prove useful for devising nanoscale microwave oscillators and for more complex signal processing. The demonstrated ability to operate such a device in near-zero applied field could lead to easier integration of such an oscillator with current semiconductor technology.

3.11   Methods

3.11.1   Details of the OOMMF micromagnetic simulations

The OOMMF micromagnetic simulations integrate the LLG equation with a spin-torque term of the form described in Ref. [50], using $\Lambda = 2$ for the torque asymmetry parameter. The material parameters are typical for Py: the damping parameter $\alpha = 0.014$, the exchange constant $A = 1.3$ μerg/cm, the saturation magnetization $M_s = 800$ emu/cm^3 for the thick layer, $M_s = 600$ emu/cm^3 for the thin layer (based on SQUID magnetometry measurements) and spin polarization [140] $P = 0.37$. The volume is discretized into 5 x 5 x 2.5 nm^3 elements. The simulation includes the magnetic coupling between the two ferromagnetic layers, as well as the Oersted field due to I. Temperature effects are not taken into account. The spin polarization of electrons transmitted to the second magnetic layer is mapped from the magnetization vector field of the first magnetic layer along the electron flow direction. I treat spins classically and use the simplifying

assumption that the spin component anti-parallel to the local magnetization is fully reflected at the interface between the spacer and the second ferromagnetic layer, thus exerting a torque on the first layer. The micromagnetic simulations provide useful insight into the nature of the spin-torque-driven vortex oscillator, however I emphasize that they may not accurately describe all features of the real system due to simplified modeling of the device geometry and spin-transfer torque, and due to the absence of defects in the simulations. In particular, the linewidths obtained from simulation are limited by the finite simulation time and do not represent the effects of thermal broadening mechanisms. The oscillation amplitude in the simulations typically decays[7], albeit quite slowly, as a function of time, suggesting that our simulations, while fairly closely replicating the frequency of the spin-torque-driven vortex precession, and its field and current dependence, do not capture the full complexity of the spin-torque and magnetic field interlayer couplings. To my knowledge, prior to this result there were no published results on micromagnetic simulations that consider the dynamic coupling between the two ferromagnetic layers in a spin valve with spin-transfer torque. The results suggest this coupling might be of considerable importance in some geometries, such as the vortex oscillator.

---

[7]Some time after the completion of this project I improved the modeling of the reflected electrons. With this modification the simulations based on the OOMMF code show steady-state vortex oscillations that do not decay. The micromagnetic model described in section 3.9.1 also reproduces the steady-state character of the vortex oscillations.

CHAPTER 4

LONG-TIMESCALE FLUCTUATIONS OF ZERO-FIELD OSCILLATIONS

4.1 Introduction

The spin-torque exerted by a spin-polarized current can excite a wide range of magnetization changes in magnetic nanostructures. Of special interest is the excitation of persistent GHz-frequency oscillations by dc currents. This auto-generation phenomenon has increased interest in magnetism-related non-linear phenomena, and is promising for potential on-chip, tunable, dc-driven microwave sources. The majority of studies to date have focused on devices with strong in-plane magnetic anisotropy that oscillate in a quasi-uniform spatial mode under applied field H of 100s to 1000s of Oe. Recently, studies have demonstrated that the spin-torque can also excite persistent GHz oscillations in the absence of any applied magnetic field. [72, 141, 61] Refs. [72] and [61] showed that by making use of the well-known precessional mode [94, 88, 95] of a magnetic vortex in a nanoscale point-contact or nanopillar structure, it is possible to obtain not only zero-field oscillations, but also sub-MHz linewidths, considerably narrower than the 10s to 100s of MHz linewidths typically observed in the conventional vortex-free spin-torque oscillators. Spin-torque-driven vortex self-oscillations have since been observed by other experiments [109, 142], and have been the subject of theoretical studies aimed at better understanding the type of dynamics that can be excited by dc spin polarized currents in nonuniform states [143], as well as the range of applicability for the equations of motion of magnetic vortices. [111] An understanding of the factors affecting the stability of these oscillators and the sources of linewidth broaden-

ing are of great importance for further advances.

I describe time-average and single-shot transport measurements, and comparisons with micromagnetic simulations, that reveal the existence of a mode substructure of the vortex self-oscillations. By simultaneously analyzing the oscillations in the frequency and time domains, we find that the substructure of the oscillations plays a key role in determinnig the average linewidth. The measurements are performed in $H = 0$, as this is perhaps the most technologically important bias regime. The devices studied here are spin-valve nanopillars composed of $Ni_{81}Fe_{19}$(60 nm)/Cu(40 nm)/$Ni_{81}Fe_{19}$(5 nm), with approximately elliptical cross-sections (dimensions for each device are specified below), fabricated as described in Ref. [61]. In equilibrium the thick Py layer has a vortex configuration and the thinner polarizing layer a uniform in-plane magnetization, but as we discuss below an alternative configuration is also possible at high bias currents.

4.2 Frequency-domain measurements

The dependence of the frequency f and linewidth ($FWHM$) on current (I) for one such device (dev. 1, nominal dimensions 80 nm x 180 nm), as measured with a spectrum analyzer, are shown in Fig. 4.1. Although the vortex oscillations are expected to be single-mode, corresponding to the gyrotropic precession of the core, the spectrum actually shows two different modes as a function of bias. The lower frequency mode (M1) and the higher frequency mode (M2) appear to coexist for I between ~6.5 mA and 9.5 mA. The presence of two modes at $H = 0$ is a feature of all devices we studied, although the details of the bias

87
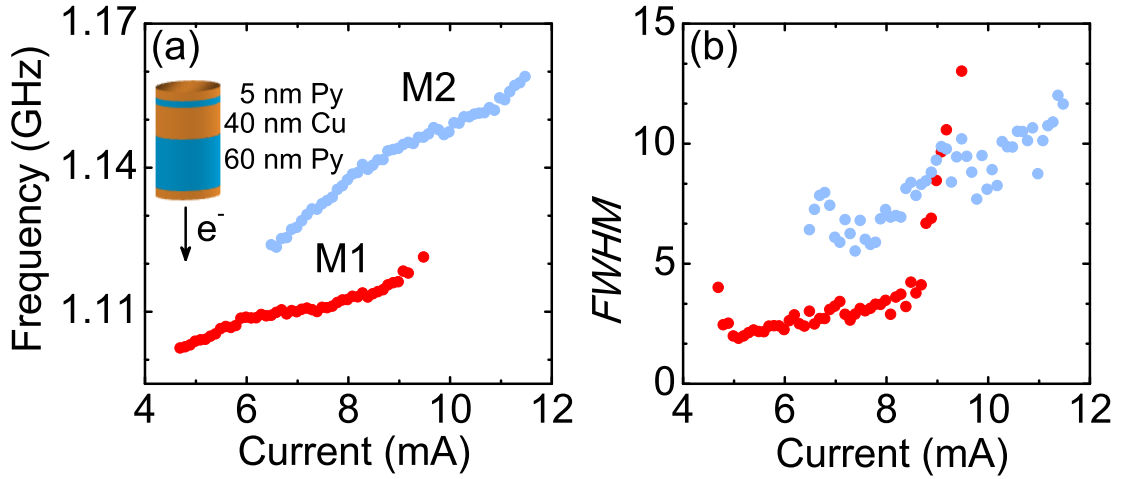
Figure 4.1: Current dependence of (a) frequency and (b) *FWHM* measured on dev. 1. Inset: schematic of device geometry, showing the direction of electron flow under dc bias.

dependence varied from sample to sample. For dev. 1 the two modes have an approximately linear dependence of frequency on current with average slopes of 3.3 MHz/mA for M1 and 6.5 MHz/mA for M2. The linewidths increase at a rate of 0.5 MHz/mA for M1 and ~1.0 MHz/mA for M2, but a stronger dependence is observed for M1 at small and large biases.

4.3   Single-shot (non-averaged) time domain measurements

4.3.1   Data acquisition and processing

To obtain information about time correlations between the two modes, I have performed single-shot time domain measurements[1], with a setup as illustrated

---

[1] I used a Lecroy WaveMaster8500 (5 GHz analog bandwidth) and a Lecroy SDA1100 (11 GHz analog bandwidth) storage oscilloscopes, each at various parts of the experiment.
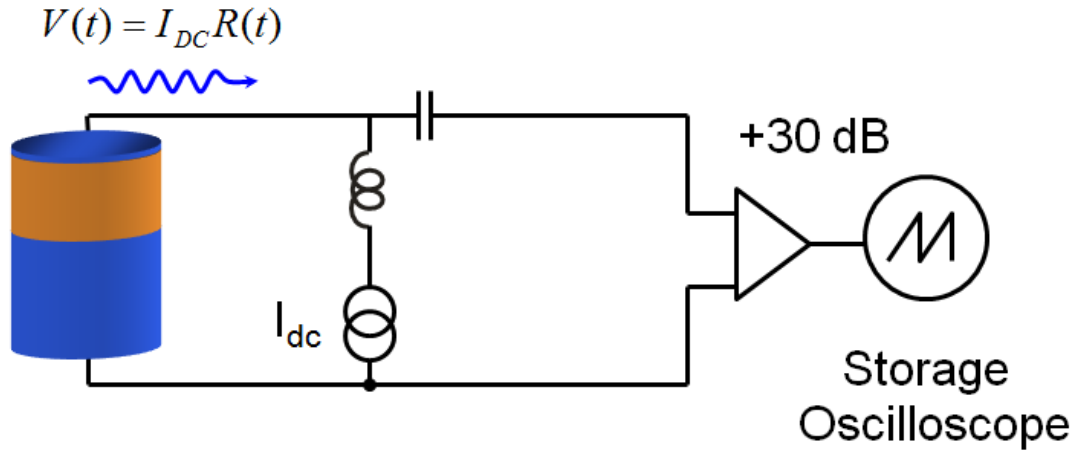
Figure 4.2: Schematic of experimental setup for the single-shot time domain measurements. $R(t)$ is the time-dependent resistance of the device that results from the magnetization dynamics and the GMR effect.

schematically in Fig. 4.2. These measurements consist of capturing the output of the oscillator without performing any time average. While this technique obviously reduces the signal-to-noise ratio of the experiment, it has the major advantage of allowing detection of transient features of the data. By band-pass filtering[2] the time-domain signals I was able to reduce the noise background sufficiently to study the time-dependent output of the devices. The digital filter bandwidth was adjusted for each peak as a function of its width (typical values were ~1.5 to 5 times the average linewidth) and was centered at the peak's main emission frequency. Fig. 4.3 shows such time traces measured using a digital storage oscilloscope with an analog bandwidth of 3 GHz and sampling rate of 20 GS/s.

[2]REU student Ben Williams helped out tremendously with writing the Labview code used to do the data acquisition and analysis!

4.3.2 Long-timescale fluctuations of the thin layer configuration

The time domain measurements reveal that the system has only one major mode of oscillation at a given time but switches randomly between the two possible modes, with bias-dependent dwell times in the μs range. Figure 4.3a) shows, as function of I, the fraction of time the system spends in each of the modes M1 and M2 for dev. 1. To obtain these data we computed the envelope of 100 μs filtered traces such as those shown in Fig. 4.3b) and then determined the fraction of time the envelope was above the combined amplifier and Johnson noise floor. Mode M1 dominates from the onset of dynamics to ~6.0 mA, while M2 dominates for I larger than ~8.8 mA. A transition region is observed at intermediate biases. The frequency shifts I discuss here are similar to the telegraph switching between spin-torque excited dynamic modes previously observed in conventional spin valves [144], but with the distinct difference that the timescales of the fluctuations in the case of the vortex oscillator are between two and three orders of magnitude longer than for the vortex-free spin valves. This indicates that the effective energy barrier retarding transitions between the two modes in the vortex oscillator system is much higher than for mode transitions in the quasi-uniform spin valve system, or alternatively that the attractors that define the two modes in phase space for the vortex oscillator are much stronger than for quasi-uniform spin valves.
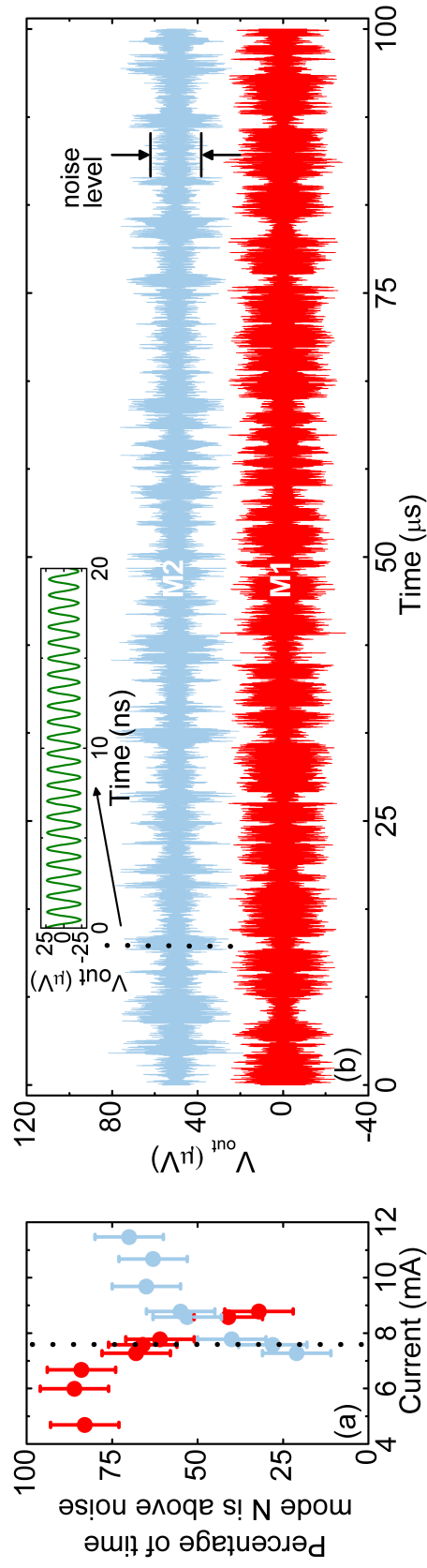
Figure 4.3: (a) Percentage of time spent oscillating above noise floor in modes M1 and M2 as a function of I, for dev. 1, obtained from a 100 μs time trace. (b) Digitally filtered time traces for modes M1 and M2 at 7.6 mA. V_{out} is the voltage delivered to the 50 Ohm line. The time trace for M2 is offset by 50 μV for clarity. Inset: 20 ns subset of trace for M2.

Micromagnetic simulations

To gain insight into the magnetic configurations associated with the experimental observations I used micromagnetic simulations[3] [129, 130] of the entire device, including the spin-torque acting on both magnetic layers and the Oersted field due to the current. I used simulations of two device cross-sections: an ideal ellipse and an additional cross-section (shape A) modeled on a scanning electron microscope image of an actual device. Figure 4.4 shows the current dependence of the frequency and the linewidth extracted from Lorentzian fits to the Fast Fourier Transform (FFT) of the MR oscillations[4] for the two shapes at a temperature (T) of 300 K and H =0. In the simulations, the current was initially set to a value of ~20 mA (ideal ellipse) and ~15 mA (shape A), then stepped down. The duration of the simulations, which was constrained by practical computation time length, limits the minimum linewidth to ~30 MHz. Due to the large initial current values, the devices start in a state with a vortex in the thin polarizing layer, in addition to the stable vortex in the thick layer. The chirality of the thick layer vortex is given by the Oersted field, while that of the thin layer vortex is opposite, due to the spin-torque from the reflected spin polarization. At the initial large bias the dynamics are highly chaotic and the frequency is not well defined. As the current is stepped down the precession of the coupled pairs of vortices becomes regular and the oscillation linewidth narrows. Eventually, between 5.2 mA and 2.5 mA the thin layer configuration switches from a vortex (V) to a quasi-uniform (QU) configuration [Fig. 4.4a) and b)], with details

---

[3]The materials parameters are typical of Permalloy: saturation magnetization M_s=650 e.m.u/cm^3, damping parameter α=0.01, exchange constant A=1.3 μerg/cm and spin polarization P=0.38. 5x5x5 nm^3 cells were used.

[4]The frequency spectrum was computed by summing the absolute values of the FFTs of the MR time traces over all balistic channels. A cosine angular dependence was used to compute the the MR trace for each channel.

depending on the simulated device shape. For the ideal ellipse I also used simulations where the direction of the current ramp was increasing [Fig. 4.4c) and d)]. In this case, the thin layer remains in the QU configuration for I up to a value between ~15.5 mA and 20.6 mA, then switches to a vortex. This reveals the existence of a broad bias range, between ~5 mA and ~16 mA, within which both QU and V configurations of the thin layer are stable over the 100 ns length of all simulations. These two magnetic configurations are shown in Fig. 4.4e) and f). The frequency difference between the two simulated modes, corresponding to the two magnetic configurations of the thin layer, varies with bias between ~30 MHz and ~120 MHz, while the experimental frequency splitting between modes M1 and M2 of device 1 ranges from ~15 MHz to ~27 MHz, with the smaller difference perhaps being due to the non-ideal shape of the experimental device. The simulated linewidth for the V-QU configuration is lower than for the V-V configuration at low currents and increases sharply at larger bias, in qualitative agreement with the experimental observation for dev. 1. The good qualitative agreement of the simulations with the experiment suggests that the lower frequency experimental mode M1 corresponds to the V-QU configuration while M2 corresponds to the V-V configuration, with the data in Fig. 4.3a) indicating that oscillations in the V-QU configuration have the dominant lifetime at low bias and oscillations in the V-V are dominant at large bias. While the time domain measurements show that modes M1 and M2 are metastable, their lifetimes are $\geq 1\ \mu$s, even when the bias is such that these dwell times are comparable. This is more than an order of magnitude longer than the duration of the simulations, which therefore do not capture the reversible jumps between V-V and V-QU seen experimentally.
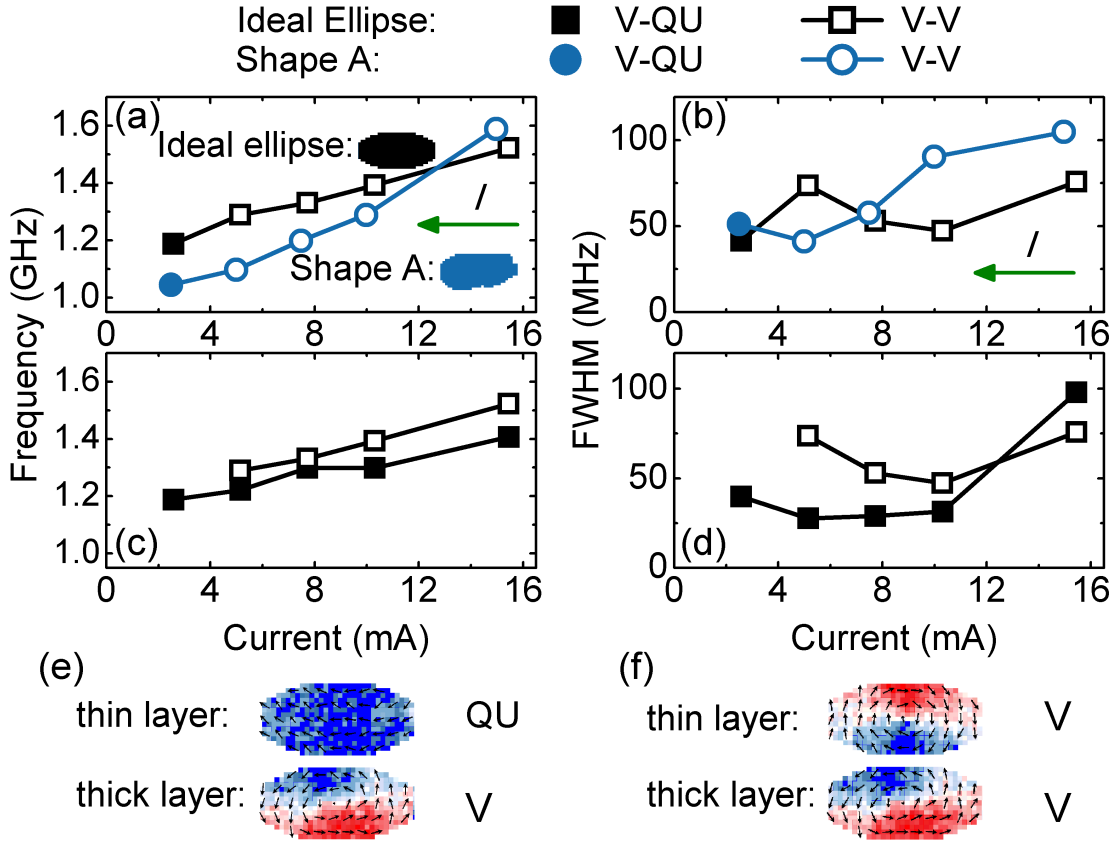
Figure 4.4: Simulated current dependence of (a) frequency and (b) *FWHM*, showing differences between two 75 nm x 160 nm shapes, for decreasing *I*. Current dependence of (c) frequency and (d) *FWHM* for the ideal ellipse, showing difference between the V-QU and V-V configurations. (e) One of the two possible micromagnetic configurations, at 5.2 mA: V-QU. (f) The second possible configuration: V-V. The color scheme in (e) and (f) indicates the direction of the in-plane component of the magnetization and varies from blue to red as the magnetization rotates from left to right.

4.3.3 Long-timescale abrupt frequency fluctuations

Since the dwell times of the two modes as determined by the time domain measurements are generally on the order of 1 μs to 10s of μs, except at the extremes of the bias range for oscillation, mode jumping due to abrupt changes in the overall magnetic configuration of the thin layer is not a dominant contribution to the individual mode linewidths, >1 MHz, obtained from time-averaged frequency measurements. Instead we find by higher resolution time domain studies that each peak exhibits a substructure caused by abrupt small-scale changes in its frequency and amplitude, also with slow characteristic timescales of 100s of ns to μs. Fig. 4.5a) shows the Fourier spectrogram of a 5 GS/s time trace of mode M1 from a second device (dev. 2, 75 nm x 155 nm), obtained by sliding a 4 μs long Hann window [145] across the time trace in 20 ns steps. The spectrogram of a sine wave with similar frequency and integrated power produced with a commercial generator, shown for comparison in Fig. 4.5b), displays a stable frequency with the power clearly concentrated within the resolution bandwidth. In contrast, the device oscillations exhibit fluctuations of the frequency that are abrupt on the μs time scale of the measurement, as well as fluctuations in the shape and width of the spectrogram. These fluctuations qualitatively resemble those recently reported in vortex-free MgO magnetic tunnel junctions (MTJ) [146], however the timescales for our vortex spin-valves are orders of magnitude longer than the ns timescales reported for the vortex-free MTJs, indicating that the vortex oscillations are much more coherent. Moreover, while Ref. [146] reports that discrete amplitude fluctuations dominate at low bias and continuous frequency fluctuations are dominant at high bias for vortex-free MTJs, I find that for vortex spin-valves the fluctuations can have a discrete character across the entire bias range we studied.
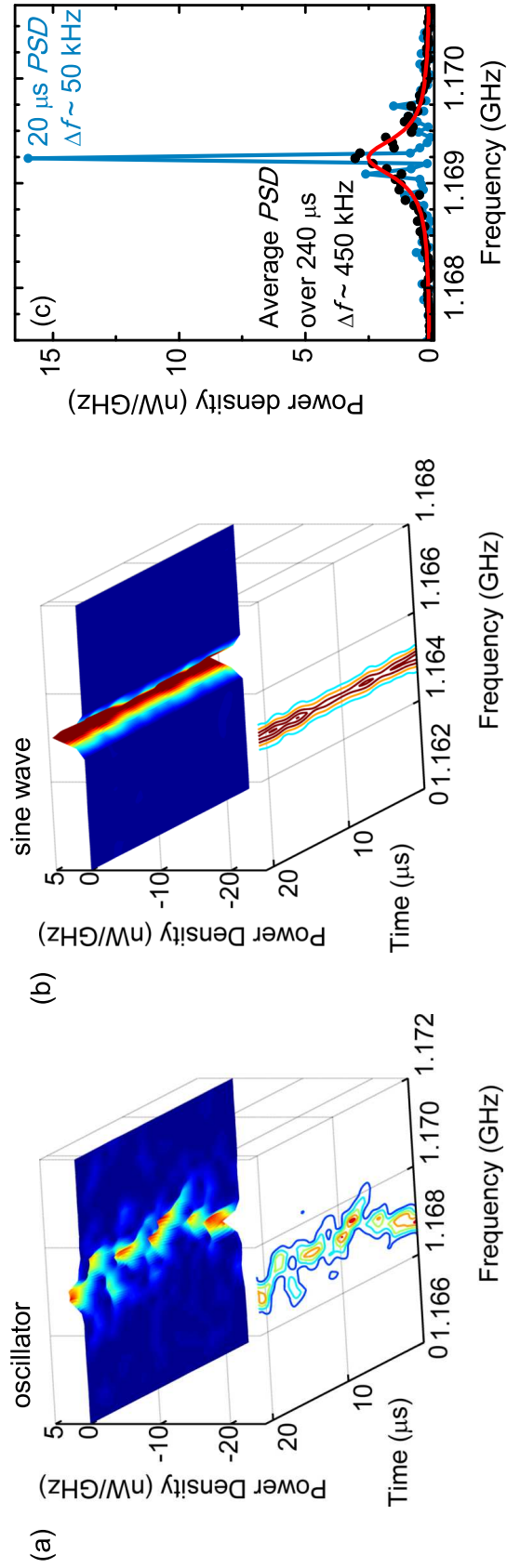
Figure 4.5: Spectrogram of (a) dev. 2 at I =3.8 mA, showing discrete frequency and amplitude fluctuations, and (b) a 1.165 GHz sine wave with similar total power to device in (a), measured with the same circuit. The power fluctuations visible in (b) display the electronic noise added by the measurement circuit. (c) *Average PSD* of a 240 *μs* time trace from dev. 2 (black dots) and corresponding Lorentzian fit (red, lower line) with $\Delta f \sim$450 kHz; *PSD* of a 20 *μs* contiguous subtrace (blue, upper line), with $\Delta f \sim$50 kHz, limited by the length of the rectangular time window.

4.3.4 Linewidth broadening by long-timescale discrete frequency fluctuations

The small, discrete frequency jumps are particularly relevant since they appear to be the dominant contributor to the average linewidth of the vortex oscillator. In the intervals between these jumps the linewidth can be quite narrow. For example, a typical long-time-averaged power spectral density (*PSD*) yields a relatively broad *FWHM* of 450 kHz, while the *PSD* of one of the 20 μs long interval within this longer trace has a *FWHM* equal to the 50 kHz bandwidth set by the measurement window (Fig. 4.5c)). This nine-fold reduction of the linewidth shows that the oscillator can be stable to better than 5×10^{-5} over 10s of μs (more than 10^4 cycles) before an abrupt change alters the center frequency. The corresponding value for the length of stable oscillations in vortex-free MTJs is just 10s of ns. [146] The much slower timescales of the fluctuations for the vortex oscillator are another sign of its greater stability, in addition to its much narrower intrinsic linewidths (50 kHz min.) compared to the vortex-free MTJs (~1 MHz min.), albeit at the lower frequency of the vortex gyrotropic mode.

An analytical model of linewidth broadening in spin-torque oscillators has been proposed [63] based on the effect of Gaussian thermal noise in a nonlinear system, that has been found to be in good agreement with experiment for certain device geometries. [70] Given the characteristics of thermal noise, the bandwidth of the resulting frequency fluctuations is expected to extend up to the ferromagnetic resonance frequencies of the magnetic elements within the device. This does not appear to be compatible with the dominant frequencies of the discrete fluctuations we observe in the vortex oscillator, which are two to three orders of magnitude slower.

I propose, instead, that these discrete, μs-timescale frequency fluctuations result from abrupt changes in the non-ideal vortex orbit. The ability of static magnetic imperfections to affect vortex dynamics has been demonstrated by optical Kerr microscopy studies that have shown that the gyrotropic frequency of a vortex in a micron-scale thin film structure can vary by a factor of three or more when the core is displaced relative to different pinning inhomogeneities. [126] Due to the relatively small region covered by the precessing core, and the stronger confining potential in our nanopillars, I do not expect, nor observe, such large variations in the frequency. However, if the confining potential for the vortex is not ideal, then abrupt changes in the orbit can occur if, on the same time scale, there are either abrupt changes in the magnetic configuration that defines that potential, which could be due to thermal or spin-torque excitations, or if there are chaotic transitions between different attractors in the non-ideal phase space. [68] According to the simulations, which assume a magnetically perfect, albeit digitally modeled system, the vortex oscillator can indeed be chaotic, even at T=0, due in part to the spin-torque excitation of localized magnetic dynamics. Although direct comparison with experiment is impossible due to the short simulation times, the fact that at sufficiently high bias, both in the experiment and in the simulations, the vortex oscillator linewidth broadens and the device behavior becomes chaotic, with the oscillation eventually breaking down, suggests that spin-torque excitation of localized magnetic dynamics could be a significant contribution to the smaller-scale linewidth broadening observed by the time domain measurements at moderate bias levels.

4.4 Summary of relevant timescales

Since this chapter contains a number of important time scales, I am listing them below, in Table 4.1, for easier comparison with each other.

Table 4.1: Relevant timescales for the time-domain measurements, in nanoseconds. (Note that at very low bias mode M2 is not detectable, while at very large bias M1 is not detectable.)

Typical oscillation period	~ 0.9
Length of micromagnetic simulations	10^2
Average time between fluctuations that lead to linewidth broadening	$\sim 10^2$ to $\sim 10^3$
Average dwell time in the V-V or V-QU configurations	$\sim 10^3$ to $<\sim 10^5$

4.5 Conclusions

In conclusion, the results presented above show that zero-field, spin-torque driven vortex self-oscillations are characterized by very long timescale fluctuations (100s of ns to 10s of μs). By means of single-shot time-domain measurements I can resolve two main types of fluctuations. The first are due to transitions of the thin polarizing magnetic layer between quasi-uniform and vortex configurations, resulting in shifts of 10s of MHz in the ~1 GHz vortex gyrotropic frequency. The second are smaller fluctuations that appear to be the

dominant contribution to the long-time average linewidth of the vortex oscillator. The discrete, low-frequency character of these smaller fluctuations suggests the dominant linewidth broadening mechanisms are either dynamic changes in the magnetic configuration that defines the vortex orbit, or chaotic transitions between attractors in the phase space established by the device shape and defect configuration. A stronger confining potential would reduce the sensitivity of the orbit to magnetic defects and hence could better stabilize it. The use of smaller devices and more homogeneous thin films could therefore yield significant improvements in vortex oscillator properties.

CHAPTER 5

SPACE AND TIME-RESOLVED X-RAY IMAGING OF THE VORTEX DYNAMICS

This chapter discusses results obtained from studies performed at the Advanced Light Source (ALS) soft x-ray synchrotron source (part of the Lawrence Berkeley Laboratory), and at Cornell University. For this project I worked in close collaboration with Yves Acremann (then staff scientist at the Stanford Synchrotron Radiation Lightsource (SSRL)) and Xiaowei Yu (then a PhD student in the Stöhr group at Stanford), as well a number of other collaborators at Cornell, SSRL and the ALS. I was involved in the project at all stages: i) sample fabrication, which I performed at Cornell (the process included a number of challenges, the solutions to which I will describe in more detail in the Appendix of this dissertation), ii) sample characterization (performed in part by myself at Cornell and in part by me with some of the SSRL/Stanford collaborators in California), iii) data acquisition, for which I traveled to Berkeley for the majority of "beamtimes," iv) discussions and analysis of the data, and v) writing of the manuscript.

The results of this study constitute direct experimental proof of the presence of the vortex magnetization configuration in the spin-valve nanopillars discussed in the previous two chapters, which was previously inferred from key signatures associated with the transport measurements, and from micromagnetic simulations. The study also uncovered important implications of the small size of spin-transfer devices on magnetization configurations. Before I describe the study in more detail, I would first like to provide some background on various magnetic imaging techniques, focusing particularly on the X-ray Magnetic Circular Dichroism (XMCD) effect, which we used in this experiment.

5.1 Overview of magnetic imaging

A number of techniques exist for imaging the magnetization of micro- and nano-scale devices. Some of the most commonly-used are:

1. Magneto-optical Kerr microscopy (MOKE) (or Faraday microscopy, if in transmission mode) relies on the rotation of the plane of polarization of linearly-polarized light by the magnetization of the sample. Kerr microscopy has been used extensively for the early experimental studies of the vortex gyrotropic mode in single-layer micron-size disks, because it is relatively easy to set up and run. However, it is limited to the film surface, it is not element specific and has low resolution (limited by the wavelength of light). It is therefore not an option for imaging complex, multilayered, nanoscale samples, such as spin-torque nanopillars.

2. Magnetic force microscopy (MFM) measures the magnetic contribution to the force acting on a small tip scanned near the surface. It is limited in resolution to ~30-50 nm, and can be difficult to interpret, but is relatively inexpensive. One of the drawbacks is that stray field from the tip can affect the magnetization of the sample that is being imaged.

3. Spin-polarized scanning tunneling microscopy (SP-STM) is an extension of conventional STM using a tip coated with a thin ferromagnetic layer, or an antiferromagnetic tip. Just as for MFM, one must be able to distinguish between the effect of the topological features and the magnetic features. The technique can provide atomic resolution of a metallic surface, but is very challenging.

4. Lorentz microscopy relies on the deflection of the electron beam of a trans-

mission electron microscope due to the magnetic field of the sample. The technique can achieve similar resolution to a TEM, but requires expensive equipment. Some restrictions are imposed on high magnification imaging by the need to avoid stray magnetic fields from the magnetic lenses.

5. Photoemission electron microscopy (PEEM) measures the emission of secondary electrons ejected by x-rays incident on the sample. The emission of secondary electrons is proportional to the absorption cross-section for the x-rays [147]. Spatially-resolved magnetic information can then be obtained by making this cross-section magnetization-dependent. This can be achieved using dichroism effects (see for example a description of x-ray magnetic circular dichroism, below). For magnetic imaging, one needs intense x-rays from a synchrotron. PEEM has a resolution of 15-50 nm (e.g. PEEM-2 at the Advanced Light Source), but is only a surface technique (2-5 nm depth), since secondary electrons are only ejected outside the sample from this small shell.

5.1.1   X-ray Magnetic Circular Dichroism

The X-ray Magnetic Circular Dichroism (XMCD) effect refers to the different absorption experienced by the two different X-ray circular polarizations depending on the relative orientation of the photon helicity and the local magnetic moment, as illustrated in Fig. 5.1. The effect was first demonstrated in 1987 by Schütz and coworkers [148]. Since then it has been used for a variety of microscopy and spectroscopy studies (e.g. [149, 150]). Over the last few years, several groups have used the effect to study time-resolved magnetization dynamics in metallic microstructures (e.g. [119]) or nanostructures (e.g. [151]). It

is a very powerful, but quite challenging and time-intensive technique. Among its key advantages over some of the other magnetic imaging techniques mentioned above are: i) possibility of high (< 100 ps) temporal resolution, ii) high spatial (< 40 nm) resolution, iii) does not affect the magnetization (such as, for example, Magnetic Force Microscopy does), iv) can be used to separate spin and orbital contributions, and most importantly for the case of complex nanostructures v) it can be used to investigate multilayer devices, since it is a "bulk," material-specific effect.
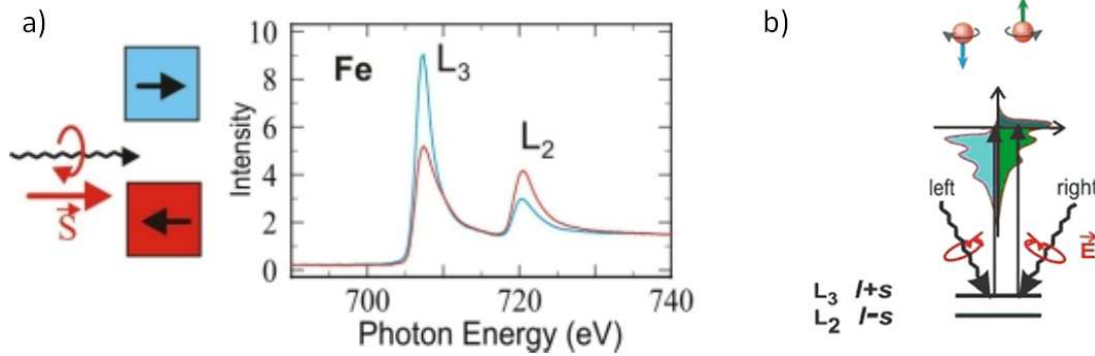
Figure 5.1: Schematic illustration of the X-ray Magnetic Circular Dichroism effect. For $3d$ ferromagnets, where the magnetization is due primarily to the electronic spin, the $2p - 3d$ (L-edge) transitions are typically most relevant. a) Due to spin-orbit coupling the $2p$ orbital degeneracy is lifted, leading to a splitting of the L edge into the L_2 ($2p_{1/2} \rightarrow 3d$) and L_3 ($2p_{3/2} \rightarrow 3d$) edges. Reversing the magnetization (or equivalently the x-ray polarization) results in different absorption. The sign of this dichroism is opposite for the L_2 and L_3 edges, as a result of the opposite sign of spin-orbit coupling. b) Illustration of the spin transitions. Modified from Ref. [152]

XMCD effect in $3d$ **ferromagnets**

Since the magnetic properties of $3d$ ferromagnets are primarily determined by the spin of $3d$ valence electrons, the XMCD effect is going to be strongest for transitions that involve these electrons. Since absorption of a photon corresponds to a change of the total angular momentum by $\pm\hbar$, a convenient transition occurs between $2p$ and $3d$ orbitals (L-edge), as illustrated in Fig. 5.1. In fact, spin-orbit coupling splits the $2p$ level, leading to a splitting of the L edge into the L_2 ($2p_{1/2} \rightarrow 3d$) and L_3 ($2p_{3/2} \rightarrow 3d$) edges. In $3d$ metals both L-edges have energies slightly less than 1 keV, which is in the soft X-ray band. At this energy scale, these are dipole electronic transitions and consequently obey the selection rules given in Table 5.1. With this in mind, a qualitative explanation

Table 5.1: Dipole selection rules, where l, m, s and m_s are the indices for the orbital angular momentum and its z-component, and the spin and its z-component, respectively.

Parity	Changes	Notes
l	$\Delta l = \pm 1; \Delta m = +1$	excited by σ^+ circular polarization
	$\Delta l = \pm 1; \Delta m = -1$	excited by σ^- circular polarization
s	$\Delta s = 0; \Delta m_s = 0$	

of the XMCD effect is as follows. As the angular momentum of the photon is absorbed by the electron, the spin-orbit interaction couples part of that angular momentum to the spin, resulting in the creation of spin-up, or spin-down electrons for the $2p_{3/2}$, $2p_{1/2}$ levels, respectively, as a result of the opposite sign of the spin-orbit coupling of these two states. Here, the spin quantization axis is

the x-ray propagation direction. Right (σ^+) and left (σ^-) circular polarizations are also defined with respect to this axis, and correspond to the photon helicity being parallel and antiparallel to it, respectively. Because of the dipole selection rules, the $2p - 3d$ electronic transitions conserve spin. But the $3d$ level is exchange-split, so there are fewer available final states for spin-down electrons than for spin-up (the relevant quantization axis for the transition is now the magnetization direction). Thus, when the beam propagation axis and the magnetization are closely aligned, a magnetic filtering effect occurs. For example, if the two quantization axes are antiparallel (i.e. a spin-up electron in the material is also spin-up along the beam direction), then the σ^+ polarization is going exhibit much higher absorption than σ^- if the beam is tuned to the L_3 edge, and vice-versa for the L_2 edge.

XMCD is not only a microscopy technique, but also a powerful technique for magnetic spectroscopy, because the spin and orbital contributions to the magnetization can be experimentally determined using sum rules for the helicity-dependent absorption differences at each of the two edges. Information about magnetocrystalline anisotropies can also be obtained. A more detailed description of XMCD, including also the effects of orbital angular momentum, can be found, for example, in Ref. [150]. However, spectroscopy is outside the scope of this study, where we were not interested in the material properties, but rather in the static configuration and steady-state dynamics of the magnetization, as described in more detail below. For this, it is both necessary and sufficient to look at a single edge, and reverse the x-ray polarization in order to extract the (weak) magnetic intensity contrast $\Delta I/I$ from the topography-dominated raw data for each polarization. Equation 5.1 describes this process [148]

$$\frac{\Delta I}{I} = \frac{I^+ - I^-}{I^+ + I^-} = -tanh(P cos(\theta) \mu_c d) \tag{5.1}$$

where I^+ (I^-) is the transmitted intensity of the right-polarized (left-polarized) x-rays for a given edge, P is the degree of polarization of the beam, θ is the misalignment angle between beam and magnetization, μ_c is the spin-dependent part of the absorption coefficient (per unit thickness) and d is the thickness of the sample. The argument of the hyperbolic tangent is usually very small, so the approximation $\Delta I / I \approx -P cos(\theta) \mu_c d$ can be used.

Before I move on to our experiment I would like to describe briefly the main factors affecting the magnitude of the circular dichroism. In particular the circular dichroism increases in materials with a large number of $3d$ holes (this increases the overall absorption) and a large magnetic moment (this increases the contrast between the two x-ray helicities). Larger spin-orbit splitting of the $2p$ level also increases the contrast.

Table 5.2 shows the number of $3d$ holes and the net spin moment in Bohr magnetons for three $3d$ ferromagnetic elements. The low number of $3d$ holes and low magnetic moment of Ni make it the least optimal $3d$ ferromagnetic

Table 5.2: Number of $3d$ holes and the net spin moment in Bohr magnetons for three $3d$ ferromagnetic elements. The spin moment values values are from [153, 154].

Element	Number of $3d$ holes	Spin moment
Fe	3.4	2.69
Co	2.5	1.64
Ni	1.5	0.62

element for XMCD imaging, even though it has a larger atomic number[1] Z (and hence stronger spin-orbit splitting) than the other two ferromagnetic elements shown in the table. Despite the lower contrast and overall absorption associated with Ni it is nevertheless the primary material we imaged in this study because it allowed us to distinguish between the vortex layer and the thinner magnetic layer of our devices, as explained further below.

5.2 Motivation of the study

The electronic transport properties of spin-torque oscillators have been studied extensively, but the details of the magnetic structure and its dynamics have remained hidden. Here we present the first images of the ground-state vortex structure in a 3-dimensional (3D) nanopillar and its steady-state oscillation induced by a dc spin current. In particular, we report real space, time-resolved x-ray images that identify the precession of the vortex core which leads to microwave emission, as well as deviations from the behavior expected from an ideal vortex. The elemental selectivity of the x-ray technique allows us to isolate the magnetization of the magnetic layer of interest, while the combined high temporal and spatial resolution of time-resolved x-ray microscopy allows the underlying magnetization dynamics to be observed in detail. The spin-torque-driven dynamics are shown to be closely-dependent on the unexpectedly complex 3D vortex profile, while at the same time they maintain a simple dependence on the vortex handedness, despite the strong nonlinearity of the system.

---

[1]A large atomic number Z also leads to a larger non-magnetic absorption of the x-rays, which is detrimental for the overall sensitivity of the experiments since fewer photons make it through to the detector.

5.3   Description of experiment

We studied devices with a spin valve structure as shown in Fig. 5.2, with a 60 nm-thick magnetic layer composed of $Ni_{81}Fe_{19}$ and a thinner (5 nm) magnetic layer composed of $Co_{60}Fe_{20}B_{20}$, separated by a 40 nm-thick Cu spacer. The samples were patterned into nanopillars having elliptical cross-section with a major axis of ~170 nm and a minor axis of ~120 nm. To allow x-ray transmission, the Si wafer was etched, leaving the pillars suspended on 200 nm-thick low-stress silicon nitride windows.

Persistent gigahertz-frequency voltage oscillations are excited when a direct current is applied corresponding to electrons flowing from the thin magnetic layer to the thick magnetic layer, with the transport properties being typical for this type of device [61]. The oscillations exhibited by our samples have narrower linewidths for finite applied magnetic fields, but all the data reported here were obtained at zero field, where the linewidths were on the order of 10 MHz.

The x-ray experiments reported here were carried out at the Advanced Light Source (ALS), using the Scanning Transmission X-ray Microscope (STXM) on beamline 11.0.2 (see Fig. 5.3) [155]. The spatial resolution of the STXM is about 30 nm and the temporal resolution of our experiment is about 70 ps, limited by the pulse-width of the x-ray pulses. The samples were excited by a direct current of ~3-8 mA and all measurements were performed at room temperature. One of the many challenges of using the instrument is that over the course of the x-ray measurement the devices and surrounding area that is scanned by the beam become gradually coated with a layer of organic compounds that steadily decreases the transparency to x-rays and eventually renders further imaging of
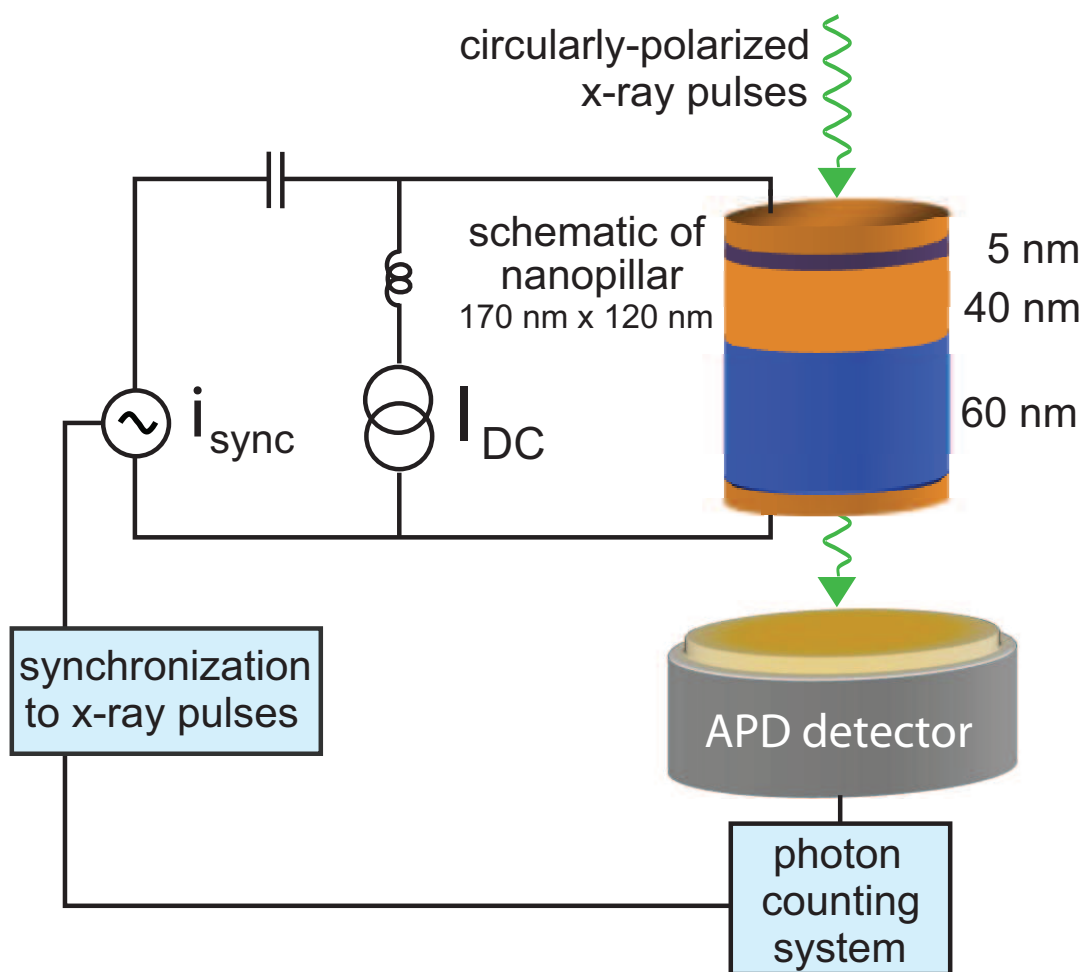
Figure 5.2: Schematic of the experimental setup. The sample is positioned perpendicular to the incoming x-ray pulses and the transmitted x-ray intensity is recorded by an avalanche photodiode (APD) detector. The pulse repetition frequency is $f_{ALS} \sim 500$ MHz (see Methods for details).
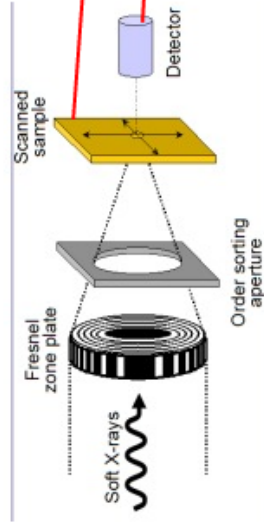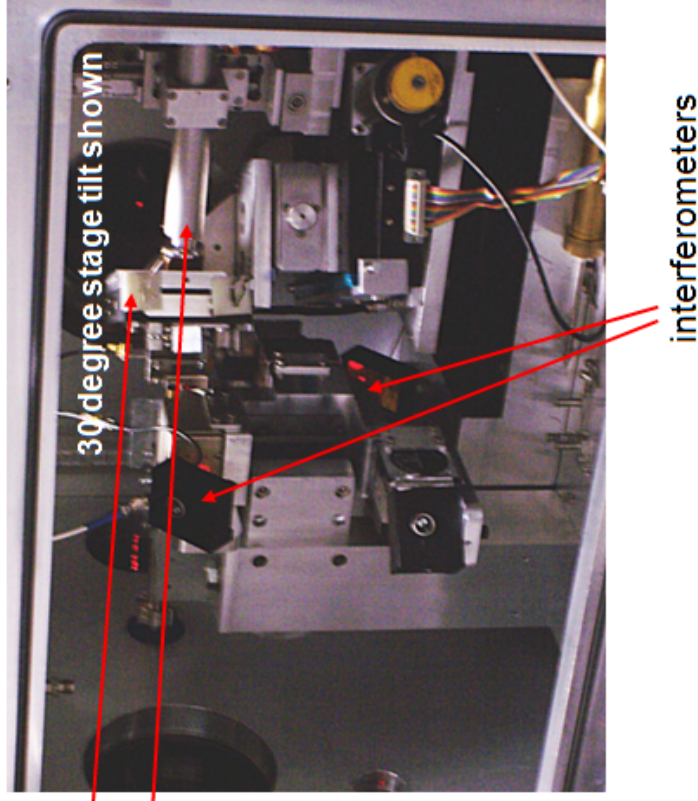
Figure 5.3: Illustration of the Scanning Transmission X-ray Microscope on beamline 11.0.2 at the Advanced Light Source. The x-rays are focused using a Fresnel zone plate made of gold on a low-stress silicon nitride membrane, and after focusing pass through an order-selecting aperture. Piezoelectric actuators are used to scan the sample stage in front of the beam.

111

the device impossible. Unfortunately, cleaning of the devices was not possible, even with O_2 plasma in an Reactive Ion Etcher. Therefore, the devices must be measured judiciously due to their limited microscopy lifetime. In order to reduce the rate of organic compound deposition the chamber was periodically pumped and refilled with an exchange gas at low pressure[2].

5.4   Synchronizing the dc-driven oscillations

Typically the synchronization of magnetization dynamics to x-ray pulses is done using a "pump-probe" approach: the "pump" consists of pulses of magnetic field or electric current to study the response to transient excitations [88, 118, 116, 156, 157] or continuous sinusoidal signals to study resonant behaviors [119, 158, 159, 160], while the "probe" consists of circularly polarized x-ray pulses. However, since in our experiment the dynamics were driven by a direct current instead of pulses or ac signals, the synchronization between the sample and the x-ray source is nontrivial and cannot be achieved by means of the standard "pump-probe" technique. Instead, we developed a new method that relies on injection locking [161] to phase lock the dc driven oscillation to a small ac current i_{sync}. Fig. 5.2 shows the schematic of our setup: a direct current I_{DC} was applied to the sample to excite the steady-state GHz oscillation, a small alternating current i_{sync} was added to I_{DC} to synchronize the sample oscillation to x-ray pulses. The root mean square value (RMS) of the phase-locking

---

[2]We also observed a slow increase in the oscillation linewidth after repeated measurements, which we think could be due to a degradation of the magnetization due to heating effects of the applied current. Indeed, cooling occurs primarily in two ways, both of which are relatively inefficient: i) horizontally through the metallic leads (which have a small cross-section) or ii) directly by conduction to the exchange gas (which is at low pressure). Direct cooling to the substrate, which would be efficient, is not possible due to the fact that the devices are suspended on the membrane.

current i_{sync} was less than 7% of the direct current which drives the magnetization dynamics. A photon counting system was developed to distribute the x-ray transmission signals recorded by an avalanche photodiode detector (APD) to 16 different channels, corresponding to 16 equally-spaced phases of the oscillation.

To probe the thick magnetic layer only, the x-ray energy was tuned to the Ni L_3 edge and STXM images of the sample transmission intensity $I^+(x, y)$ and $I^-(x, y)$ were recorded using right and left circularly polarized x-rays. Fig. 5.4a) is a typical x-ray transmission image of our sample where topography contrast strongly dominates over magnetic contrast. Darker regions indicate that the sample absorbs more of the incident x-rays, indicating the position of the nanopillar. To suppress the topography contrast, we computed the normalized difference $\frac{I^+(x,y)-I^-(x,y)}{I^+(x,y)+I^-(x,y)}$, and the resulting image of the differential intensity is shown in Fig. 5.4b)[3]. The magnetic contrast of this figure comes from the X-ray Magnetic Circular Dichroism (XMCD) effect [148, 149]. The sample surface is perpendicular to the x-ray propagation direction, thus the contrast in Fig. 5.4b) corresponds to the out-of-plane magnetization of the thick layer.

5.5 3D ground state of a strongly-confined vortex

We studied both the equilibrium magnetic state of these samples without any external excitation and the persistent oscillations excited by a direct current. The static measurement[4] shown in Fig. 5.4b) confirmed that the magnetic configu-

---

[3]Additional details of the synchronization of the oscillations and alignment of the images to correct for spatial drift can be found in Xiaowei Yu's 2009 Stanford Ph.D. dissertation.

[4]Imaging of the thinner magnetic layer (the polarizer) yielded only a very weak signal, due to its much lower thickness and the strong attenuation across the thick nanopillar stack and nitride membrane.
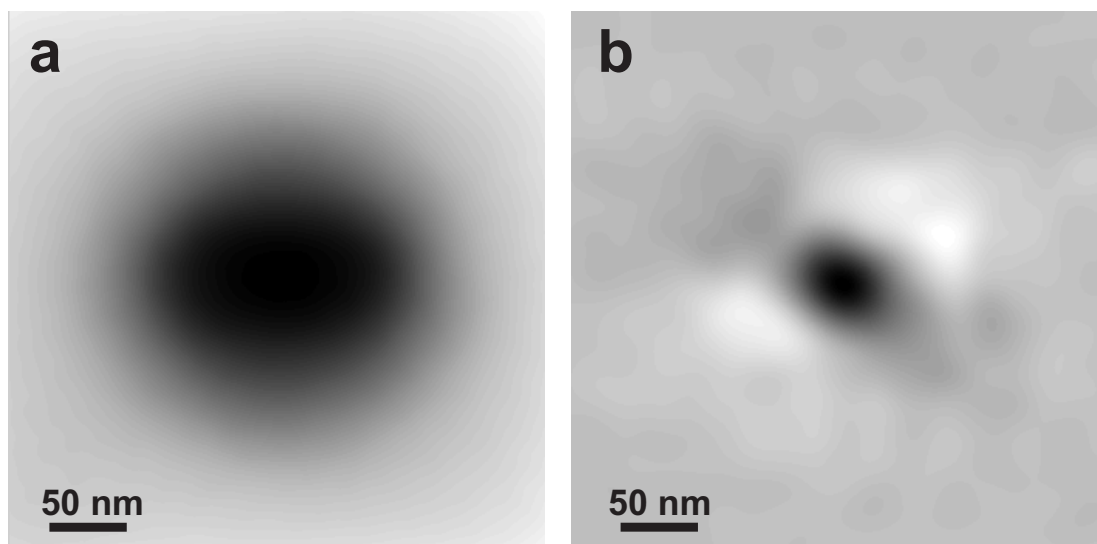
Figure 5.4: Static STXM image and magnetic image. **a**, STXM image showing mainly topographic contrast. **b**, Magnetic image deduced from STXM images showing XMCD contrast corresponding to the out-of-plane magnetization.

ration of the thick layer is a magnetic vortex. However, besides the black area in the center of the image corresponding to the vortex core, there are also two lighter regions indicating a considerable out-of-plane magnetization component with opposite orientation to that of the core. To depict this magnetization distribution more clearly, the pillar area in Fig. 5.4b) is plotted in Fig. 5.5 (top) using both pseudo color and a surface plot, where the height is proportional to the out-of-plane magnetization. The out-of-plane magnetization decays from the center of the ellipse to its edge; the decay is most pronounced along an axis that lies between the major and minor axes, with the magnetization turning to a direction opposite that of the core near the edges. The data also clearly shows that the magnetization breaks the symmetry of the elliptical shape of the sample. The observed distortions indicate that the static vortex profile strongly deviates from an ideal vortex profile, where the magnetization lies in plane everywhere except at the core.

To better understand this unusual vortex profile, we conducted micromagnetic simulations of an isolated Permalloy (Py) pillar with the same dimensions as the thick layer in our samples using the LLG Micromagnetic Simulator [162]. The simulated grid size is 2 nm $\times$ 2 nm $\times$ 2 nm and the material parameters are 1.3×10^{-11} J/m for the exchange constant and 8×10^5 A/m for the saturation magnetization. The bottom part of Fig. 5.5 shows the simulation results for the in-plane distribution of the out-of-plane magnetization at the top, in the middle, at the bottom, and averaged over the whole Py pillar. The average magnetization and the magnetization in the middle of the pillar are very similar, following the symmetry of the pillar shape and remaining mostly in plane except in the center and at the edge. However, the out-of-plane magnetizations on the top and bottom surfaces break the in-plane symmetry and have mirror symmetry

between them. In the simulations the top and bottom are identical to each other so the direction of symmetry breaking depends on the initial conditions, which are random (i.e. it behaves as a *spontaneous* symmetry breaking). The variation
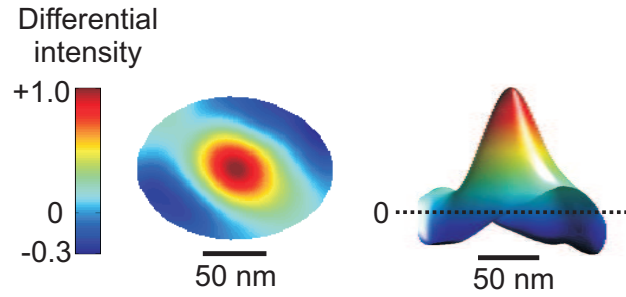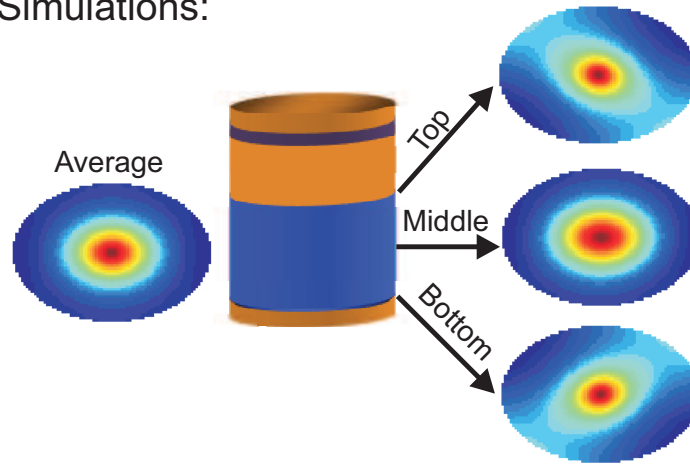
Figure 5.5: Comparison of experimental data and micromagnetic simulation of the static magnetization distribution. Top: The magnetic contrast within the sample area of the magnetic image, Fig. 2b, with pseudo color (left) and its surface plot (right), where the height is proportional to the out-of-plane magnetization. Bottom: Micromagnetic simulation, showing the out-of-plane component of the equilibrium magnetization in different planes of an isolated 60 nm-thick Py pillar with the same dimensions as in our sample (as shown).

of the magnetization across the sample normal axis shown in the simulation is a consequence of the 3D nature of magnetic elements whose thickness is comparable to the lateral size [163, 164, 165]. Although most studies of micro- and nano-scale magnetic elements have focused on two-dimensional structures, the magnetic vortex as a ground state in a spin-torque device is almost inevitably 3D in nature. Spin-transfer devices need to have small lateral dimensions in order for the spin-torque to dominate over the adverse effect of the Oersted field. Due to this requirement on the lateral dimensions, which implies very advantageous scaling properties for spin-torque devices, the thickness of a magnetic layer needs to be well above the exchange length in order to energetically favor the vortex state over the single domain state. The 60 nm thickness of our vortex layer is considerably larger than the exchange length for Permalloy, which is about 5 nm. Hence the magnetization is expected to be inhomogeneous across the normal axis, resulting in the different magnetization distributions on the top surface, in the middle, and on the bottom surface.

Surprisingly, Fig. 5.5 shows that our x-ray data is rotated with respect to the device long axis. Although the XMCD contrast deduced from x-ray transmission images corresponds to the magnetization averaged along the entire normal axis of the vortex layer, the data is similar to the simulated magnetization distribution at the top and bottom surfaces of the Py pillar, but not to the simulation average over the entire layer. In the simulations we found that introducing a tapered sidewall ranging between 10 and 30 degrees (not shown), as exhibited by real devices as a result of ion milling, can reproduce part of the rotation, however the effect is not as pronounced as in the x-ray data. The simulations also indicate that interface anisotropy [166] or magnetic coupling from the thin layer do not account alone for the magnitude of the observed rotation in the data.

We believe that other factors, such as a possible deviation of the real device shape from an ideal ellipse might also contribute to explain why the rotation is considerably greater in the data than in the simulations. An additional possibility is that the absorption coefficient might vary between the top and bottom parts of the thick layer. This could occur, for example, as a result of possible inter-diffusion between the vortex-containing thick Py layer and either the Cu spacer (at the top) or the Ta immediate underlayer (at the bottom) during the hotter steps of the fabrication process, which reach 170°C. Overall, the asymmetric vortex profile revealed in our x-ray data can thus be understood in two steps: first the 3D nature of the thick magnetic layer breaks the symmetry of the magnetization distribution within the surfaces; second, the mirror symmetry between the top and bottom surfaces is also broken due to the asymmetric environment in the experimental device, arising from the interlayer coupling, the tapered profile of the device sidewalls and possibly other shape non-idealities.

5.6 Trajectory of a spin-torque-driven self-oscillating vortex at zero applied field

Our dynamic measurements of the 16 evenly-spaced phases of the magnetization dynamics directly confirm that the GHz-frequency GMR signal observed under dc bias [61] originates from the vortex translational mode (see supplementary video 1). Fig. 5.6 shows the vortex core trajectory (red) of a sample oscillating at 0.95 GHz, excited by a direct current of 7.8 mA (i_{sync} ~0.4 mA RMS), and the core positions for the same sample without any excitation (black). The static core positions are recorded by the same photon counting system used for

the dynamic measurement, thus they provide an estimate of the uncertainty of the vortex core trajectory. Using the standard deviation of the recorded static core positions, we depict the uncertainty of the dynamic core positions by the transparent red disks. There are several sources contributing to the uncertainty of the core positions, including the limited spatial resolution, fluctuations in the photon counters, the finite width of the x-ray pulses (~70 ps at full width half maximum), and the jitter in the synchronization, which is about 66 ps. In both samples we studied in detail the core orbit appears to be is elongated and irregular. Moreover, the static core position seems shifted by several nanometers from the origin, which could be due to the effect of the dipole field from the thin layer. We note, however, that a conclusive interpretation of the significance of these two specific features is made difficult by the size of the position uncertainties. The radius of the vortex trajectory is ~10 nm, as shown in Fig. 5.6, much smaller than that seen in resonating vortex core gyration excited in single-layer devices by ac magnetic field (e.g. ~100 nm in Ref. [160]), ac current (e.g. ~250 nm in Ref. [158]), or dc driven vortex gyration in a metallic nano-contact with an out-of-plane external magnetic field (~158 nm in the simulations in Ref. [109]). Unlike in resonant dynamics, where the size of the orbit strongly depends on the amplitude of the periodic excitation, in the persistent oscillations measured here, which are sustained by a direct current, the core trajectory satisfies a subtle balance between the work done by spin-torque integrated over a cycle and the energy dissipation.
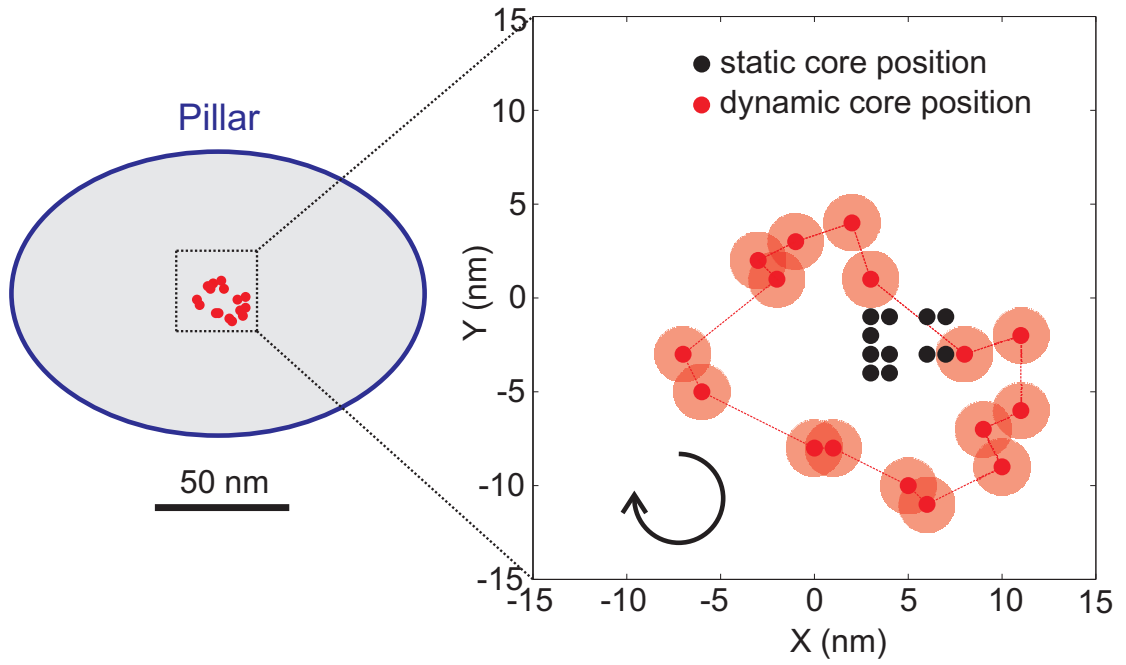
Figure 5.6: Vortex core trajectory deduced from STXM images. Black dots: static core positions recorded by 16 photon counters. (Some of the static positions overlap.) Red dots: core positions of the same sample during the oscillations, recorded by the same photon counters. Red disks: an estimate of the position uncertainty by using the standard deviation of the static core positions. The direction of vortex gyration is clockwise, as indicated.

5.7 Handedness and nonlinear vortex oscillations

Time-resolved images of the same sample, but having the opposite core polarity due to its magnetic history (as evidenced by the change from white to black contrast in the center of the normalized difference images) reveal that the core moves counterclockwise, opposite to the direction of gyration for the case shown in Fig. 5.6 (see supplementary video 2). The oscillation frequency is 1.26 GHz with a direct current of 5.1 mA (i_{sync} ~0.4 mA RMS). (The vortex frequency of 0.95 GHz measured for the initial core polarity is inaccessible after the polarity switches because the oscillation frequencies move to a higher range after the core flip.) This observation is consistent with the conclusion in Ref. [118], that the direction of the vortex gyrotropic motion is determined by the direction of the out-of-plane magnetization at the core, or the handedness of the vortex. Our result shows that even when the effect of spin-torque is strong enough to balance the damping, an intrinsically nonlinear effect, the vortex core rotation direction is still determined by the internal structure of the vortex, just as for a freely relaxing magnetic vortex.

5.8 Vortex non-ideality and spin-torque efficiency

The magnetic vortex profile revealed by our x-ray data makes it very challenging to describe analytically the magnetization dynamics reported here. Most vortex dynamic models assume an "ideal" vortex profile where the magnetization is uniform along the normal axis and the in-plane distribution maintains the sample topographic symmetry [94, 156, 102, 103]; however, these models are not strictly applicable to our case due to the 3D nature of our magnetization

121

distribution. For example, Ref. [109] concludes, through use of the Thiele equation [89, 91], that only the perpendicular component of the spin polarization can sustain persistent vortex gyration, while the in-plane component leads only to vortex core displacement. In contrast, our x-ray data clearly shows that in our samples the vortex undergoes steady-state oscillation under the influence of a predominantly in-plane spin-polarized longitudinal current. One possible reason for the discrepancy is the unusual profile of the vortex in spin valve nanopillars such as studied here, since both the damping force and the spin-torque force in the Thiele equation are strongly dependent on the vortex magnetization distribution. Another possible reason is the periodic distortion of the vortex core along the normal axis observed in simulations of the dynamics [61] (see also Fig. 3.3). Such a periodic distortion of the core during the gyrotropic motion is not describable using the existing models of vortex dynamics. However the prediction that an in-plane polarized spin current should not induce gyration at all in the ideal case can likely provide the basis for the explanation of why the zero-field gyration orbit observed experimentally with a vortex that has a non-ideal profile has such a small radius.

5.9 Summary of relevant frequency and time scales

Since this chapter contains a number of important frequency and time scales, I am listing them below, in Table 5.3, for easier comparison with each other.

Table 5.3: Relevant frequency and time scales for the time-resolved x-ray imaging experiment.

Typical oscillation frequency of vortex	~ 0.9 to 1.3 GHz
Pulse repetition frequency	0.499642 GHz
Resolution of frequency mesh for sampling frequency	0.015 GHz
Sampling frequency	~ 0.95 to ~ 1.55 GHz (see Methods section for details)
x-ray pulse width in time	0.07 ns

5.10   Conclusions

In summary, we have presented the first direct images of the magnetization dynamics in a dc-driven spin-torque oscillator. For a vortex oscillator, we find that the magnetization profile deviates significantly from the ideal 2D structure, due to the 3D nature of the thick magnetic pillar, its asymmetric environment and the small dimensions typical of all spin-torque devices. We find that these non-idealities play a crucial role in the excitation of the oscillations, a fact that is currently not taken into account by analytical models. On the other hand, we find that the polarity of the vortex core has a robust effect on the oscillations, such that even under the effect of the strongly nonlinear spin-torque, it still determines the vortex gyration direction, as for linear vortex dynamics in the absence of spin-torque. While in this work we focused on the spin-torque-

driven oscillations of magnetic vortices due to their particular technological importance, our technique based on nonlinear phase-locking is quite general and can be used to image any dc-driven magnetic nano-oscillator.

5.11 Methods

5.11.1 Additional details of the synchronization scheme

A phase-lock loop is used to synchronize i_{sync} to the the x-ray pulses generated by the Advanced Light Source (ALS). Since the frequency of the dc driven oscillation is not in general a multiple or divisor of the x-ray repetition rate, $f_{\text{ALS}} = 499.642\,\text{MHz}$, we used a frequency grid with $f_{\text{ALS}}/32 \simeq 15\text{MHz}$ increments and tuned the amplitude of the direct current I_{DC} so that the sample frequency is a multiple of the frequency grid, i.e., $f_{\text{sample}} = M \times f_{\text{ALS}}/32$, where M is an integer ranging between 61 and 99 in our experiment. If M is an odd number, then the result of the synchronization is that the x-ray pulses probe 32 different phases of the sample dynamics simultaneously. Our photon counting system is similar to that used in Refs. [151] and [167], except we increased the number of counters from 8 to 16, so as to record 16 or 32 dynamics phases.

CHAPTER 6

CONCLUSIONS

This dissertation summarized my experimental results on the spin-torque driven steady-state oscillations of a magnetic vortex within a spin-valve nanopillar structure.

The manipulation of nanoscale magnetic moments by means of the torque applied by a spin-polarized current has been the focus of intense research since the theoretical predictions of this effect in 1996 [40, 41], and has grown to be one of the largest subfields of magnetism over the last few years. Both fundamental and applied research has been motivated in large part by the promise of novel spintronics applications, such as non-volatile magnetic memories and tunable, dc-driven gigahertz-frequency oscillators.

In my first study I discovered that a quintessentially nonuniform magnetic structure, a magnetic vortex can also be excited into persistent GHz-frequency oscillations by a spin-polarized dc current. The details of the motion are more complex than for a uniform magnetization, and as I have described in the dissertation, a satisfactory understanding of the motion is still missing. However, by comparing the experimental results from electrical transport measurements to micromagnetic simulations I found out that the oscillations correspond to the precession of the vortex core. This is an exciting result from a fundamental point of view because the core precession is closely related to the lowest-frequency excitation of a vortex, the gyrotropic mode. Moreover, from the standpoint of potential applications, as on-chip tunable microwave oscillators, two features set the vortex oscillator apart from the previously studied vortex-free oscillators: i) the vortex oscillations can be obtained in zero magnetic field, allowing for eas-

ier integration with standard semiconductor fabrication techniques, and ii) the vortex oscillators exhibit the narrowest linewidth of any spin-torque oscillator, with measured values of less than 300 kHz at room temperature, at frequencies of $\sim 1 - 2$ GHz, which means that they can be a more coherent source of microwaves than vortex-free spin-torque oscillators.

In the second study I performed frequency domain and single-shot time domain studies of the spin-torque-driven vortex oscillations, focusing on the behavior at zero magnetic field. I observed two types of abrupt fluctuations in the frequency and amplitude, with very long random mean lifetimes ($\sim 10^2$ to $\sim 10^4$ oscillation cycles). The first type are fluctuations between two center frequencies separated by 10s of MHz that we determined to be a result of switching between quasi-uniform and vortex states of the thinner magnetic polarizing layer. The second type are much smaller, discrete frequency fluctuations that lead to a fine structure of the oscillations. I found that this fine structure plays a very important role in determining the long-time average linewidths. I will also discuss possible physical origins of these long-timescale discrete fluctuations.

In the third study, which was a joint effort with a group from Stanford and the Lawrence Berkeley Laboratory, we used soft x-rays from the synchrotron source at the Advanced Light Source in Berkeley to perform time- and space-resolved imaging of the vortex magnetization dynamics, by means of the X-ray Magnetic Circular Dichroism effect. This was the first study to image the steady-state oscillations of a nanomagnet driven by dc spin-polarized current. One of the main results of this study is that that the vortex precession is affected by a non-trivial magnetization profile which results from the small scale that is characteristic of spin-torque devices, and which is typically ignored in analytical

calculations. We also find that despite the strong, nonlinear spin-torque the sense of the vortex gyration is uniquely determined by the vortex core polarity, just as for the linear case of magnetic-field-induced vortex dynamics.

The study of spin-torque driven magnetic vortex dynamics is still full of interesting challenges, many of which I would have liked to have had time to study in more detail as part of my PhD work. One active direction of study is motivated by the desire for larger output powers. Recent progress in vortex oscillators involving a magnetic tunnel junctions [75] is encouraging and suggests that power enhancements of by several orders of magnitude more could be achieved with better integration of high-TMR junctions within Py nanopillars. Another direction is provided by the exciting possibilities of reversibly controlling the vortex core polarity [113, 114] and chirality [115] by means of spin-torque, for which only analytical or numerical proposals have been published to date. Finally, a more fundamental issue is the still incomplete understanding of the roles of various sources of decoherence in determining the observed auto-oscillation linewidths.

APPENDIX A

TABLE OF RELEVANT CONSTANTS AND LENGTH SCALES

Table A.1: Table of relevant constants and length scales. The values for the damping constant α and the spin-diffusion length l_{sf} vary significantly across publications, depending on the measurement method or model used to analyze the data. The superscript in brackets indicates the temperature at which the values were obtained, if known. The range of values of A for Fe is from [168], the values for Co and Ni are obtained from calculations in [169], while the value for Py is that often used in micromagnetic simulations. The values of M_s are from [170]. The values of α are from [171], except for the value for Py, which is from [172]. The values of l_{sf} are from [173].

Material	A (J/m)	M_s (kA/m)	α	l_{ex} (nm)	l_{sf} (nm)
Fe	0.3 to 2×10^{-11}	1700^{293K}	0.01^{293K}	1 to 2	$8^{4.2K}$
Co	1.0×10^{-11}	1450^{293K}	$0.008^{4.2K}$	2	38^{300K}
Ni	2.0×10^{-12}	490^{293K}	0.02^{293K}	3	$21^{4.2K}$
Py ($Ni_{81}Fe_{19}$)	1.3×10^{-11}	800^{293K}	0.01^{293K}	4	3^{293K}
Cu	-	-	-	-	$(350 - 700)^{293K}$

APPENDIX B

TEMPERATURE DEPENDENCE OF SPIN-TORQUE DRIVEN VORTEX OSCILLATIONS AT ZERO APPLIED FIELD

I measured the temperature-dependence[1] of the vortex oscillations at zero applied field on devices as those discussed in Chapters 3 and 4. Below, I show data from Device 1 of Chapter 4. The behavior as a function of temperature is quite complex, as shown in Fig. B.1. In particular, note that at temperatures of 176 K or less, only Mode 1 is observed. Fig. B.2 shows the temperature-dependence of the frequency, linewidth and power for $I = 5.0$ mA. The linewidth decreases and the power increases monotonically as the temperature is reduced at this current value. However, at a larger current value of 11.0 mA, the opposite trend is observed, as shown in Fig. B.3. At this current value, Mode 2 is also active (not shown), but only for $T \geq 220$ K, where Mode 1 is not detected. The linewidth of Mode 2 also increases with decreasing temperature, but unlike Mode 1, its power increases.

---

[1]The temperatures shown are those indicated by a temperature sensor located near the sample. They have not been corrected for Joule heating due to the applied current.
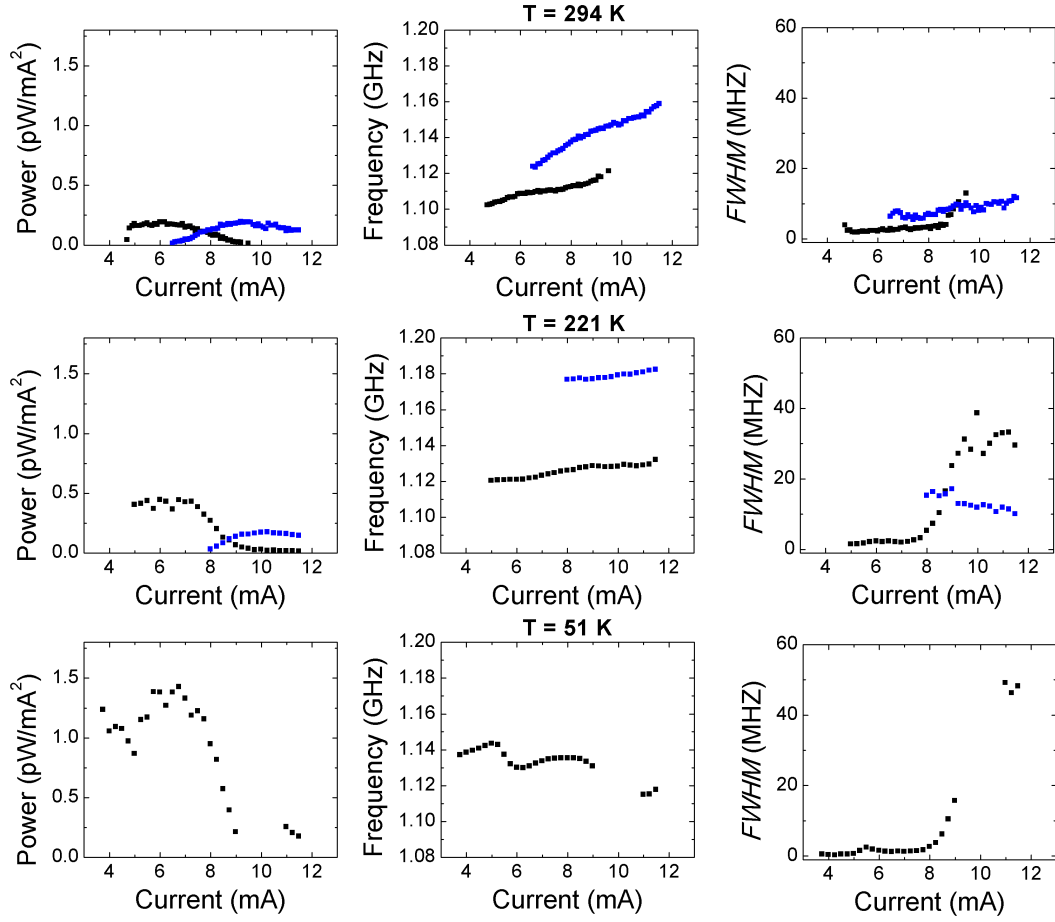
Figure B.1: Current-dependence of the power, frequency and linewidth of the resistance oscillations of Device 1 from Chapter 4, shown for three different temperatures. At 51 K only mode M1 is visible.

Figure B.2: Temperature-dependence of the frequency, linewidth and power of the resistance oscillations of Device 1 from Chapter 4 for Mode 1 (low-frequency mode) at I = 5.0 mA
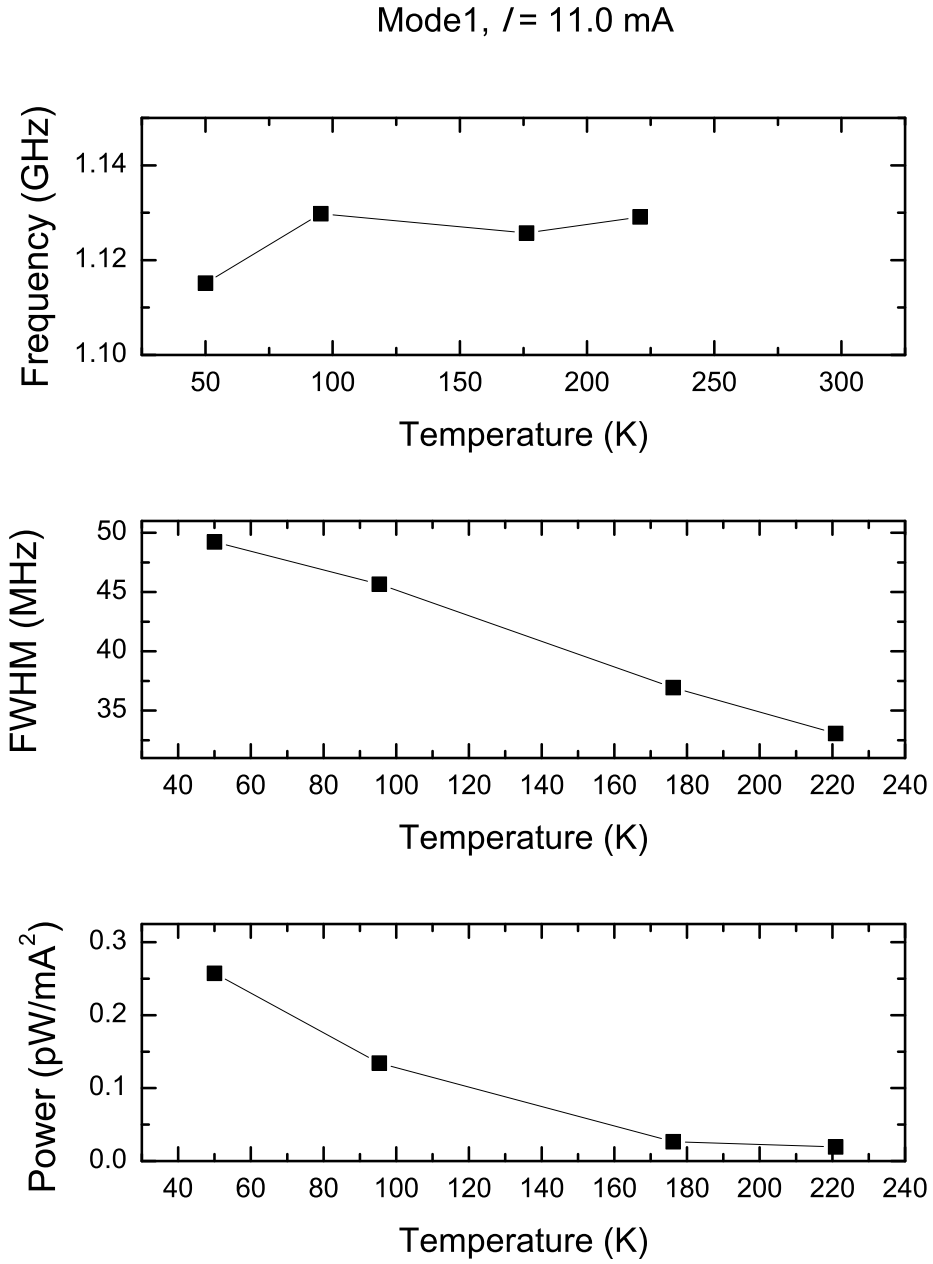
Mode1, I = 11.0 mA
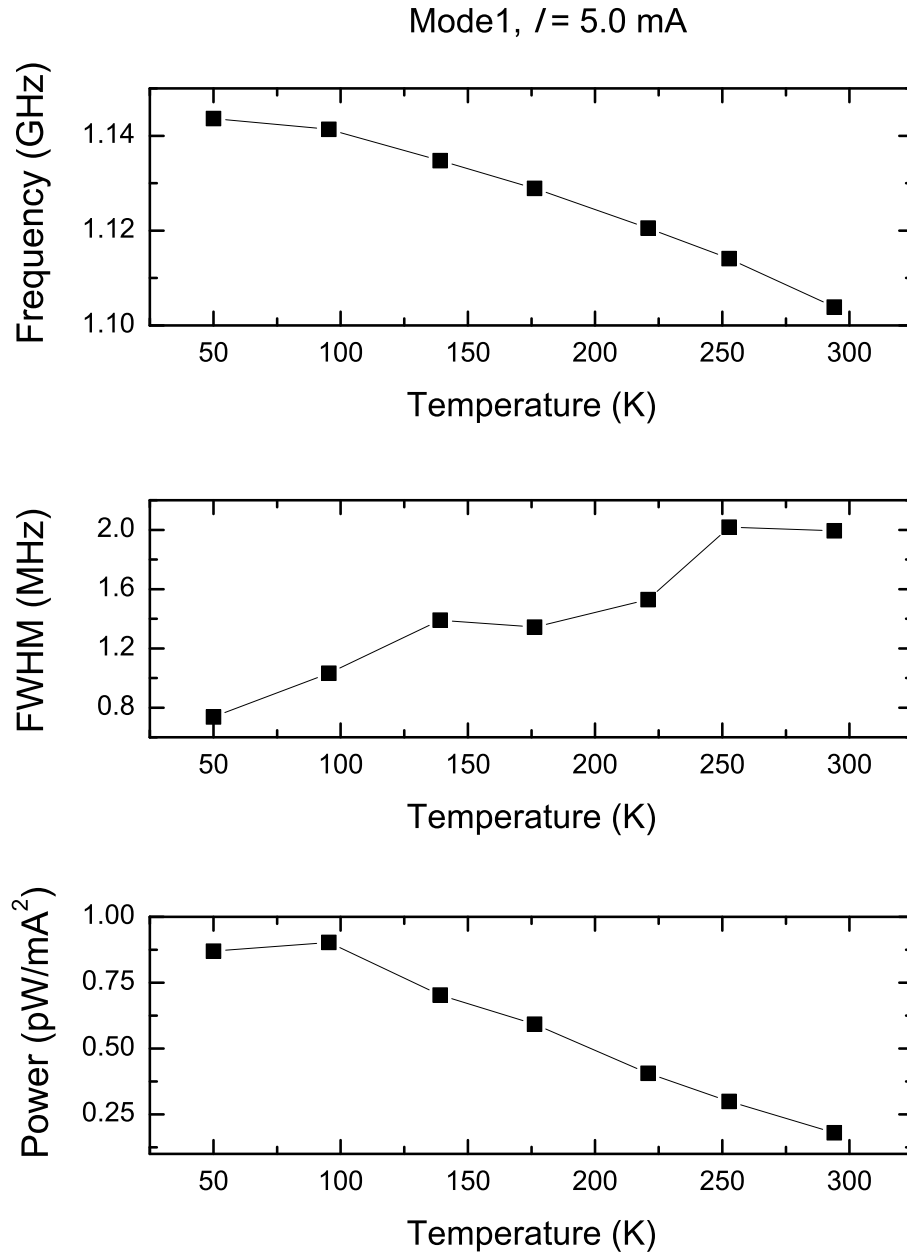

Figure B.3: Temperature-dependence of the frequency, linewidth and power of the resistance oscillations of Device 1 from Chapter 4 for Mode 1 (low-frequency mode) at I = 11.0 mA

APPENDIX C

VORTEX OSCILLATIONS USING A SYNTHETIC ANTIFERROMAGNET AS POLARIZER

I have fabricated and studied, with help from Jun Park, a set of devices that have a vortex in the thick layer, but employ a synthetic antiferromagnetic trilayer as polarizer, instead of the more usual single ferromagnetic layer described in Chapters 3 through 5. Most of these devices also have a circular cross-section, as opposed to the elliptical cross-section of devices in Chapters 3 through 5. Below, I show some preliminary data from our experimental studies of dc-driven dynamics of these devices. A number of basic features of the devices have been identified through our measurements: i) at room temperature, dc-driven self-oscillations are visible only over narrow regions of field and current, ii) at low temperature (we have studied 70 K and below) the dynamics exist over a much broader range of the applied field and current, iii) dynamics are generally observed only at fields above ~ 500 Oe, iv) the frequency is generally higher than the typical vortex gyrotropic-like frequency, and can be as high as 7 GHz, and v) linewidths can be as narrow as 2.2 MHz (at a frequency of 5.2 GHz). As of the moment of writing of this thesis this is still work in progress.

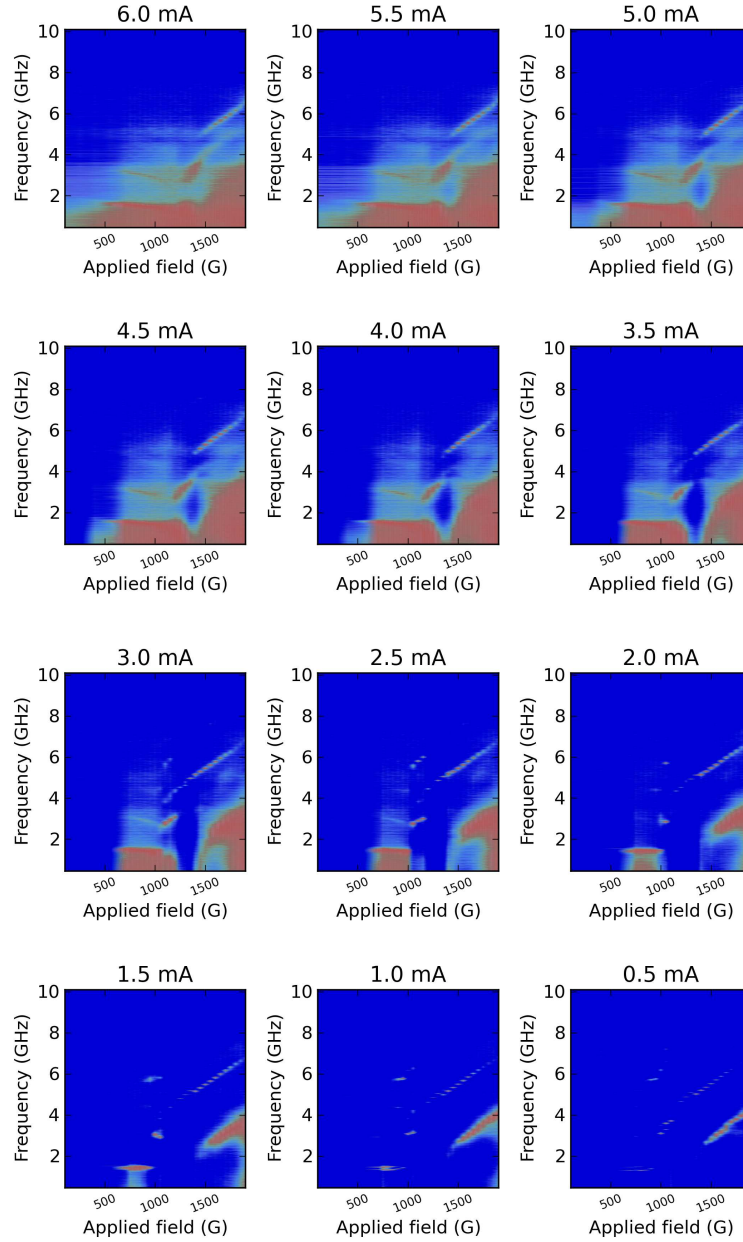**Figure** C.1: Field-dependence of spectra for a device with a vortex and a SAF polarizer. The applied field is in-plane and the chip temperature is 42 K. The sample structure is [Ta50/CuN$_x$200]$_2$Ta250/Py600/Cu100/Py30/Ru7.5/Py30 /Cu200/Pt300, with thicknesses in Å. The diameter is ~ 95 nm. The color scheme encodes the output power, with blue being low values.

APPENDIX D

CONTROLLING THE VORTEX CORE POLARITY USING A PERPENDICULAR POLARIZER

As mentioned in Chapter 2, control of the core polarity by means of spin torque presents an exciting challenge. I have been interested in pursuing this from an experimental point of view and have fabricated for that, with Jun Park's help, a set of nanopillar devices consisting of a vortex and an out-of-plane polarizer (implemented as a Co/Pt multilayer). Fig. D.1 shows the differential resistance vs. current for several values of the applied out-of-plane field on a device with diameter of ∼ 110 nm. Hysteretic switching is observed for some of the field values and is consistent with the switching of the core by the spin-torque (with the exception of the loop at −130 Oe). A number of non-hysteretic features are also observed. (Although these are typically associated with persistent oscillations, we see no well-defined spectral peaks when measuring in the frequency domain.) Interestingly, the hysteresis loop does not generally exhibit bistability at zero current, as can be seen from in Fig. D.1, this being due possibly to the presence of stray field from the perpendicular polarizer which stabilizes one of the core polarities at zero field. In general we see considerable device-to-device variability in the differential resistance vs. current data. One of the possible sources is a source of systematic defects in the pillar shape, which results in a stepped cross-section. We attribute this to an over-etching of the carbon mask by the plasma etcher[1] during fabrication, which left an undercut in the Cr mask.

---

[1] We have not observed such problems with our etcher of choice, the PT72 at the CNF, but unfortunately that etcher was down for an extensive period of time at the time of fabrication, so that the Oxford 80/1 had to be used instead. We have attempted to increase the etch anisotropy in order to reduce the undercut, by increasing the plasma power and decreasing the oxygen pressure. This lead to some reduction of the undercut in the test phase, but the results were inconsistent during the fabrication of the real devices. The PT72 is now again operational, so that a newly fabricated batch might show improved shape and transport behavior.

This would lead to a sudden decrease in the ion milling mask radius as the Cr is etched away and the carbon takes over during the pillar definition mill step. As of the moment of writing of this thesis this work is still in progress.
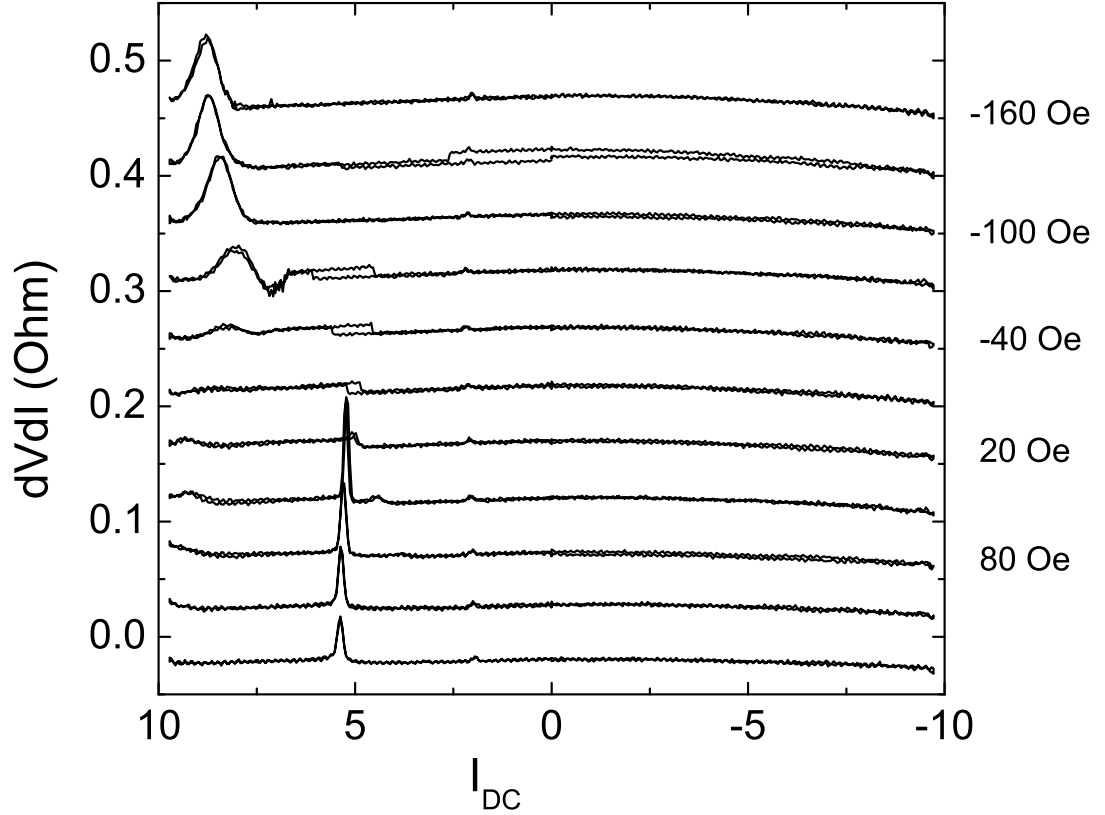
Figure D.1: Differential resistance vs. applied dc current for a sample with vortex and perpendicular polarizer. The applied field is out-of-plane and the data was taken at room temperature. The sample structure is [Ta50/CuN$_x$200]$_2$Ta50/Cu120/Pt100/[Co4.4/Pt6.8]$_8$/Co6.6/Cu3/Co6.6/Cu300 /Py650/Cu200/Pt300, with thicknesses in Å. The Co/Pt multilayer is partly patterned in order to ensure that current flows through it before entering the rest of the pillar. This patterning, in turn, results in a finite stray field from the multilayer. The diameter of this circular sample is ~ 115 nm.

FABRICATION OF NANOPILLARS ON A SILICON NITRIDE

MEMBRANE

E.1   Overview

In order to perform the x-ray transmission measurement through the nanopillar devices, as described in Chapter 5 it is necessary to make the samples transparent to x-rays. The absorption length of soft x-rays is relatively short (in the metals we used it is ∼ 20 nm), so a 500 μm thick Si wafer is not very transparent! In order to obtain a transparent substrate, I therefore fabricated the devices on double-sided polished Si wafers that had been commercially coated on both sides with a layer (150 or 200 nm thick) of low-stress SiN_x[1]. Low-stress nitride (i.e. nitride deposited under conditions that result in a lower residual tensile stress[2] than stoichiometric Si_3N_4) has several desirable properties: i) it can tolerate a certain amount of external stress when not supported from underneath, ii) it is transparent to x-rays (though less so than oxide, which however lacks the mechanical strength) and iii) it is an excellent etch stop for KOH, the most common[3] wet etchant for Si.

Thus, the fabrication process I developed with help from Zhipan Li (then postdoc in our group) consists of fabricating the devices with the standard pro-

---

[1]In principle, one can also use CNF LPCVD (low-pressure chemical vapor deposition) furnaces to deposit low-stress nitride, but it is a tedious process, and it can be difficult to get the same quality as in the industry due to the stringent requirement on the cleanliness of the wafer surface and the small size of the furnaces, which can result in poorer uniformity

[2]For the purposes of making suspended nanopillars SiN_x having a tensile stress of less than about 250 MPa is recommended. It is possible to obtain ultra-low stress nitride, at ∼ 100 MPa, for example from International Wafer Service.

[3]Although KOH is very commonly used, especially for MEMS and NEMS work, it is not compatible with CMOS processing. Other etchants, such as TMAH are compatible with CMOS.

cess on a wafer which is coated on both sides with low-stress nitride, and then etching the Si wafer under the pillars, leaving them suspended on a 200 nm thick nitride membrane (several 10's of μm on a side) that is transparent to x-rays. The KOH etching of the Si wafer requires a prior back-side-front-side aligned photolithography step (using the EV620 contact aligner at the CNF), followed by a plasma etch step (in the PT72 etcher) in order to define windows on the backside nitride from where the exposed Si will begin to etch away. Fig. E.1 illustrates the main steps of the fabrication process. Although conceptually simple the process presents a number of considerable technical challenges over our group's standard fabrication process, which I will highlight next. The end goal is to obtain a device that is both both electrically alive and accessible by X-rays. Figures E.2 and E.3 show optical microscope images of completed working devices.

E.2   Backside alignment

The first important requirement is to have accurate alignment of the backside windows to the frontside pattern, otherwise the frontside window may miss the pillar altogether. Of course, making larger windows can relax the tolerances for the alignment, but it will also result in more fragile windows. A related point is that the orientation of the front side pattern (and therefore also of the backside windows) with respect to the crystallographic axes of the Si wafer is crucial. This is a result of the fact that Si wet etching is highly anisotropic. The implication is that, in addition to good backside-frontside alignment, it is also necessary that the e-beam exposure be aligned as well as possible (within a few degrees) with the wafer flat, since the e-beam pattern and alignment marks it produces define the orientation of all successive steps. KOH achieves a selectivity of sev-

1. **Metallic films** sputtered on **Si** wafer coated on both sides with 200 nm low-stress **SiN$_x$**

2. Process devices in standard way

3. Photolithographic exposure of etch windows on the back of the wafer (aligned to front-side pattern), followed by dry etching of backside nitride to uncover Si substrate
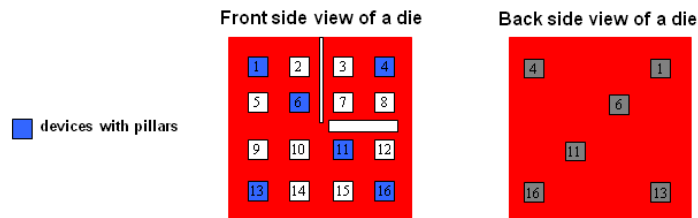
Figure E.1: Illustration of wafer geometry and main steps of the fabrication process for the nanopillars suspended on a low-stress nitride membrane. The metallic layers are shown in green, the low-stress silicon nitride in red, and the Si in gray. The two images at the bottom show a single die. A 3-inch wafer, as we typically used, would have 25 such dies in a rectangular grid, spaced apart by ~ 5 mm. As shown, only 6 devices on each die have nanopillars and windows. This was intended in order to leave more space between devices in case larger windows would be necessary, but with hindsight I think it should be possible to fully fab all 16 devices without any problems. This is true if the devices are meant to be imaged in the STXM X-ray microscope at the ALS. If the intent is to use another X-ray microscope one should first check that larger windows are not in fact necessary for aligning devices in the respective microscope.

Figure E.2: Optical microscope image of a completed device, showing the leads and the transparent low-stress nitride membrane, as seen from the front. The nanopillar is located near the center of the central square region where the leads intersect.

Figure E.3: Optical microscope image of a completed device, showing the leads and the transparent low-stress nitride membrane, as seen from the back. The image also shows the characteristic angle of the (111) planes of Si. (This is a different device that in Fig. E.2.)

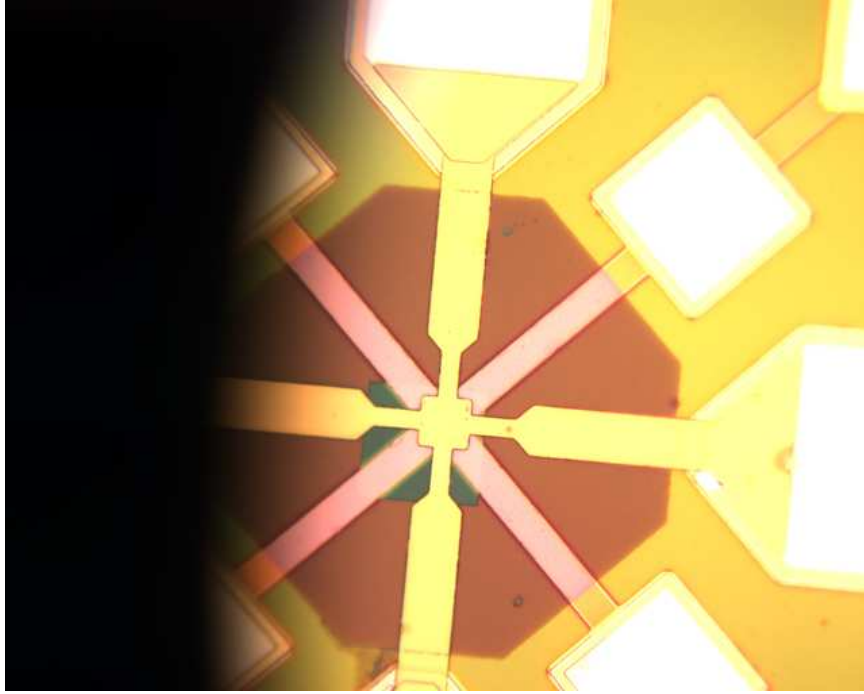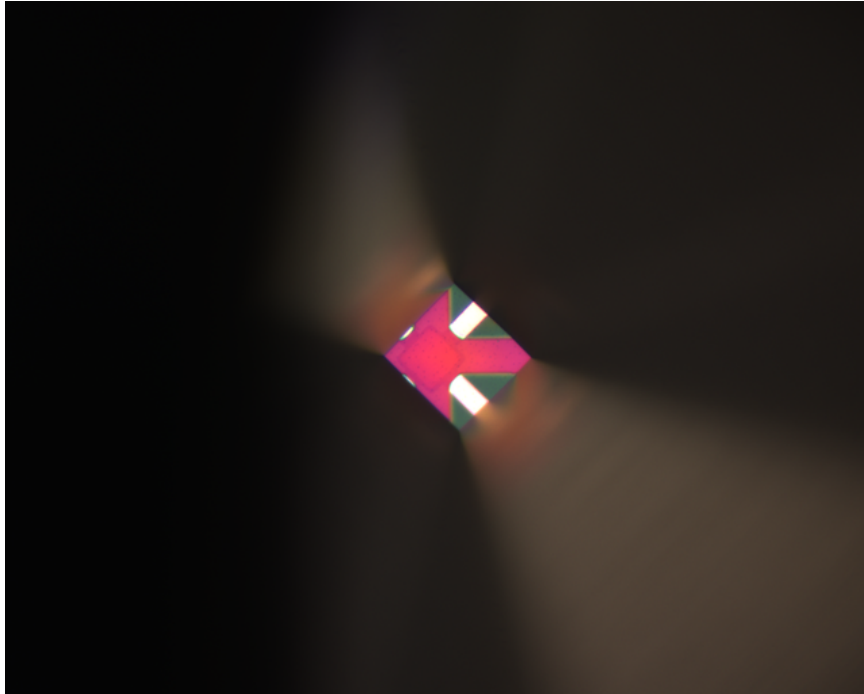eral hundred to one for etching (100) planes with respect to (111) planes. The exact ratio, as well as the absolute rates depend on the KOH concentration and temperature of the solution and follow an Arrhenius law (equation E.1), with parameters shown in Table E.1 [174].

$$R = R_0 Exp\left(-\frac{E_a}{k_B T}\right) \tag{E.1}$$

with R being the etch rate, R_0 the Arrhenius prefactor and E_a the activation energy. The wafers we used are (100) oriented (standard flat is along (110)), so the

Table E.1: Activation energies and Arrhenius prefactors for KOH etching of (100) and (110) Si. Values are from Ref. [174].

KOH concentration	(100)		(110)	
	R_0 (μm/h)	E_a (eV)	R_0 (μm/h)	E_a (eV)
20%	1.23×10^{10}	0.57	3.17×10^{10}	0.59
23%	2.69×10^{10}	0.60	8.98×10^{10}	0.62
27%	3.61×10^{10}	0.60	1.50×10^{10}	0.57
32%	9.28×10^{9}	0.57	9.88×10^{10}	0.62
34%	3.10×10^{10}	0.61	3.66×10^{10}	0.60
42%	$1.60 x 10^{10}$	0.59	$4.37 x 10^{10}$	0.60

final etch pattern has a pyramidal shape with sides at the characteristic angle of 54.7° (35.3° between the (100) direction and the (111) planes) (see Fig. E.4). If the backside mask is not aligned parallel to the (110) axis, then the pattern will align itself with this axis in the initial part of the etching, resulting in a slightly smaller final frontside window. It the misalignment is considerable and the window size tolerances are small, the window may miss the pillar altogether.
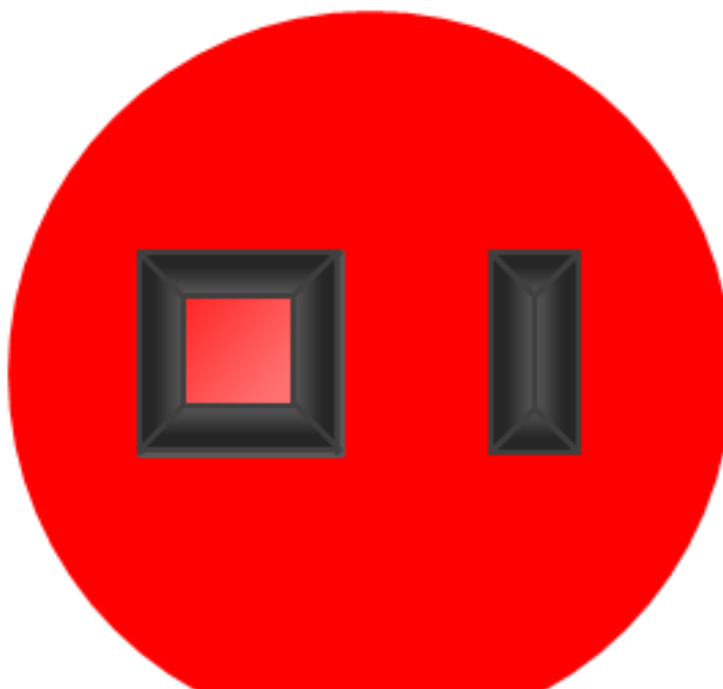
Figure E.4: Schematic of etching profile for a (100) oriented Si wafer with pattern edge aligned to the (110) flat. The pattern on the left etched all the way through to the membrane. The pattern on the right is too narrow, so the (111) planes meet before reaching the other surface.

In addition, it is important that the thickness variations across the wafer and between wafers in a batch be small ($\pm 25\ \mu$m or less for a $500\ \mu$m thick wafer and desired final window size of $\sim 25\ \mu$m). This is because large thickness variations

will throw off the window size calculations. If the thickness variations are large enough they may even result in complete absence of any frontside window (i.e. the (111) planes meet at a point before reaching the frontside membrane).

Thus the size of the backside windows is determined by the desired size of the frontside windows and the wafer thickness, subject to the fixed etch angle. Some degree of undercut due to slow but finite etching of the (111) planes will also occur, but is not very relevant for these devices. Selectivity with respect to the nitride membrane is extremely high[4], so that a 150 nm thick membrane will remain sufficiently thick to support the topside metallic features without breaking after the entire thickness of the Si wafer is etched through. It is necessary to overetch in order to ensure that the resulting window is clean. Otherwise, one ends up with opaque Si residue on the window.

E.3 Protecting the frontside nano- and microscale features during the Si deep etch

The second (and main) challenge has to do with protecting the delicate frontside nano- and microscale features against the KOH, otherwise, KOH will etch most of the metallic features very quickly. First off, it is important to be very careful to not mill through the nitride membrane when defining pillars or when isolating devices (first 2 ion milling steps in the standard fab process). While such holes in the insulator would not be a problem with usual devices, they will obviously

---

[4]PECVD nitride, with which the pillars are coated in the IPE tool (see the fab sheet), on the other hand, is extremely low quality and very porous. Consequently, it will etch, or rather disintegrate very rapidly in KOH. It is not a good KOH etch mask! The same is true for the evaporated nitride used in the "Protect Shorts" step.

be a major problem for devices meant to be suspended on a membrane, as they allow the KOH to sip through, leading to eventual damage to the frontside features. But even if one is careful about this, the fact remains that in order to do a deep Si etch with KOH the wafer needs to be submerged in hot solution for a period ranging from minutes to hours. A commercial spin-on bilayer (PROTEK) exists that is in principle designed to protect[5] delicate frontside features against KOH during the etch. However, I found out the hard way that the PROTEK coating then available at the CNF would easily peel off or puncture during the etching process, resulting in complete loss of the devices. The solution was to fabricate (out of TEFLON) a set of clamping devices that expose the backside of the wafer to the KOH, while keeping the frontside dry[6]. There are two such devices: one accommodates a full 3-inch wafer, and the other accommodates a 1 cm^2 chip, on which is located a single die. These two clamping/etching devices are currently stored in one of the two Buhrman group drawers in the CNF cleanroom. The devices are first coated with PROTEK, which acts as a secondary protection against KOH, as well as improving the seal between wafer and TEFLON clamp, and are then mounted on the clamp with the TEFLON screws, which need to be wrench-tightened by about 1/2 turn after finger-tightening them. The small clamping device also has a TEFLON washer, which is meant to ensure that the clamping pressure is entirely distributed across the chip, even as the TEFLON clamp flexes due to the tightening of the screws. Because the clamps do flex (as well as deforming plastically over time) it is important to inspect them after tightening by looking edge-on and ensuring that there is an uninter-

---

[5]Another popular method for protecting features from KOH is the so-called "black wax," but from my inquiries I found out that this is relatively messy and hard to remove completely after the etch.

[6]More recently, the CNF acquired a different batch of PROTEK. While I have not had the need to use it, according to Yongtao Cui who has tried it, this coating is now of good enough quality to protect the front surface on its own.

rupted gap between the top and bottom halves. If this is not the case, the screw pressures must be adjusted to open up the gap.

E.3.1 Details of the KOH etching procedure

The KOH etching is done in several major steps: i) etch the entire wafer to a depth of $\sim 450\mu$m (on our 500μm thick wafers), ii) cut wafer into dies (this is made easy by a grid of specially etched lines on the back of the wafer), iii) put top leads on small groups of dies, as in the standard process, and iv) etch the remainder of the Si on individual dies to uncover the nitride windows. Next I will outline the steps of the etching procedure.

Applying PROTEK bilayer

First the PROTEK bilayer is applied (in the e-beam spinners). This involves two steps:

1. Spin primer (with a 20 sec wait after applying it with the pipette and engaging the spinner)

    -60 seconds at 1000 RPM, with 20,000 RPM/sec. acceleration

    -bake for 60 seconds at 100°C

2. Spin main coating

    -90 seconds at 2000 RPM, with 20,000 RPM/sec. acceleration

    -bake for 120 seconds at 100°C

    -bake for 120 seconds at 130°C

    -bake for 60 seconds at 205°C

In order to avoid damaging the coating while handling the wafer or chips, it is important to touch only the back of the substrate. This can be achieved by using two wafer tweezers. Having applied the bilayer, the substrate can now be placed in the appropriate clamping device, as described above. Then, the clamping device is taken to the base hood.

Preparing the solution and starting the etch

In order to save time the KOH solution (concentration 25% by volume) can be be prepared before starting to apply the bilayer and can be left to warm up to about 80°C on the hotplate while spinning the bilayer (thermometers are available under the hood). At that time, a stirrer should also be placed in the beaker and the RPM set to 200-250 RPM. Now the clamping device can be lowered into the KOH beaker by means of plastic hooks that attach to the TEFLON tabs on the device. The temperature can then be increased to about 98°C to speed-up the etching. After a few minutes, hydrogen bubbles will start to be released as aresult of the etching reaction. These are aparticularly visible when etching a whole wafer, but are more difficult to see with a chip. In fact, when etching chips, I recommend using a glass rod to periodically clear the bubble that tends to get trapped on the back of the clamping device, in order to ensure that fresh KOH reaches the surface.

Ending the etch

When the estimated etch time is up (including overetching to obtain a residue-free window), pull the clamping device out using the hooks and place it in a

147

second beaker that is filled with warm DI water. After about a minute, take it out and rinse it with warm water in the base hood sink. The warm water is intended to reduce the thermal shock on the windows. It is also important to use light water pressure when rinsing and to point the jet at an angle to reduce the risk of breaking windows. I found that the windows are actually quite robust and will not break if using this method.

Inspecting the result of the etch

At this point, the clamping device is well rinsed, so it is possible to take it to a hood in the e-beam resist spinning room (or photolithography spinning room). Here, the screws are removed and the chip or wafer is quickly rinsed with water and blow-dried. In the case of the wafer, the depth of the etches can be verified with a profilometer. For chips, it is necessary to use a microscope to see if the windows are fully-etched, clean and sufficiently well-aligned to overlap with the nanopillars. If all looks fine, then the PROTEK can be removed in acetone, followed by an isopropyl alcohol (IPA) rinse, and blow-drying. If, on the other hand, the windows need further etching, then the chip can be put back in the clamping device and then in the KOH bath, as before. (However, if the PRO-TEK is in bad shape, it is better to strip it in acetone, and then spin a new bilayer before continuing the etch. Otherwise, if KOH seeps under the PROTEK, the latter will leave a residue that cannot be removed with acetone. Even if the seeped KOH does not damage the metallic features, this residue can still degrade the quality of the electrical contact to the pads or enhance x-ray attenuation.)

E.4 Fab sheet for the suspended pillar process

page 1/3	🕐	date:	Wafer:
Substrate Si[100] + Si3N4			Si3N4 thickness =
1.Sputter Wafer			
2.Pre-clean wafer			
3.Evaporate Carbon (500Å) (800Å for vortex nanopillars)			
4.Spin PMMA bilayer			
5.VB6 expose on Carbon			job file:
(5*5 dies)			devices per die =
6.Develop PMMA			
7.Evaporate Cr Mask (150Å) (200Å for vortex nanopillars)			
8.Liftoff Cr Mask			
9.RIE Carbon in O2 plasma			Etch time =
10.Spin Photoresist			
11.Photolith Step #1			
"Define Leads" (step1cm in x&y)			
12.Develop			
13.Descum			
14.Ion Mill (1)			Mill time =
(T = -10.0 ºC, ø = 45º, 60 mA)			After IM 1 & 2,
			SiN should still have ~ 100 nm left.
15.Strip resist			
16. Measure Depth of Etches			(1,1) die =
			(3,3) die =
			SiN thickness =
17.Spin Photoresist (Spinmob 2)			
18.Photolith Step #2			
"Define Pillar"			
19.Develop			
20.Descum			
21.Ion Mill (2)			Mill time =
(T = -10.0 ºC, ø = 45º, 60 mA)			
22.Strip resist			
23.Measure Depth of Etches			(1,1) die =
			(3,3) die =
			SiN thickness =
24.PECVD Si3N4 at 170˚C			*Can do two 3" wafers, flat-to-flat
Use program #2 in IPE PECVD manual			**Aim for 4 x pillar height
			One calibration wafer. Rate = about 18 nm/min
			Dep time =
25.Ion Mill (3) Planarization			*Shutter open continuously
(ø = 85º, find with level)			Etch rate calibration using FilMetrics
			Etch rate =
			Etch time =
26.AFM for Planarization			(1,1) die =
			(3,3) die =
27.Spin Photoresist (w/ P-20)			
28.Photolith Step #3 "Si3N4 Etch"			
29.Develop			
30.Descum			

Figure E.5: Fab sheet for the suspended nanopillar process - page 1.

page 2/3	🕐	date:	**Wafer:**
31.CHF3 + O2 Etch Si3N4			Time =
on bonding pads			
32.Strip resist, measure nitride			(1,1) die =
			(3,3) die =
33.Spin Photoresist (w/ P-20)			
34.Photolith Step #4			
"Protect Shorts"			
35.Develop			
36.Descum			
37.Evaporate Si3N4 as needed			
Use even hour evaporator.			
38.Liftoff and measure Si3N4			use wafer map
above pillar			
39.Spin Photoresist (w/ P-20)			
40.Photolith Step #5			*Only necessary if nitride
"Etch Si3N4 above pillar"			depth is >80nm
41.Develop			
42.Descum			
43.Ion Mill (4)			*Ion Mill to 50nm above pillar
(ø = 25º, 40 mA)			
44.Strip resist			
45.Measure Depth of Etch			use wafer map
46.Spin Photoresist on backside			
(w/ P-20)			
47.Photolith on EV620			
Backside alignment exp time 12s			
48.Develop			
49.Descum			
50.CHF3 + O2 Etch Si3N4 window			
51.Spin Protek			
(Primer + three-step baking)			
52.KOH etch			
			Etch time =
			KOH temperature =
			Depth of Etch = (Profilometer)
53.Strip PROTEK			
54.Spin Photoresist (S1813 w/ P-20)			
55.Photolith Step #6			
"Top Leads"			
56.Develop			
57.Descum			
58.Ion Mill (5)			*Aim for top of Pt layer
(ø = 25º, 40 mA)			
59.O2 etch C mask			*3 x time in step 9.
60.Ion Mill (6) for 6-15 sec			Mill time =
(T = +20.0 ºC, ø = 0º)			
61.Sputter or IBD Cu			*Sputter 2000Å or IBD 3000Å
62.Spin PROTEK on individual chip			
63.KOH etch			
64.Strip PROTEK and inspect			

Figure E.6: Fab sheet for the suspended nanopillar process - page 2.

END OF FAB SHEET STEPS

Recipe for Si3N4 plasma etch in PT72:
CHF3: 30 SCCM
O2: 0.7 SCCM
Pressure: 30 mTorr
RF power: 150 W
Rate: ~35 nm/min

Figure E.7: Fab sheet for the suspended nanopillar process - page 3.

151

BIBLIOGRAPHY

[1] Žutiç, I., Fabian, J. & Sarma, S.D., Spintronics: Fundamentals and applications, *Reviews of Modern Physics* **76**, 323 (2004).

[2] DiVincenzo, D.P., Quantum Computation, *Science* **270**, 255–261 (1995).

[3] Loss, D. & DiVincenzo, D.P., Quantum computation with quantum dots, *Phys. Rev. A* **57**, 120 (1998).

[4] O'Handley, R., *Modern magnetic materials: principles and applications*, Wiley, New York (2000).

[5] Tsymbal, E.Y. & D., G.P., Perspectives of Giant Magnetoresistance, in *Solid State Physics* (H. Ehrenreich & F. Spaepen, eds.), Academic Press, 111–237 (2001).

[6] Nickel, J., Magnetoresistance Overview, Tech. Rep. HPL-95-60, HP (1995).

[7] Chappert, C., Fert, A. & Dau, F.N.V., The emergence of spin electronics in data storage, *Nat. Mater.* **6**, 813–823 (2007).

[8] van Gorkom, R.P., Caro, J., Klapwijk, T.M. & Radelaar, S., Temperature and angular dependence of the anisotropic magnetoresistance in epitaxial Fe films, *Phys. Rev. B* **63**, 134432 (2001).

[9] Baibich, M.N., Broto, J.M., Fert, A., Dau, F.N.V., Petroff, F., Etienne, P., Creuzet, G., Friederich, A. & Chazelas, J., Giant Magnetoresistance of (001)Fe/(001)Cr Magnetic Superlattices, *Phys. Rev. Lett.* **61**, 2472 (1988).

[10] Binasch, G., Grünberg, P., Saurenbach, F. & Zinn, W., Enhanced magnetoresistance in layered magnetic structures with antiferromagnetic interlayer exchange, *Phys. Rev. B* **39**, 4828–4830 (1989).

[11] Jullière, M., Tunneling between ferromagnetic films, *Phys. Lett. A* **54**, 225–226 (1975).

[12] Moodera, J.S., Kinder, L.R., Wong, T.M. & Meservey, R., Large Magnetoresistance at Room Temperature in Ferromagnetic Thin Film Tunnel Junctions, *Phys. Rev. Lett.* **74**, 3273–3276 (1995).

[13] Miyazaki, T. & Tezuka, N., Giant magnetic tunneling effect in Fe/Al2O3/Fe junction, *J. Magn. Magn. Mat.* **139**, L231–L234 (1995).

[14] Lee, Y.M., Hayakawa, J., Ikeda, S., Matsukura, F. & Ohno, H., Effect of electrode composition on the tunnel magnetoresistance of pseudo-spin-valve magnetic tunnel junction with a MgO tunnel barrier, *Appl. Phys. Lett.* **90**, 212507 (2007).

[15] Ramirez, A.P., Colossal Magnetoresistance, *JOP: Cond. Matt.* **9**, 8171 (1997).

[16] Grünberg, P., Schreiber, R., Pang, Y., Brodsky, M.B. & Sowers, H., Layered Magnetic Structures: Evidence for Antiferromagnetic Coupling of Fe Layers across Cr Interlayers, *Phys. Rev. Lett.* **57**, 2442–2445 (1986).

[17] Majkrzak, C.F., Cable, J.W., Kwo, J., Hong, M., McWhan, D.B., Yafet, Y., Waszczak, J.V. & Vettier, C., Observation of a Magnetic Antiphase Domain Structure with Long-Range Order in a Synthetic Gd-Y Superlattice, *Phys. Rev. Lett.* **56**, 2700–2703 (1986).

[18] Salamon, M.B., Sinha, S., Rhyne, J.J., Cunningham, J.E., Erwin, R.W., Borchers, J. & Flynn, C.P., Long-range incommensurate magnetic order in a Dy-Y multilayer, *Phys. Rev. Lett.* **56**, 259–262 (1986).

[19] Parkin, S.S.P., Bhadra, R. & Roche, K.P., Oscillatory magnetic exchange coupling through thin copper layers, *Phys. Rev. Lett.* **66**, 2152–2155 (1991).

[20] Ralph, D.C. & Stiles, M.D., Spin Transfer Torques, *J. Magn. Magn. Mat.* **320**, 1190 (2007).

[21] Dieny, B., Speriosu, V.S., Parkin, S.S.P., Gurney, B.A., Wilhoit, D.R. & Mauri, D., Giant magnetoresistive in soft ferromagnetic multilayers, *Phys. Rev. B* **43**, 1297–1300 (1991).

[22] Steren, L., Morel, R., Barthlmy, A., Petroff, F., Fert, A., Holody, P., Loloee, R. & Schroeder, P., Giant magnetoresistance in hybrid magnetic nanostructures, *J. Magn. Magn. Mat.* **140**, 495 – 496 (1995), international Conference on Magnetism.

[23] Piraux, L., George, J.M., Despres, J.F., Leroy, C., Ferain, E., Legras, R., Ounadjela, K. & Fert, A., Giant magnetoresistance in magnetic multilayered nanowires, *Appl. Phys. Lett.* **65**, 2484 (1994).

[24] Mott, N.F., The Electrical Conductivity of Transition Metals, *Proc. R. Soc. Lond. A* **153**, 699–717 (1936).

[25] Valet, T. & Fert, A., Theory of the perpendicular magnetoresistance in magnetic multilayers, *Phys. Rev. B* **48**, 7099–7113 (1993).

[26] Johnson, M. & Silsbee, R.H., Interfacial charge-spin coupling: Injection and detection of spin magnetization in metals, *Phys. Rev. Lett.* **55**, 1790–1793 (1985).

[27] Johnson, M. & Silsbee, R.H., Coupling of electronic charge and spin at a ferromagnetic-paramagnetic metal interface, *Phys. Rev. B* **37**, 5312–5325 (1988).

[28] Zhang, S. & Levy, P.M., Conductivity perpendicular to the plane of multi-layered structures, *J. Appl. Phys.* **69**, 4786–4788 (1991).

[29] Camblong, H.E., Zhang, S. & Levy, P.M., Magnetoresistance of multilayered structures for currents perpendicular to the plane of the layers, *Phys. Rev. B* **47**, 4735–4741 (1993).

[30] Schmidt, G., Ferrand, D., Molenkamp, L.W., Filip, A.T. & van Wees, B.J., Fundamental obstacle for electrical spin injection from a ferromagnetic metal into a diffusive semiconductor, *Phys. Rev. B* **62**, R4790–R4793 (2000).

[31] Rashba, E.I., Theory of electrical spin injection: Tunnel contacts as a solution of the conductivity mismatch problem, *Phys. Rev. B* **62**, R16267–R16270 (2000).

[32] Fert, A. & Jaffrès, H., Conditions for efficient spin injection from a ferromagnetic metal into a semiconductor, *Phys. Rev. B* **64**, 184420 (2001).

[33] Jiang, X., Wang, R., Shelby, R.M., Macfarlane, R.M., Bank, S.R., Harris, J.S. & Parkin, S.S.P., Highly Spin-Polarized Room-Temperature Tunnel Injector for Semiconductor Spintronics using MgO(100), *Phys. Rev. Lett.* **94**, 056601 (2005).

[34] Crooker, S.A., Furis, M., Lou, X., Adelmann, C., Smith, D.L., Palmstrom, C.J. & Crowell, P.A., Imaging Spin Transport in Lateral Ferromagnet/Semiconductor Structures, *Science* **309**, 2191–2195 (2005).

[35] Schuhl, A. & Lacour, D., Spin dependent transport: GMR & TMR, *Comptes Rendus Physique* **6**, 945–955 (2005).

[36] Teresa, J.M.D., Barthélémy, A., Fert, A., Contour, J.P., Montaigne, F. & Seneor, P., Role of Metal-Oxide Interface in Determining the Spin Polarization of Magnetic Tunnel Junctions, *Science* **286**, 507–509 (1999).

[37] Zhang, X.G. & Butler, W.H., Large magnetoresistance in bcc Co/MgO/Co and FeCo/MgO/FeCo tunnel junctions, *Phys. Rev. B* **70**, 172407 (2004).

[38] Berger, L., Prediction of a domain-drag effect in uniaxial, non-compensated, ferromagnetic metals, *J. Phys. Chem. Solids* **35**, 947–956 (1974).

[39] Freitas, P. & Berger, L., Observation of sd exchange force between domain walls and electric current in very thin Permalloy films, *J. Appl. Phys.* **57**, 1266–1269 (1985).

[40] Slonczewski, J.C., Current-driven excitation of magnetic multilayers., *J. Magn. Magn. Mat.* **159**, L1–L7 (1996).

[41] Berger, L., Emission of spin waves by a magnetic multilayer traversed by a current., *Phys. Rev. B* **54**, 9353–9358 (1996).

[42] Slonczewski, J., United States Patent #5,695,864 (1997).

[43] Myers, E.B., Ralph, D.C., Katine, J.A., Louie, R.N. & Buhrman, R.A., Current-Induced Switching of Domains in Magnetic Multilayer Devices, *Science* **285**, 867–870 (1999).

[44] Katine, J.A., Albert, F.J., Buhrman, R.A., Myers, E.B. & Ralph, D.C., Current-Driven Magnetization Reversal and Spin-Wave Excitations in Co /Cu /Co Pillars, *Phys. Rev. Lett.* **84**, 3149–3152 (2000).

[45] Kiselev, S.I., Sankey, J.C., Krivorotov, I.N., Emley, N.C., Schoelkopf, R.J., Buhrman, R.A. & Ralph, D.C., Microwave oscillations of a nanomagnet driven by a spin-polarized current, *Nature* **425**, 380–383 (2003).

[46] Sun, J. & Ralph, D., Magnetoresistance and spin-transfer torque in magnetic tunnel junctions, *J. Magn. Magn. Mater.* **320**, 1227–1237 (2008).

[47] Polianski, M.L. & Brouwer, P.W., Current-Induced Transverse Spin-Wave Instability in a Thin Nanomagnet, *Phys. Rev. Lett.* **92**, 026602 (2004).

[48] Özyilmaz, B., Kent, A.D., Sun, J.Z., Rooks, M.J. & Koch, R.H., Current-Induced Excitations in Single Cobalt Ferromagnetic Layer Nanopillars, *Phys. Rev. Lett.* **93**, 176604 (2004).

[49] Özyilmaz, B. & Kent, A.D., Current-induced switching in single ferroma-genetic layer nanopillar junctions, *Appl. Phys. Lett.* **88**, 162506 (2006).

[50] Xiao, J., Zangwill, A. & Stiles, M.D., Boltzmann test of Slonczewski's the-ory of spin-transfer torque, *Phys. Rev. B* **70**, 172405 (2004).

[51] McMichael, R.D., Twisselmann, D.J. & Kunz, A., Localized Ferromag-netic Resonance in Inhomogeneous Thin Films, *Phys. Rev. Lett.* **90**, 227601 (2003).

[52] Tserkovnyak, Y., Brataas, A. & Bauer, G.E.W., Enhanced Gilbert Damping in Thin Ferromagnetic Films, *Phys. Rev. Lett.* **88**, 117601 (2002).

[53] Kamberský, V., *Czech. J. Phys. Section B* **26**, 1366 (1976).

[54] Gilmore, K., Idzerda, Y.U. & Stiles, M.D., Identification of the Dominant Precession-Damping Mechanism in Fe, Co, and Ni by First-Principles Cal-culations, *Phys. Rev. Lett.* **99**, 027204 (2007).

[55] Sinova, J., Jungwirth, T., Liu, X., Sasaki, Y., Furdyna, J.K., Atkinson, W.A. & MacDonald, A.H., Magnetization relaxation in (Ga,Mn)As ferromag-netic semiconductors, *Phys. Rev. B* **69**, 085209 (2004).

[56] Krivorotov, I.N., Emley, N.C., Garcia, A.G.F., Sankey, J.C., Kiselev, S.I., Ralph, D.C. & Buhrman, R.A., Temperature Dependence of Spin-Transfer-Induced Switching of Nanomagnets, *Phys. Rev. Lett.* **93**, 166603 (2004).

[57] Liu, L., Moriyama, T., Ralph, D.C. & Buhrman, R.A., Reduction of the spin-torque critical current by partially canceling the free layer demagne-tization field, *Appl. Phys. Lett.* **94**, 122508 (2009).

[58] Lee, O.J., Pribiag, V.S., Braganca, P.M., Gowtham, P.G., Ralph, D.C. & Buhrman, R.A., Ultrafast switching of a nanomagnet by a combined out-of-plane and in-plane polarized spin current pulse, *Appl. Phys. Lett.* **95**, 012506 (2009).

[59] Rippard, W.H., Pufall, M.R., Kaka, S., Russek, S.E. & Silva, T.J., Direct-Current Induced Dynamics in $Co90Fe10/Ni80Fe20$ Point Contacts, *Phys. Rev. Lett.* **92**, 027201 (2004).

[60] Krivorotov, I.N., Emley, N.C., Sankey, J.C., Kiselev, S.I., Ralph, D.C. & Buhrman, R.A., Time-Domain Measurements of Nanomagnet Dynamics Driven by Spin-Transfer Torques, *Science* **307**, 228–231 (2005).

[61] Pribiag, V.S., Krivorotov, I.N., Fuchs, G.D., Braganca, P.M., Ozatay, O., Sankey, J.C., Ralph, D.C. & Buhrman, R.A., Magnetic vortex oscillator driven by d.c. spin-polarized current, *Nat. Phys.* **3**, 498–503 (2007).

[62] Kittel, C., *Introduction to Solid State Physics*, John Wiley & Sons, New York, 7th edn. (1996).

[63] Slavin, A. & Tiberkevich, V., Nonlinear Auto-Oscillator Theory of Microwave Generation by Spin-Polarized Current, *IEEE Trans. Mag.* **45**, 1875 –1918 (2009).

[64] Sankey, J.C., Braganca, P.M., Garcia, A.G.F., Krivorotov, I.N., Buhrman, R.A. & Ralph, D.C., Spin-Transfer-Driven Ferromagnetic Resonance of Individual Nanomagnets, *Phys. Rev. Lett.* **96**, 227601 (2006).

[65] Bland, J.A.C. & Heinrich, B., *Ultrathin Magnetic Structures III*, Springer (2005).

[66] Lax, M., Classical Noise. V. Noise in Self-Sustained Oscillators, *Phys. Rev.* **160**, 290–307 (1967).

[67] Sankey, J.C., Krivorotov, I.N., Kiselev, S.I., Braganca, P.M., Emley, N.C., Buhrman, R.A. & Ralph, D.C., Mechanisms limiting the coherence time of spontaneous magnetic oscillations driven by dc spin-polarized currents, *Phys. Rev. B* **72**, 224427 (2005).

[68] Lee, K., Deac, A., Redon, O., Nozieres, J. & Dieny, B., Excitations of incoherent spin-waves due to spin-transfer torque, *Nat. Mater.* **3**, 877–881 (2004).

[69] Berkov, D. & Gorn, N., Transition from the macrospin to chaotic behavior by a spin-torque driven magnetization precession of a square nanoelement, *Phys. Rev. B* **71**, 052403 (2005).

[70] Boone, C., Katine, J.A., Childress, J.R., Zhu, J., Cheng, X. & Krivorotov, I.N., Experimental test of an analytical theory of spin-torque-oscillator dynamics, *Phys. Rev. B* **79**, 140404 (2009).

[71] Rippard, W.H., Pufall, M.R., Kaka, S., Silva, T.J. & Russek, S.E., Current-driven microwave dynamics in magnetic point contacts as a function of applied field angle, *Phys. Rev. B* **70**, 100406 (2004).

[72] Pufall, M.R., Rippard, W.H., Schneider, M.L. & Russek, S.E., Low-field current-hysteretic oscillations in spin-transfer nanocontacts, *Phys. Rev. B* **75**, 140404 (2007).

[73] Houssameddine, D., Florez, S.H., Katine, J.A., Michel, J.P., Ebels, U., Mauri, D., Ozatay, O., Delaet, B., Viala, B., Folks, L., Terris, B.D. & Cyrille, M.C., Spin transfer induced coherent microwave emission with large power from nanoscale MgO tunnel junctions, *Appl. Phys. Lett.* **93**, 022505 (2008).

[74] Deac, A.M., Fukushima, A., Kubota, H., Maehara, H., Suzuki, Y., Yuasa, S., Nagamine, Y., Tsunekawa, K., Djayaprawira, D.D. & Watanabe, N., Bias-driven high-power microwave emission from MgO-based tunnel magnetoresistance devices, *Nat Phys* **4**, 803–809 (2008).

[75] Dussaux, A., Georges, B., Grollier, J., Cros, V., Khvalkovskiy, A., Fukushima, A., Konoto, M., Kubota, H., Yakushiji, K., Yuasa, S., Zvezdin, K., Ando, K. & Fert, A., Large microwave generation from current-driven magnetic vortex oscillators in magnetic tunnel junctions, *Nat. Commun.* **1**, 1–6 (2010).

[76] Mancoff, F.B., Rizzo, N.D., Engel, B.N. & Tehrani, S., Phase-locking in double-point-contact spin-transfer devices, *Nature* **437**, 393–395 (2005).

[77] Kaka, S., Pufall, M.R., Rippard, W.H., Silva, T.J., Russek, S.E. & Katine, J.A., Mutual phase-locking of microwave spin torque nano-oscillators, *Nature* **437**, 389–392 (2005).

[78] RuotoloA., CrosV., GeorgesB., DussauxA., GrollierJ., DeranlotC., GuillemetR., BouzehouaneK., FusilS. & FertA., Phase-locking of magnetic vortices mediated by antivortices, *Nat Nano* **4**, 528–532 (2009).

[79] Grollier, J., Cros, V. & Fert, A., Synchronization of spin-transfer oscillators driven by stimulated microwave currents, *Physical Review B* **73**, 060409 (2006).

[80] Beach, G., Tsoi, M. & Erskine, J., Current-induced domain wall motion, *J. Magn. Magn. Mat.* **320**, 1272–1281 (2008).

[81] Ohno, H. & Dietl, T., Spin-transfer physics and the model of ferromagnetism in (Ga,Mn)As, *J. Magn. Magn. Mat.* **320**, 1293–1299 (2008).

[82] Shinjo, T., Okuno, T., Hassdorf, R., Shigeto, K. & Ono, T., Magnetic Vortex Core Observation in Circular Dots of Permalloy, *Science* **289**, 930–932 (2000).

[83] Usov, N.A. & Peschany, S.E., Magnetization curling in a fine cylindrical particle, *J. Magn. Magn. Mater.* **118**, L290 – L294 (1993).

[84] Metlov, K.L. & Guslienko, K.Y., Stability of magnetic vortex in soft magnetic nano-sized circular cylinder, *J. Magn. Magn. Mater.* **242-245**, 1015 – 1017 (2002).

[85] Cowburn, R.P., Koltsov, D.K., Adeyeye, A.O., Welland, M.E. & Tricker, D.M., Single-Domain Circular Nanomagnets, *Phys. Rev. Lett.* **83**, 1042–1045 (1999).

[86] Antos, R., Otani, Y. & Shibata, J., Magnetic Vortex Dynamics, *J. Phys. Soc. Jpn.* **77**, 031004 (2008).

[87] Argyle, B.E., Terrenzio, E. & Slonczewski, J.C., Magnetic Vortex Dynamics Using the Optical Cotton-Mouton Effect, *Phys. Rev. Lett.* **53**, 190 (1984).

[88] Park, J.P., Eames, P., Engebretson, D.M., Berezovsky, J. & Crowell, P.A., Imaging of spin dynamics in closure domain and vortex structures, *Phys. Rev. B* **67**, 020403 (2003).

[89] Thiele, A.A., Steady-State Motion of Magnetic Domains, *Phys. Rev. Lett.* **30**, 230–233 (1973).

[90] Buchanan, K.S., Roy, P.E., Grimsditch, M., Fradin, F.Y., Guslienko, K.Y., Bader, S.D. & Novosad, V., Magnetic-field tunability of the vortex translational mode in micron-sized permalloy ellipses: Experiment and micromagnetic modeling, *Phys. Rev. B* **74**, 064404 (2006).

[91] Huber, D.L., Dynamics of spin vortices in two-dimensional planar magnets, *Phys. Rev. B* **26**, 3758–3765 (1982).

[92] Hikami, S. & Tsuneto, T., Phase Transition of Quasi-Two Dimensional Planar System, *Prog. Theor. Phys.* **63**, 387–401 (1980).

[93] Guslienko, K.Y., Novosad, V., Otani, Y., Shima, H. & Fukamichi, K., Field evolution of magnetic vortex state in ferromagnetic disks, *Appl. Phys. Lett.* **78**, 3848–3850 (2001).

[94] Guslienko, K.Y., Ivanov, B.A., Novosad, V., Otani, Y., Shima, H. & Fukamichi, K., Eigenfrequencies of vortex state excitations in magnetic submicron-size disks, *J. Appl. Phys.* **91**, 8037–8039 (2002).

[95] Novosad, V., Fradin, F.Y., Roy, P.E., Buchanan, K.S., Guslienko, K.Y. & Bader, S.D., Magnetic vortex resonance in patterned ferromagnetic dots, *Phys. Rev. B* **72**, 024455 (2005).

[96] Guslienko, K.Y., Aranda, G.R. & Gonzalez, J.M., Spin torque and critical currents for magnetic vortex nano-oscillator in nanopillars, *arXiv:0912.5521v1 [cond-mat.other]* (2009).

[97] Park, J.P. & Crowell, P.A., Interactions of Spin Waves with a Magnetic Vortex, *Phys. Rev. Lett.* **95**, 167201 (2005).

[98] Back, C., Pescia, D. & Buess, M., Vortex Dynamics, in *Spin Dynamics in Confined Magnetic Structures III*, Springer, Berlin / Heidelberg, 137–160 (2006).

[99] Acremann, Y., Back, C.H., Buess, M., Portmann, O., Vaterlaus, A., Pescia, D. & Melchior, H., Imaging Precessional Motion of the Magnetization Vector, *Science* **290**, 492–495 (2000).

[100] Zhu, X., Malac, M., Liu, Z., Qian, H., Metlushko, V. & Freeman, M.R., Broadband spin dynamics of Permalloy rings in the circulation state, *Appl. Phys. Lett.* **86**, 262502 (2005).

[101] Buess, M., Höllinger, R., Haug, T., Perzlmaier, K., Krey, U., Pescia, D., Scheinfein, M.R., Weiss, D. & Back, C.H., Fourier Transform Imaging of Spin Vortex Eigenmodes, *Phys. Rev. Lett.* **93**, 077207 (2004).

[102] Ivanov, B.A., Schnitzer, H.J., Mertens, F.G. & Wysin, G.M., Magnon modes and magnon-vortex scattering in two-dimensional easy-plane ferromagnets, *Phys. Rev. B* **58**, 8464–8474 (1998).

[103] Ivanov, B.A. & Zaspel, C.E., Magnon modes for thin circular vortex-state magnetic dots, *Appl. Phys. Lett.* **81**, 1261–1263 (2002).

[104] Guslienko, K.Y., Scholz, W., Chantrell, R.W. & Novosad, V., Vortex-state oscillations in soft magnetic cylindrical dots, *Phys. Rev. B* **71**, 144407 (2005).

[105] Shibata, J., Nakatani, Y., Tatara, G., Kohno, H. & Otani, Y., Current-induced magnetic vortex motion by spin-transfer torque, *Phys. Rev. B* **73**, 020403(R) (2006).

[106] Kasai, S., Nakatani, Y., Kobayashi, K., Kohno, H. & Ono, T., Current-Driven Resonant Excitation of Magnetic Vortices, *Phys. Rev. Lett.* **97**, 107204 (2006).

[107] Pribiag, V.S., Krivorotov, I.N., Fuchs, G.D., Braganca, P.M., Ozatay, O., Sankey, J.C., Ralph, D.C. & Buhrman, R.A., Magnetic vortex oscillator driven by dc spin-polarized current, *cond-mat/0702253* (2007).

[108] Pufall, M.R., Rippard, W.H., Schneider, M. & Russek, S.E., Low Field, Current-Hysteretic Oscillations in Spin Transfer Nanocontacts, *cond-mat/0702416* (2007).

[109] Mistral, Q., van Kampen, M., Hrkac, G., Kim, J.V., Devolder, T., Crozat, P., Chappert, C., Lagae, L. & Schrefl, T., Current-Driven Vortex Oscillations in Metallic Nanocontacts, *Phys. Rev. Lett.* **100**, 257201 (2008).

[110] Khvalkovskiy, A.V., Grollier, J., Locatelli, N., Gorbunov, Y.V., Zvezdin, K.A. & Cros, V., Nonuniformity of a planar polarizer for spin-transfer-induced vortex oscillations at zero field, *Appl. Phys. Lett.* **96**, 212507 (2010).

[111] Khvalkovskiy, A.V., Grollier, J., Dussaux, A., Zvezdin, K.A. & Cros, V., Vortex oscillations induced by spin-polarized current in a magnetic nanopillar: Analytical versus micromagnetic calculations, *Phys. Rev. B* **80**, 140401 (2009).

[112] Yamada, K., Kasai, S., Nakatani, Y., Kobayashi, K., Kohno, H., Thiaville, A. & Ono, T., Electrical switching of the vortex core in a magnetic disk, *Nat. Mater.* **6**, 270–273 (2007).

[113] Caputo, J.G., Gaididei, Y., Mertens, F.G. & Sheka, D.D., Vortex Polarity Switching by a Spin-Polarized Current, *Phys. Rev. Lett.* **98**, 056604 (2007).

[114] Liu, Y., He, H. & Zhang, Z., Spin-torque-driven vortex dynamics in a spin-valve pillar with a perpendicular polarizer, *Appl. Phys. Lett.* **91**, 242501 (2007).

[115] Choi, B.C., Rudge, J., Girgis, E., Kolthammer, J., Hong, Y.K. & Lyle, A., Spin-current pulse induced switching of vortex chirality in permalloy/Cu/Co nanopillars, *Appl. Phys. Lett.* **91**, 022501 (2007).

[116] Acremann, Y., Strachan, J.P., Chembrolu, V., Andrews, S.D., Tyliszczak, T., Katine, J.A., Carey, M.J., Clemens, B.M., Siegmann, H.C. & Stöhr, J., Time-Resolved Imaging of Spin Transfer Switching: Beyond the Macrospin Concept, *Phys. Rev. Lett.* **96**, 217202 (2006).

[117] Wachowiak, A., Wiebe, J., Bode, M., Pietzsch, O., Morgenstern, M. & Wiesendanger, R., Direct Observation of Internal Spin Structure of Magnetic Vortex Cores, *Science* **298**, 577–580 (2002).

[118] Choe, S., Acremann, Y., Scholl, A., Bauer, A., Doran, A., Stöhr, J. & Padmore, H.A., Vortex Core-Driven Magnetization Dynamics, *Science* **304**, 420–422 (2004).

[119] Waeyenberge, B.V., Puzic, A., Stoll, H., Chou, K.W., Tyliszczak, T., Hertel, R., Fahnle, M., Bruckl, H., Rott, K., Reiss, G., Neudecker, I., Weiss, D., Back, C.H. & Schutz, G., Magnetic vortex core reversal by excitation with short bursts of an alternating field, *Nature* **444**, 461–464 (2006).

[120] Bode, M., Wachowiak, A., Wiebe, J., Kubetzka, A., Morgenstern, M. & Wiesendanger, R., Thickness dependent magnetization states of Fe islands on W(110): From single domain to vortex and diamond patterns, *Appl. Phys. Lett.* **84**, 948–950 (2004).

[121] Donahue, M.J. & Porter, D.G., OOMMF User's Guide, Version 1.0. Interagency Report NISTR 6376, Tech. Rep., National Institute of Standards and Technology, Gaithersburg, MD (1999).

[122] Rahm, M., Biberger, J., Umansky, V. & Weiss, D., Vortex pinning at individual defects in magnetic nanodisks, *J. of Appl. Phys.* **93**, 7429–7431 (2003).

[123] Uhlig, T., Rahm, M., Dietrich, C., Höllinger, R., Heumann, M., Weiss, D. & Zweck, J., Shifting and Pinning of a Magnetic Vortex Core in a Permalloy Dot by a Magnetic Field, *Phys. Rev. Lett.* **95**, 237205 (2005).

[124] Tsoi, M., Jansen, A.G.M., Bass, J., Chiang, W.C., Seck, M., Tsoi, V. & Wyder, P., Excitation of a Magnetic Multilayer by an Electric Current, *Phys. Rev. Lett.* **80**, 4281–4284 (1998).

[125] Emley, N.C., Krivorotov, I.N., Ozatay, O., Garcia, A.G.F, Sankey, J.C., Ralph, D.C. & Buhrman, R.A., Time-Resolved Spin-Torque Switching and Enhanced Damping in Permalloy/Cu/Permalloy Spin-Valve Nanopillars, *Phys. Rev. Lett.* **96**, 247204 (2006).

[126] Compton, R.L. & Crowell, P.A., Dynamics of a Pinned Magnetic Vortex, *Phys. Rev. Lett.* **97**, 137202 (2006).

[127] Kiselev, S.I., Sankey, J.C., Krivorotov, I.N., Emley, N.C., Garcia, A.G.F., Buhrman, R.A. & Ralph, D.C., Spin-transfer excitations of permalloy nanopillars for large applied currents, *Phys. Rev. B* **72**, 064430 (2005).

[128] Kim, J.V., Stochastic theory of spin-transfer oscillator linewidths, *Phys. Rev. B* **73**, 174412 (2006).

[129] Finocchio, G., Krivorotov, I.N., Torres, L., Buhrman, R.A., Ralph, D.C. & Azzerboni, B., Magnetization reversal driven by spin-polarized current in exchange-biased nanoscale spin valves, *Phys. Rev. B* **76**, 174408 (2007).

[130] Siracusano, G., Finocchio, G., Krivorotov, I.N., Torres, L., Consolo, G. & Azzerboni, B., Micromagnetic simulations of persistent oscillatory modes excited by spin-polarized current in nanoscale exchange-biased spin valves, *J. Appl. Phys.* **105**, 07D107 (2009).

[131] Bass, J. & Pratt, W.P., Current-perpendicular (CPP) magnetoresistance in magnetic metallic multilayers, *J. Magn. Magn. Mater.* **200**, 274 – 289 (1999).

[132] Consolo, G., Lopez-Diaz, L., Torres, L., Finocchio, G., Romeo, A. & Azzerboni, B., Nanocontact spin-transfer oscillators based on perpendicular anisotropy in the free layer, *Appl. Phys. Lett.* **91**, 162506 (2007).

[133] Pribiag, V.S., Finocchio, G., Williams, B.J., Ralph, D.C. & Buhrman, R.A., Long-timescale fluctuations in zero-field magnetic vortex oscillations driven by dc spin-polarized current, *Phys. Rev. B* **80**, 180411(R) (2009).

[134] Brown, W.F., Thermal Fluctuations of a Single-Domain Particle, *Phys. Rev.* **130**, 1677–1686 (1963).

[135] Li, Z. & Zhang, S., Thermally assisted magnetization reversal in the presence of a spin-transfer torque, *Phys. Rev. B* **69**, 134416 (2004).

[136] Finocchio, G., Carpentieri, M., Azzerboni, B., Torres, L., Martinez, E. & Lopez-Diaz, L., Micromagnetic simulations of nanosecond magnetization reversal processes in magnetic nanopillar, *J. Appl. Phys.* **99**, 08G522 (2006).

[137] McMichael, R.D. & Stiles, M.D., Magnetic normal modes of nanoelements, *J. Appl. Phys.* **97**, 10J901 (2005).

[138] Torres, L., Lopez-Diaz, L., Martinez, E., Finocchio, G., Carpentieri, M. & Azzerboni, B., Coupling of spin-transfer torque to microwave magnetic field: A micromagnetic modal analysis, *J. Appl. Phys.* **101**, 053914 (2007).

[139] Krivorotov, I.N., Berkov, D.V., Gorn, N.L., Emley, N.C., Sankey, J.C., Ralph, D.C. & Buhrman, R.A., Large-amplitude coherent spin waves excited by spin-polarized current in nanoscale spin valves, *Phys. Rev. B* **76**, 024418 (2007).

[140] Soulen, R.J., Byers, J.M., Osofsky, M.S., Nadgorny, B., Ambrose, T., Cheng, S.F., Broussard, P.R., Tanaka, C.T., Nowak, J., Moodera, J.S., Barry, A. & Coey, J.M.D., Measuring the Spin Polarization of a Metal with a Superconducting Point Contact, *Science* **282**, 85–88 (1998).

[141] Boulle, O., Cros, V., Grollier, J., Pereira, L.G., Deranlot, C., Petroff, F., Faini, G., Barnas, J. & Fert, A., Shaped angular dependence of the spin-transfer torque and microwave generation without magnetic field, *Nat. Phys.* **3**, 492–497 (2007).

[142] Lehndorff, R., Bürgler, D.E., Gliga, S., Hertel, R., Grünberg, P., Schneider, C.M. & Celinski, Z., Magnetization dynamics in spin torque nano-oscillators: Vortex state versus uniform state, *Phys. Rev. B* **80**, 054412 (2009).

[143] Ivanov, B.A. & Zaspel, C.E., Excitation of Spin Dynamics by Spin-Polarized Current in Vortex State Magnetic Disks, *Phys. Rev. Lett.* **99**, 247208 (2007).

[144] Krivorotov, I.N., Emley, N.C., Buhrman, R.A. & Ralph, D.C., Time-domain studies of very-large-angle magnetization dynamics excited by spin transfer torques, *Phys. Rev. B* **77**, 054440 (2008).

[145] Smith, W.W. & Smith, J.M., *Handbook of Real-Time Fast Fourier Transforms*, IEEE Press, Piscataway (1995).

[146] Houssameddine, D., Ebels, U., Dieny, B., Garello, K., Michel, J.P., Delaet, B., Viala, B., Cyrille, M.C., Katine, J.A. & Mauri, D., Temporal Coherence of MgO Based Magnetic Tunnel Junction Spin Torque Oscillators, *Phys. Rev. Lett.* **102**, 257202 (2009).

[147] Kuch, W., Magnetic Imaging, in *Magnetism: A Synchrotron Radiation Approach* (E. Beaurepaire, H. Bulou, F. Scheurer & J. Kappler, eds.), Springer, Berlin / Heidelberg, 275–320 (2006).

[148] Schütz, G., Wagner, W., Wilhelm, W., Kienle, P., Zeller, R., Frahm, R. & Materlik, G., Absorption of circularly polarized x rays in iron, *Phys. Rev. Lett.* **58**, 737–740 (1987).

[149] Stöhr, J., Wu, Y., Hermsmeier, B.D., Samant, M.G., Harp, G.R., Koranda, S., Dunham, D. & Tonner, B.P., Element-specific magnetic micoscopy with circularly polarized x-rays., *Science* **259**, 658 (1993).

[150] Stöhr, J., Exploring the microscopic origin of magnetic anisotropies with X-ray magnetic circular dichroism (XMCD) spectroscopy, *J. Magn. Magn. Mater.* **200**, 470 – 497 (1999).

[151] Acremann, Y., Chembrolu, V., Strachan, J.P., Tyliszczak, T. & Stöhr, J., Software defined photon counting system for time resolved x-ray experiments, *Rev. Sci. Instrum.* **78**, 014702 (2007).

[152] Stöhr, J., Magnetic Dichroism Spectroscopy and Microscopy, retrieved in May 2010 from http://ssrl.slac.stanford.edu/stohr/xmcd.htm.

[153] Söderlind, P., Eriksson, O., Johansson, B., Albers, R.C. & Boring, A.M., Spin and orbital magnetism in Fe-Co and Co-Ni alloys, *Phys. Rev. B* **45**, 12911–12916 (1992).

[154] Samant, M.G., Stöhr, J., Parkin, S.S.P., Held, G.A., Hermsmeier, B.D., Herman, F., Van Schilfgaarde, M., Duda, L.C., Mancini, D.C., Wassdahl, N. & Nakajima, R., Induced spin polarization in Cu spacer layers in Co/Cu multilayers, *Phys. Rev. Lett.* **72**, 1112–1115 (1994).

[155] Kilcoyne, A.L.D., Tyliszczak, T., Steele, W.F., Fakra, S., Hitchcock, P., Franck, K., Anderson, E., Harteneck, B., Rightor, E.G., Mitchell, G.E.,

Hitchcock, A.P., Yang, L., Warwick, T. & Ade, H., Interferometer-controlled scanning transmission X-ray microscopes at the Advanced Light Source, *J. Sync. Radiat.* **10**, 125–136 (2003).

[156] Guslienko, K.Y., Han, X.F., Keavney, D.J., Divan, R. & Bader, S.D., Magnetic Vortex Core Dynamics in Cylindrical Ferromagnetic Dots, *Phys. Rev. Lett.* **96**, 067205 (2006).

[157] Strachan, J.P., Chembrolu, V., Acremann, Y., Yu, X.W., Tulapurkar, A.A., Tyliszczak, T., Katine, J.A., Carey, M.J., Scheinfein, M.R., Siegmann, H.C. & Stöhr, J., Direct Observation of Spin-Torque Driven Magnetization Reversal through Nonuniform Modes, *Phys. Rev. Lett.* **100**, 247201 (2008).

[158] Bolte, M., Meier, G., Krüger, B., Drews, A., Eiselt, R., Bocklage, L., Bohlens, S., Tyliszczak, T., Vansteenkiste, A., Van Waeyenberge, B., Chou, K.W., Puzic, A. & Stoll, H., Time-Resolved X-Ray Microscopy of Spin-Torque-Induced Magnetic Vortex Gyration, *Phys. Rev. Lett.* **100**, 176601 (2008).

[159] Kasai, S., Fischer, P., Im, M.Y., Yamada, K., Nakatani, Y., Kobayashi, K., Kohno, H. & Ono, T., Probing the Spin Polarization of Current by Soft X-Ray Imaging of Current-Induced Magnetic Vortex Dynamics, *Phys. Rev. Lett.* **101**, 237203 (2008).

[160] Curcic, M., Van Waeyenberge, B., Vansteenkiste, A., Weigand, M., Sackmann, V., Stoll, H., Fähnle, M., Tyliszczak, T., Woltersdorf, G., Back, C.H. & Schütz, G., Polarization Selective Magnetic Vortex Dynamics and Core Reversal in Rotating Magnetic Fields, *Phys. Rev. Lett.* **101**, 197204 (2008).

[161] Rippard, W.H., Pufall, M.R., Kaka, S., Silva, T.J., Russek, S.E. & Katine, J.A., Injection Locking and Phase Control of Spin Transfer Nano-oscillators, *Phys. Rev. Lett.* **95**, 067203 (2005).

[162] Scheinfein, M.R., LLG Micromagnetic Simulator^{TM}, http://llgmicro.home.mindspring.com.

[163] Hertel, R. & Kronmüller, H., Computation of the magnetic domain structure in bulk permalloy, *Phys. Rev. B* **60**, 7366–7378 (1999).

[164] Ha, J.K., Hertel, R. & Kirschner, J., Micromagnetic study of magnetic configurations in submicron permalloy disks, *Phys. Rev. B* **67**, 224432 (2003).

[165] Hertel, R., Fruchart, O., Cherifi, S., Jubert, P.O., Heun, S., Locatelli, A. &

Kirschner, J., Three-dimensional magnetic-flux-closure patterns in meso-scopic Fe islands, *Phys. Rev. B* **72**, 214409 (2005).

[166] Rantschler, J.O., Chen, P.J., Arrott, A.S., McMichael, R.D., W. F. Egelhoff, J. & Maranville, B.B., Surface anisotropy of permalloy in NM/NiFe/NM multilayers, *J. Appl. Phys.* **97**, 10J113 (2005).

[167] Strachan, J.P., Chembrolu, V., Yu, X.W., Tyliszczak, T. & Acremann, Y., Synchronized and configurable source of electrical pulses for x-ray pump-probe experiments, *Rev. Sci. Instrum.* **78**, 054703 (2007).

[168] Cullity, B.D. & Graham, C.D., *Introduction to magnetic materials*, Wiley-IEEE, Hoboken (2009).

[169] Voltairas, P.A., Fotiadis, D.I. & Massalas, C.V., Estimation of exchange constant A and g factor for CoxNi1-x microspheres from size-dependent ferromagnetic resonance modes, *J. Magn. Magn. Mater.* **217**, L1–L4 (2000).

[170] Bozorth, R., *Ferromagnetism*, Van Nostrand, New York, Toronto, London (1951).

[171] Wijn, H., *Magnetic properties of metals : d-elements, alloys, and compounds*, Springer-Verlag, Berlin, New York (1991).

[172] Fuchs, G.D., Sankey, J.C., Pribiag, V.S., Qian, L., Braganca, P.M., Garcia, A.G.F., Ryan, E.M., Li, Z.P., Ozatay, O., Ralph, D.C. & Buhrman, R.A., Spin-torque ferromagnetic resonance measurements of damping in nano-magnets, *Appl. Phys. Lett.* **91**, 062507 (2007).

[173] Bass, J. & Pratt, W.P., Spin-diffusion lengths in metals and alloys, and spin-flipping at metal/metal interfaces: an experimentalist's critical review, *JOP: Cond. Mat.* **19**, 183201 (2007).

[174] Seidel, H., Csepregi, L., Heuberger, A. & Baumgärtel, H., Anisotropic Etching of Crystalline Silicon in Alkaline Solutions, *J. Electrochem. Soc.* **137**, 3612–3626 (1990).